

Dimensionality transitions in group III–V  
semiconductors



Guang Zhu

Department of Electrical and Electronics Engineering

University College London

Dissertation submitted for the Degree of Doctor of Philosophy

Supervisor: Prof. Sir Michael Pepper

Aug, 2016

I declare all the results done in this thesis is my own work, except where has clearly indicated in the text.

A handwritten signature in black ink, consisting of stylized Chinese characters, likely '朱光' (Zhu Guang).

Guang Zhu

Aug 2016

## **Acknowledgements**

I would like to thank my supervisor Prof. Sir Michael Pepper for giving me this great opportunity to work and study in the field of quantum transport in University College London. He has given me great supports not only in academic aspects, but also in personal life. I am inspired by him during the whole time.

I am greatly thankful to Dr. Sanjeev Kumar from our group, who gave me advises in data acquisition of low dimensional transport research. He taught me how to set up measurements step by step, with great of enthusiasm and patients. He also shared experiences to every members in the group and troubleshoot with us when anyone struggled in their experiments.

No measurements could be done without the devices. I, therefore, greatly indebted to Dr.Ian Farrer for growing plenty of world class wafer, and Dr.Graham Creeth, who made the excellent devices for me to give me chance to explore the fascinating quantum world. Dr.Graham Creeth also gave me a demonstration in fabricating nano-scale devices, with the assist of Dr.David English, which enlightened me in fabricating devices.

I would also like to express my gratitude to Mr.Henry Montague and Mr.Chengyu Yan, who are PhD students in our group. Henry gave me great help especially in cleanroom work. He is always sharing everything to us, as well as burst with new ideas about fabricating device. Chengyu discussed my experiments with me to a great extent, and generously shared his knowledge and opinions.

Here, I would also like to thank Prof. Tony Kenyon and Dr. Stuart Holmes sincerely for their careful evaluating towards my thesis. They has been given me a huge amount of essential suggestions which helped me make improvements on the final thesis.

Last but not least, I would like to thank my family. They are supportive both materially and mentally throughout the years. Especially the meticulous care of everything from my wife.

## **Abstract**

Since their conception two centuries ago, semiconductors have rapidly become one of the most active fields of research. As their exceptional potential became recognised, increasing amounts of resources were invested in the research and production of these materials. Consequently, semiconductor industry has gradually grown to become an essential lifeline of world economics. In the early 1980, the demand for electronic device miniaturisation, high integration and high computing speed led to the emergence of mesoscopic physics. Meanwhile, advances in materials science and microprocessing technology enabled experimental study in this area. By constantly reducing the scale of semiconductor devices, manufacturers could integrate smaller electronic devices onto one chip. These so-called integrated circuits perform storage, computing and other functions. In current production lines of the semiconductor industry, nanoscale electronic components have become the conventional technology.

This thesis investigates transport properties of two-dimensional electrons using the phenomenon of magnetoresistance in perpendicular magnetic fields at low temperature. Dimensionality transitions are enabled by quantum point contact.

Chapter 1 and 2 introduce the background information and low dimensional transport related theories, respectively. Chapter 3 describes the sample fabrication technique, instruments used in our experiments and the experimental set-up.

Low-temperature measurements of the split-gate  $GaAs/AlGaAs$  heterostructure are fully described in Chapter 4. The phase-coherence information is extracted by investigating the weak localisation effect at various temperature. The temperature dependence of phase coherence experimentally reflects the underlying transport properties.

Chapter 5 investigates and discusses the universal conductance fluctuation. The  $InGaAs/InAlAs$  heterostructure using which we interpret the low-temperature transport phenomena, is experimentally investigated in Chapter 6.

# Contents

<b>1</b>	<b>Introduction</b>	<b>4</b>
1.1	Semiconductor heterostructures . . . . .	4
1.2	Basic properties . . . . .	6
1.3	Magnetic field effect . . . . .	9
<b>2</b>	<b>The Physics of Disordered Low-dimensional Systems</b>	<b>17</b>
2.1	Anderson localisation . . . . .	17
2.2	Scaling theory . . . . .	20
2.3	Weak localisation . . . . .	23
2.4	Magnetoresistance of quantum interference . . . . .	28
2.5	Bergmann's approach . . . . .	31
2.6	Spin-orbit interaction . . . . .	34
2.7	Electron interactions . . . . .	35
2.7.1	Interactions in diffusion channels . . . . .	36
2.7.2	Interactions in Cooper channels . . . . .	37
2.8	Magnetoresistance of interaction effects . . . . .	38
2.9	Inelastic scattering . . . . .	40
2.9.1	Electron-electron scattering . . . . .	40
2.9.2	Electron-phonon scattering . . . . .	42

2.10	Phase coherence . . . . .	45
2.11	Narrow Devices . . . . .	48
2.12	Heterostructures . . . . .	50
<b>3</b>	<b>Experimental Techniques</b>	<b>53</b>
3.1	Fabrication techniques . . . . .	53
3.1.1	Wafer growth . . . . .	54
3.1.2	Wafer patterning . . . . .	55
3.2	Low-temperature techniques . . . . .	58
3.2.1	$^4\text{He}$ cryostat . . . . .	58
3.2.2	$^3\text{He}$ cryostat . . . . .	59
3.2.3	$^4\text{He}/^3\text{He}$ dilution cryostat . . . . .	59
3.3	Measurement techniques . . . . .	60
3.3.1	Two-terminal measurement . . . . .	61
3.3.2	Four terminal measurement . . . . .	62
<b>4</b>	<b>Magneto-transport in GaAs/AlGaAs Heterojunctions</b>	<b>63</b>
4.1	Quantum transport and dimensionality t-ransitions in GaAs/AlGaAs heterostructures . . . . .	67
4.1.1	Devices used in this work and experimental setup . . . . .	67
4.1.2	Two-dimensional quantum transport . . . . .	69
4.1.3	Width estimates . . . . .	73
4.1.4	One-dimensional quantum transport . . . . .	75
4.2	One-dimensional quantum interference . . . . .	86
4.3	Weak anti-localisation . . . . .	89
4.4	Interaction effect in low-dimensional GaAs heterojunctions. . . . .	93

4.4.1	Interactions in two dimensions . . . . .	93
4.4.2	Interactions in one dimension . . . . .	94
4.4.3	2D-to-1D transitions . . . . .	96
<b>5</b>	<b>Universal Conductance Fluctuations</b>	<b>98</b>
5.1	Universal behaviour at $T=0$ . . . . .	99
5.2	Fluctuations at finite temperatures . . . . .	103
5.3	Fluctuations in GaAs/AlGaAs heterojunctions . . . . .	106
5.3.1	Fluctuations in 2D . . . . .	106
5.3.2	Fluctuations in 1D . . . . .	108
<b>6</b>	<b>Magneto-transport in InGaAs/InAlAs Heterojunctions</b>	<b>111</b>
6.1	Transport in top-gate devices . . . . .	112
6.2	Transport in split-gate devices . . . . .	118
<b>7</b>	<b>Conclusions and suggestions</b>	<b>123</b>
<b>A</b>	<b>The growth structure of the experimental wafers</b>	<b>142</b>
<b>B</b>	<b>List of Notations</b>	<b>145</b>

# Chapter 1

## Introduction

### 1.1 Semiconductor heterostructures

Two-dimensional systems have always been pivotal for investigating quantum effects at low temperature. At present, a two-dimensional system can be achieved by three main methods [1]:

*a.*Single electron shell on the surface of liquid helium. Liquid helium surface attracts the electrons by image potential, and prevent electrons entering liquid helium with a 1-eV barrier.

*b.*Electron gas travels two-dimensionally along the  $Si - SiO_2$  interface in the inversion layer of an insulated gate field-effect transistors (FET);

*c.*Electron gas travels two-dimensionally through the conduction band valleys of superlattices (heterojunctions).

In recent decades, thin-film FETs have been replaced with heterojunction nanostructures, which have become the new standard for investigating the physical properties of semiconductor materials since the large development of devices fabrication. The two-dimensional electron gas (2DEG) formed in

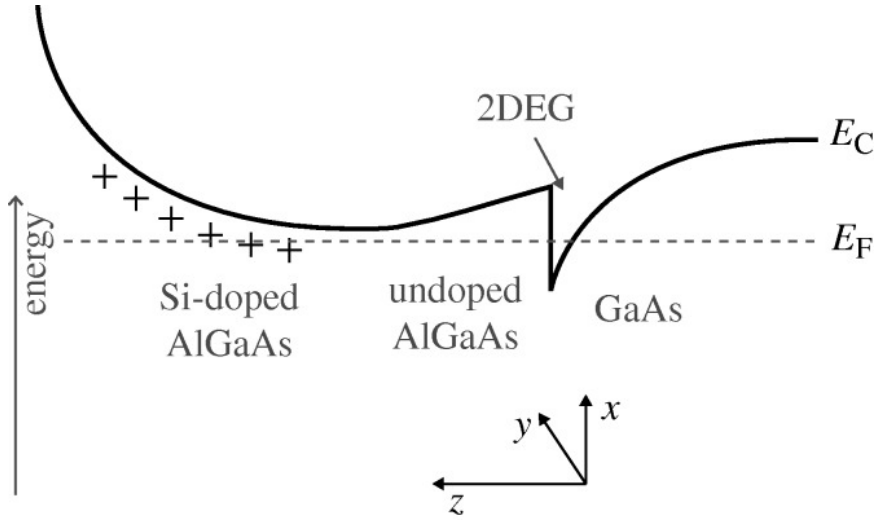


Figure 1.1: Band bending diagram of a modulation doped  $GaAs/Al_xGa_{(1-x)}As$  heterostructure [2].

heterojunctions formed in heterojunctions increases the mobility and mean free path in the semiconductor devices, and lengthens the Fermi wavelength.

Among the many species of two-dimensional electron gas systems,  $GaAs/Al_xGa_{(1-x)}As$  heterojunction is most commonly used.  $Al_xGa_{(1-x)}As$  has a wider band gap than  $GaAs$ ; for example when  $x = 0.3$ , the conduction band is  $0.3 - eV$  lower in  $GaAs$  than in  $Al_xGa_{(1-x)}As$ . The top surface of  $Al_xGa_{(1-x)}As$  is covered by an epitaxial layer of a  $Si$ -doped  $Al_xGa_{(1-x)}As$ . The conduction band will bend at the interface of two materials, forming a triangular potential well at the  $GaAs/Al_xGa_{(1-x)}As$  junction. The bottom of this triangular potential well is below the Fermi level. At very low temperatures, as the electrons flow from the  $Si$ -doped  $Al_xGa_{(1-x)}As$  to  $GaAs$ , many of them become bound inside the triangle potential well, forming a two-dimensional electron gas. In  $GaAs/Al_xGa_{(1-x)}As$  modulation-doped heterojunction interface, this two-dimensional gas forms a near-ideal two-

dimensional electron system, with the highest electron mobility achieved to date ( $\sim 10^7 \text{cm}^2 \text{V}^{-1} \text{s}^{-1}$ ). As the *GaAs* and *Al<sub>x</sub>Ga<sub>(1-x)</sub>As* lattice constants are similar, modern molecular beam epitaxy (MBE) techniques can obtain an almost atomically flat interface, greatly reducing the defects and roughness at the interface and hence enhancing the transport properties. Moreover, a buffer layer of intrinsic *Al<sub>x</sub>Ga<sub>(1-x)</sub>As* is placed between the *GaAs* substrate and the *Si*-doped *Al<sub>x</sub>Ga<sub>(1-x)</sub>As*, which greatly reduces the donor impurity scattering of the electrons, thus greatly enhancing the electron mobility in the two-dimensional electron gas [3].

## 1.2 Basic properties

The Drude model proposes that the current density  $j$  is proportional to the electric field  $E$ . The proportionality constant is the conductivity  $\sigma$  [4] [5]:

$$j = \sigma E; \sigma = \frac{n_e e^2 \tau}{m^*} = n_e e \mu \quad (1.1)$$

where  $\mu$  is the electron mobility,  $n_e$  is the carrier density and  $\tau$  is the scattering time, defined as the average time between scatterings.

The Drude model describes the diffusive movement of electrons when the characteristic length  $L$  is much larger than the mean free path (average distance between scatterings)  $l$  of electrons. This is usually the case in bulk systems (all 3D systems and some 2D systems). If  $L$  is much smaller than  $l$ , the electron transport becomes ballistic. In the ballistic transport regime, the electrons move without any scattering, so momentum and phase relaxations

are absent. In this case, we must apply Fermi-Dirac statistic.

The conductivity and density of states at the Fermi level are related through the Einstein relation

$$\sigma = De^2\rho(E_F) \quad (1.2)$$

where  $D$  denotes the diffusion constant and  $\rho(E_F)$  is the density of states at Fermi level. In two dimensions,  $D$  can be deduced by combining of Drude model with Einstein relation:

$$D = \frac{1}{2}v_F^2\tau = \frac{1}{2}v_Fl \quad (1.3)$$

In the event of quantum interferences, the diffusion correlations will disappear at the order of the phase coherence time  $\tau_\phi$ , rather than the scattering time  $\tau$  (as occurs in the classical case). At very low temperatures, the diffusion correlations are associated with inelastic scattering, and the coherence time  $\tau_\phi$  far exceeds the scattering time  $\tau$ .

The conductivity and conductance are related through Ohm's law,

$$G = \frac{W}{L}\sigma \quad (1.4)$$

where  $W$  and  $L$  are the width and length of the 2DEG, respectively. When both  $W$  and  $L$  are much longer than the mean free path  $l$ , the electron

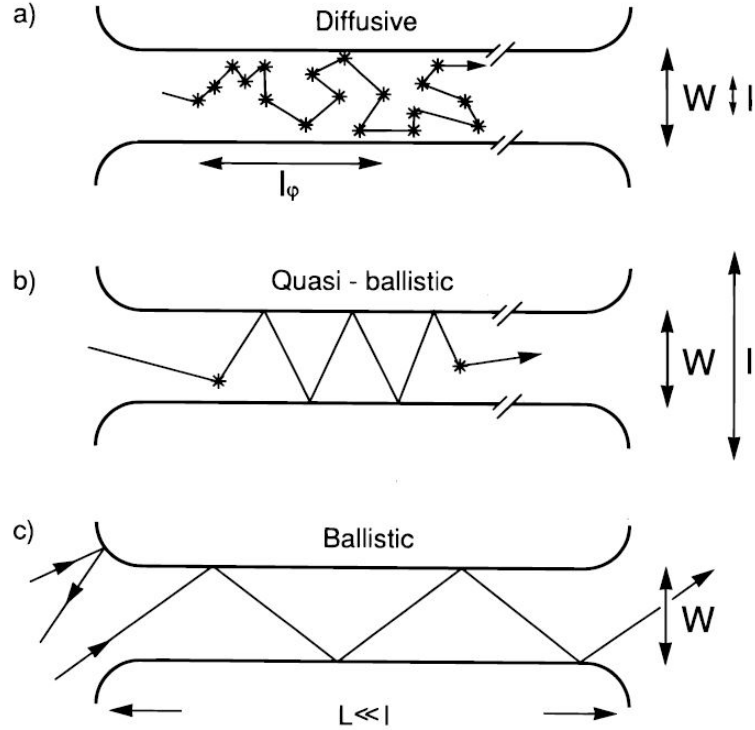


Figure 1.2: Electron trajectories in various regimes: *a*)diffusion regimes ( $l < W, L$ ); *b*)quasi-ballistic regimes ( $W < l < L$ ); *c*)ballistic regimes ( $W, L < l$ ) [6].

transport is diffusive. When the dimensions of 2DEG are shorter than  $l$ , the system enters ballistic regime, in which the conductance is unrelated to conductivity, but is instead described by the Landauer formula,

$$G = \frac{(2e^2)}{h} \sum_{i=1}^n T_i \quad (1.5)$$

where  $n$  is the number of occupied subbands, and  $T$  is the transmission probability. The electron trajectories in each regime are illustrated in Figure

1.2.

Accounting for quantum interference, the characteristic length is not the elastic mean free path  $l$ ; rather, it is phase coherence

$$L_\phi = \sqrt{D\tau_\phi} \quad (1.6)$$

At very low temperatures, the phase coherence length becomes very large, it is possible that only need to concern conductance but still in diffusion transport regime. This idea is further discussed in the next chapter.

### 1.3 Magnetic field effect

An external magnetic field induces fundamentally intriguing behaviour in semiconductor heterojunction systems. These behaviours have roused great interest in mesoscopic physics. When a magnetic field is applied perpendicularly to the current direction in a 3D bulk conductor, a voltage difference appears in the direction vertical to the current. The linear relationship between this differential voltage and the magnetic field describes the famous Hall Effect. A similar effect appears in 2DEG systems, where the electrons are confined to a 2D plane. A magnetic field applied perpendicularly to the 2DEG plane induces a Hall voltage such as that in 3D systems. However, whereas this longitudinal voltage (or longitudinal resistance) varies linearly under low magnetic field, it exhibits quantised plateaus under high magnetic field. This abnormal variation of longitudinal resistance, named by quantum Hall Effect (QHE) or quantised Hall Effect, was first observed by van Klitz-

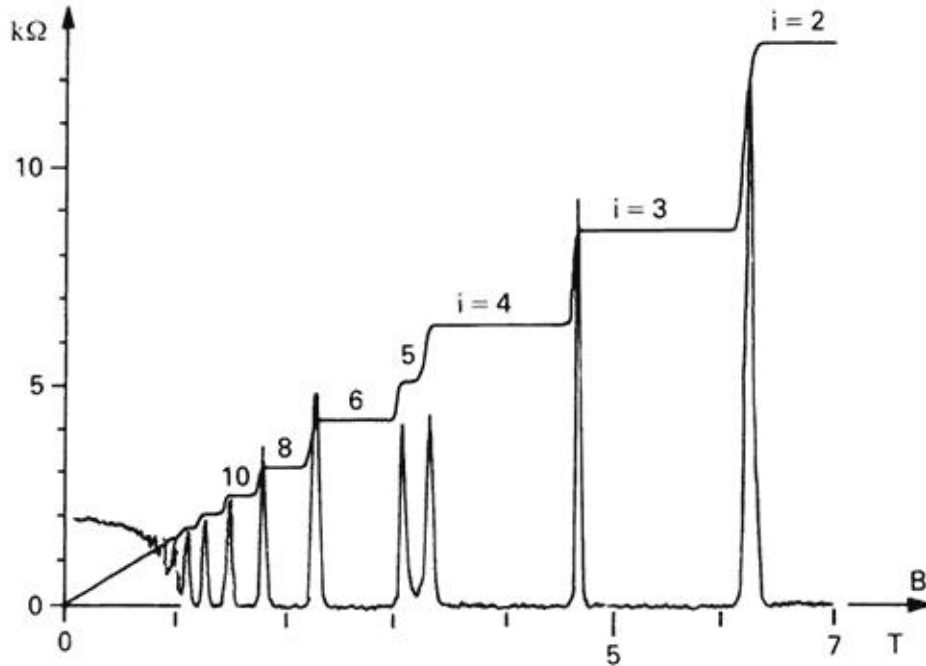


Figure 1.3: Quantum Hall Effect (plateaus) and Shubnikov-de Haas oscillations [7].

ing and Pepper [7]. For this work, published in 1980, van Klitzing received the Nobel Prize in Physics in 1985.

The QHE has become a widely accepted technique for measuring fine semiconductor structures in solid state physics. In a small perpendicular field,  $\rho_{xx}$  (Resistivity in transverse) remains constant while  $\rho_{xy}$  (Resistivity in longitudinal) linearly increases from zero as predicted by the Boltzmann equation. As the field increases, the  $\rho_{xx}$  begins to oscillate with a period of  $1/B$  (where  $B$  is the magnitude of magnetic field) and the  $\rho_{xy}$  plateaus at fractions of  $h/e^2$ . These oscillations are called Shubnikov-de Haas oscillations and the quantised plateaus demonstrate the quantum Hall effect.

As the field is perpendicular to the 2DEG, the electrons move in a circular path at a frequency of

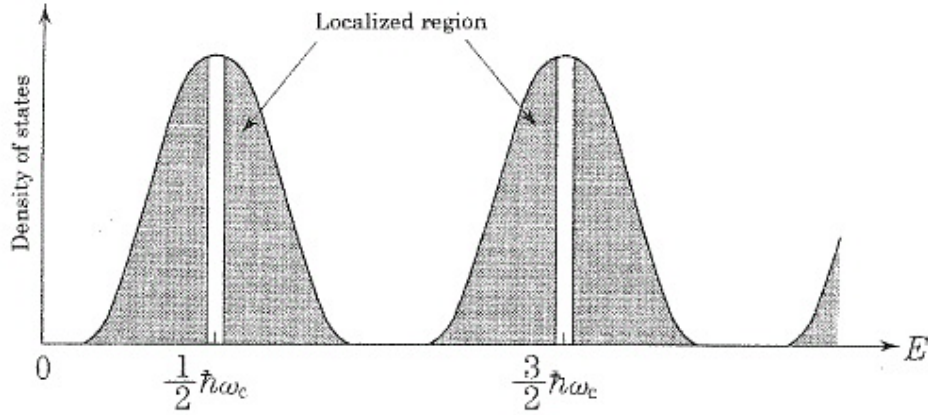


Figure 1.4: Broadening state model due to potential energy variations in 2DEG. The localised states is marked as white part, and the shaded part refers to the extended states. Because the imperfections exist in the sample, the Landau levels are randomly distributed with a small difference in energy across the sample. The amplitude of this energy difference forms the tails of Landau levels(localised states). Only the electrons in the extended states participate conduction. [8].

$$\omega_c = \frac{eB}{m^*} \quad (1.7)$$

where  $e$  is the elementary charge, and  $m^*$  is the effective mass of the electron. This is called the cyclotron frequency. The cyclotron radius corresponds to a classical orbit with energy given by

$$E_n = \hbar\omega_c \left( n + \frac{1}{2} \right), n = 0, 1, 2, 3 \dots \quad (1.8)$$

These energy levels are the Landau levels in two-dimensional systems. Considering the additional effect of spin splitting, this equation becomes

$$E_n = \hbar\omega_c \left( n + \frac{1}{2} \right) \pm \frac{g\mu_B B}{2}, n = 0, 1, 2, 3 \dots \quad (1.9)$$

where  $g$  is the g-factor and  $\mu_B$  is the Bohr magneton. The filling factor, which specifies the number of occupied Landau levels [8]. It can be defined by the carrier density in a two dimensional system  $n_{2D}$  under any perpendicular magnetic field  $B$ :

$$v = n_{2D} \frac{h}{eB} \quad (1.10)$$

where  $v$  is the filling factor.

The effective potential in a 2D system is influenced by impurities, crystal lattice defects and interfaces. These effects feed into the Landau levels, broadening the energy levels (see Figure 1.4). Energy level states may be localised (at the tails of the Landau levels) or extended (at the centres of Landau levels). As the magnetic field decreases, the resistance plateaus are gradually filled by localised states. Once the extended states have been filled, the next Hall resistance plateau begins filling. As the magnetic field increases, the spacing between two Landau levels becomes larger. In other words, at higher field, 'more time' is required to fill each Landau level than at lower field with a linear varying magnetic field. The Schrödinger equation of a systems under an applied magnetic field is given by

$$\frac{1}{2m^*} \left( p_x - \frac{eB}{2} y \right)^2 \Psi + \frac{1}{2m^*} \left( p_y - \frac{eB}{2} x \right)^2 \Psi = E\Psi \quad (1.11)$$

Expanding the brackets we find that

$$\frac{p^2}{2m^*} + \frac{eB}{2m^*} Z\Psi + \frac{1}{2m^*} \left( \frac{eB}{2} \right)^2 (x^2 + y^2)\Psi = E\Psi \quad (1.12)$$

where  $Z$  is the z-component of the angular momentum. The first magnetic field dependent term is linear, but the second term is a parabolic potential. The confinement of this potential increases as the magnetic field increases. Under strong magnetic field, the eigenstates are localised to an area of  $h/eB$  around an arbitrarily chosen origin.

As the magnetic field is increased, the density of each Landau level increases. At some critical field, the highest occupied Landau level becomes depopulated, and the Fermi level discontinuously drops to the next lower level. Thus, the number of occupied Landau levels decreases as the magnetic field increases. This discontinuity in the Fermi energy with either density or magnetic field results in an oscillatory behaviour. [9–16].

The expression  $N(E)dE$  gives the number of states in the energy range  $[E, E + dE]$ . Assuming that the Fermi level is sufficiently far from the conduction band, we can assume that all of the available energy levels in the conduction band are obtained at the band edge. In n-type semiconductors, the carrier density is given by

$$n_e = N_c f(E_C) = \frac{N_C}{1 + \exp\left(\frac{E_C - E_F}{k_B T}\right)} \quad (1.13)$$

where  $N_C$  is the density of states function,  $E_C$  is the energy level above the conduction band and  $E_F$  is the Fermi energy. In the intrinsic semiconductors, the activation energy is defined as  $|E_C - E_F|/2$ . If  $|E_C - E_F| > 4k_B T$ , where  $k_B$  is the Boltzmann constant, the Fermi-Dirac distribution can be approximated by the Boltzmann distribution:

$$f(E_C) = \frac{1}{1 + \exp\left(\frac{E_C - E_F}{k_B T}\right)} \approx \exp\left(\frac{E_F - E_C}{k_B T}\right) \quad (1.14)$$

and the carrier density becomes

$$n_e = N_c \exp\left(\frac{E_F - E_C}{k_B T}\right) \quad (1.15)$$

If the mobility  $\mu$  is known, the conductivity is calculated as  $\sigma = n_e e \mu$ , and we have

$$\sigma = e \mu N_c \exp\left(\frac{E_F - E_C}{k_B T}\right) \quad (1.16)$$

Taking the natural logarithm of both sides, we get

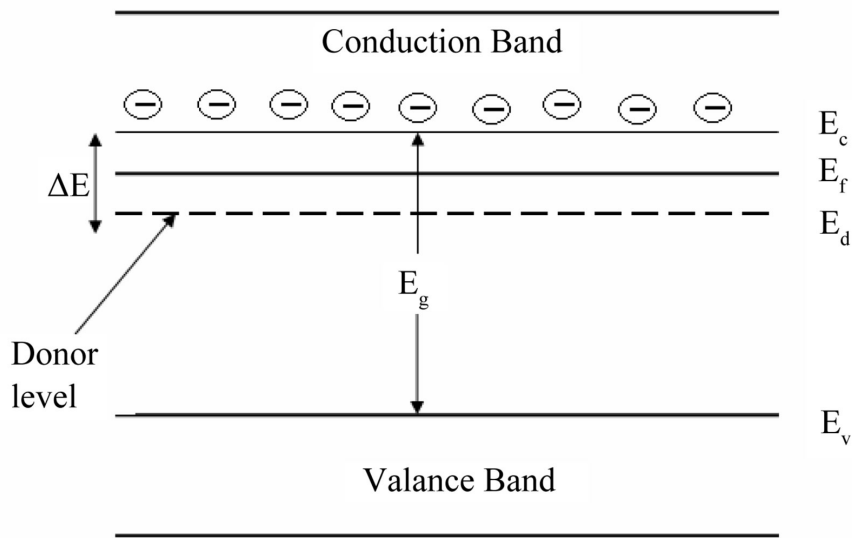


Figure 1.5: Band diagram for activation energy in n-type semiconductor. The activation energy is defined as  $E_c - E_d$ , where  $E_d$  is the donor level [17].

$$\ln(\sigma) = \ln(e\mu N_c) + \left( \frac{E_F - E_C}{k_B T} \right) \quad (1.17)$$

where  $|E_F - E_C| > 4k_B T$ . This equation states that the natural logarithm of conductivity is a linear function of  $1/T$ . Figure 1.5 illuminates band diagram of the activation energy in n-type semiconductors.

If the carrier density and environmental temperature are sufficiently low, the two-dimensional electron gases in fine devices will further condense into liquid states. In these states, the quantised plateaus do appear at non-integer filling factor. In order to distinguish the quantum Hall effect with integer filling factor from plateaus with non-integer filling factors, we named them integer quantum Hall effect and fractional quantum Hall effect, respectively. This distinction will not be further discussed here.

The amplitude envelope of the Shubnikov-de Haas oscillations is given by [18]

$$\frac{\Delta G}{G} = \frac{2(\omega_c \tau)^2}{1 + (\omega_c \tau)^2} \frac{\frac{2\pi^2 k_B T}{\hbar \omega_c}}{\sinh \frac{2\pi^2 k_B T}{\hbar \omega_c}} \exp\left(\frac{-\pi}{\omega_c \tau}\right) \quad (1.18)$$

The condition of this equation is that the  $k_B T > \hbar \omega_c$ . The effective mass can be derived from the temperature dependence of the oscillation amplitude.

# Chapter 2

## The Physics of Disordered Low-dimensional Systems

### 2.1 Anderson localisation

At low temperatures, the small heat energy  $\frac{1}{2}k_B T$  cannot free the electrons from the Coulomb force of their binding atoms, so very few of the carriers conduct. The number of bound states of an electron in a finite quantum well decreases with decreasing width of the quantum well. At some critical width, the number of bound states is zero. Moreover, all conducting materials have a small lattice constant, which increase as the carrier concentration decreases. Eventually, most of the electrons become bound and the conductivity considerable decreases. The metal-insulator transition (MIT), at which conduction ceases, was proposed by Mott in 1949 [19]. This transition occurs at some critical electron density, which may be changed by temperature, pressure, external fields and doping levels in semiconductors.

However, Mott's treatment ignores the disorder in the system. A more

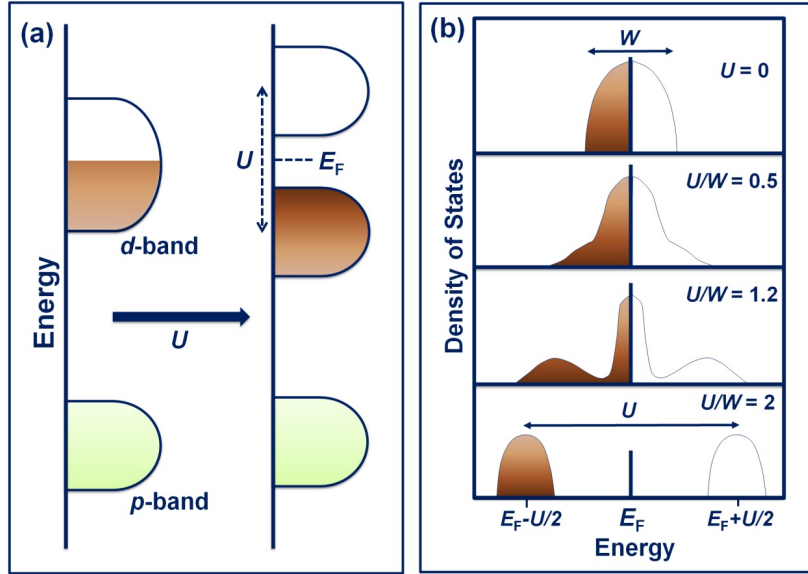


Figure 2.1: Schematic representation of the energy levels for a Mott–Hubbard insulator where on-site Coulomb interaction  $U$  splits the  $d$ -band into lower Hubbard band and upper Hubbard band. (b) Evolution of the density of states (DOS) of electrons as a function of  $U/W$  ( $W =$  bandwidth) as the system evolves from a metal to an insulator [20].

realistic treatment was first proposed by Anderson in 1958 [21].

He proposed that very strong disorders alter the wavefunction states of an electronic system from extended to localised. The envelope of the wavefunction will then exponentially decay from some point in space  $r_0$ :

$$|\Psi(r)| = \exp\left(\frac{-|r - r_0|}{\xi}\right) \quad (2.1)$$

where  $\xi$  is the localisation length. Anderson’s model can be expressed by a dimensionless parameter  $A/B$ , where  $A$  is the energy difference between two randomly located sites, and  $B$  is the energy bandwidth of the crystal or the overlap between two sites. Anderson found that if this parameter exceeds

some critical value, all states are localised. In a numerical study, Edwards and Thouless [22] determined  $A/B = 1/2$ .

Mott [23] pointed out that although the degree of disorder cannot localise all states in the band, and the tail states can also be assigned as localised states. The localised and extended states are separated by  $E_c$ . At  $T = 0$ , the conductivity is zero when  $E_F < E_c$ , and nonzero when  $E_F > E_c$ , indicating that the MIT can be altered by moving the Fermi level. Anderson localisation has been observed in low concentration Si-inversion layers [24, 25] and in *GaAs* metal-semiconductor FETs (MESFETs) [26].

In 1968, Mott proposed the minimum metallic conductivity concept [27], which predicts a discontinuous transition at  $E_c$  from zero conductivity. He noticed that in a metallic system, the mean free path always exceeds the de Broglie wavelength, implying that the usual transport theory fails in very low mobility systems. In a weakly disordered system, the Boltzmann conductivity can be estimated from Drude theory as:

$$\sigma_B = \frac{ne^2\tau}{m^*} \quad (2.2)$$

where  $\tau$  is the elastic scattering time, given by

$$\tau = \frac{v_F}{l} \quad (2.3)$$

$v_F$  is the Fermi velocity, and  $l$  is mean free path, respectively. This model is valid only when  $l$  is much greater than the wavelength, i.e.  $k_F l \gg 1$ .

When  $k_F l = 1$ , the metallic conductivity ceases. At this critical value the conductivity becomes,

$$\sigma_{min} = C_{3d} \frac{e^2}{\hbar l_{min}} \quad (2.4)$$

$l_{min}$  is the shortest possible mean free path, and  $C_{3d}$  is a constant in a 3D system. Mott proposed the following form of the minimal conductivity in two dimensions:

$$\sigma_{min} = C_{2d} \frac{e^2}{\hbar} \quad (2.5)$$

Note that this the conductivity is independent of the length parameter.

However, this proposition predicts a continuous transition from zero conductivity, which has been excluded by scaling theory.

## 2.2 Scaling theory

Mott and Twose [28] showed that all states in a 1D potential are localised. Thouless [29] proposed that in a 1D wire, the Anderson parameter for localisation,  $A/B$ , simply equals the wire resistance  $R = h/2e^2$ . At zero temperature, the wire resistance in a 1D potential is an exponential (rather than linear) function of length. The localisation length  $\xi_{1D}$  is then given by

$$\xi_{1D} = \frac{2Sk_F^2 l}{3\pi^2} \quad (2.6)$$

where  $S$  is the cross section area. Thouless also suggested that in two dimensions, no metallic states exist and that conductivity is a decreasing function with size. Extending Thouless's work, Abrahams et al. [30] provided the first comprehensive understanding of the MIT. They generalised the dimensionless conductance  $G$ , which defines the disorder parameter, and related it to the length scale of the system.

The scaling theory of Abrahams et al. replaces the single atomic site in the Anderson model with a  $d$ -dimensional hypercube of volume of  $L^d$ . Abrahams et al. proposed that the conductance of a hypercube of size  $2L$  is completely determined by the conductance of a hypercube of size  $L$ . An electron diffuses through distance  $L$  during time  $\tau = D/L^2$ , in the Anderson model, the dimensionless parameter  $A/B$  is therefore given by

$$\frac{A}{B} = N(E_F)L^d \frac{\hbar D}{L^2} \quad (2.7)$$

$$= \sigma L^{(d-2)} \frac{2\hbar}{e^2} = G \quad (2.8)$$

If two or more edge doubling processes occur, then the scaling equation is given by

$$\beta(G) = \frac{d \ln(G(L))}{d \ln(L)} \quad (2.9)$$

In weakly disordered systems, which obey the Boltzmann equation, the conductance is given by:

$$G(L) = \sigma L^{(d-2)} \quad (2.10)$$

and

$$\lim_{G \rightarrow \infty} \beta(G) = d - 2 \quad (2.11)$$

In strongly disordered systems ( $\xi < L$ ), most of the states are localised, and transport occurs only by hopping from an occupied to an unoccupied state. Thus we have

$$G(L) = G_0 \exp\left(-\frac{L}{\xi}\right) \quad (2.12)$$

and

$$\lim_{G \rightarrow 0} \beta(G) = \ln\left(\frac{G}{G_0}\right) \quad (2.13)$$

where  $G_0$  is a dimensionless ratio of order unity.  $\beta(G)$  is continuous and monotonic in all three dimensions:

$$d=1$$

$\beta(G)$  is negative at all conductances. As  $L \rightarrow \infty$ , the conductance exponentially decreases to zero.

d=2

Scaling theory predicts that  $\beta(G)$  is negative, indicating all states are localised, and no state is purely metallic at any length scale. As  $G \rightarrow \infty$ , the  $\beta(G)$  closely approximates zero. In this region, the conductance is less affected by the length scale, and metallic states may appear.

d=3

As  $G$  varies,  $\beta(G)$  can be either positive or negative, indicating that an MIT appears at suitable  $G$ . The critical conductance  $G_c$  located at  $\beta(G) = 0$  is an unstable point that separates the extended states ( $G > G_c$ ) from localised states ( $G < G_c$ ).  $\beta(G_c)$  is invariant at different length scales.

The 2D form of the conductivity correction has been observed in numerous types of systems such thin Au-Pd films [31], *Si*-metal-oxide-semiconductors(MOSFETs) [32], Mg films [33] and GaAs MESFETs [34].

## 2.3 Weak localisation

In weakly disordered systems ( $k_F l \gg 1$ ), the Boltzmann transport correction can be extended by perturbation theory. Abrahams et al. [30] investigated the behaviour of  $\beta(G)$  at  $G \rightarrow \infty$  by this approach, and found a length-dependent correction to the conductivity. This conductivity correction (denoted by  $\alpha$ ) accounts for the breakdown of electronic wave interference by the loss of phase memories. Thus, the scaling relation becomes

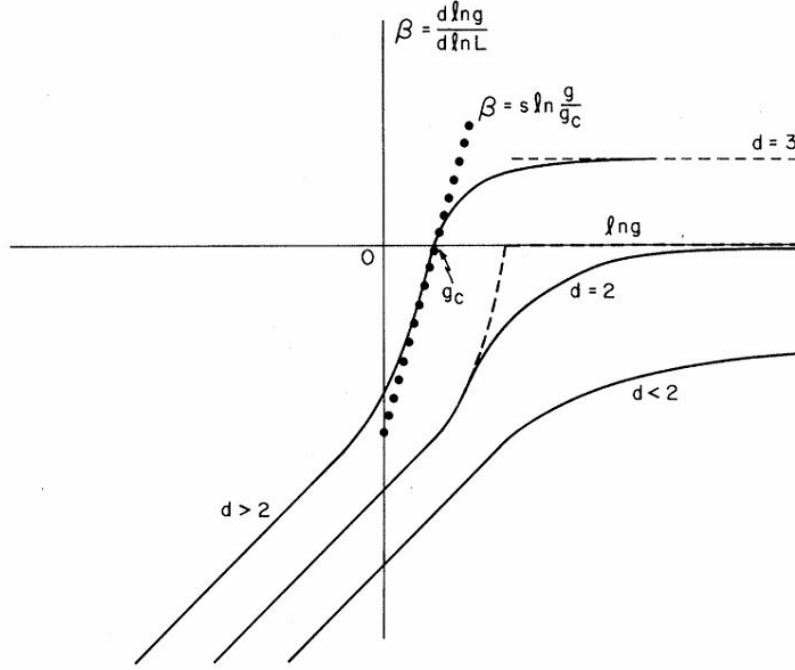


Figure 2.2: Plots of  $\beta(G)$  vs  $\ln(G)$  for  $d > 2$ ,  $d = 2$ ,  $d < 2$ .  $g(L)$  is the normalised "local conductance". Solid-circle line is the approximation  $\beta = s \ln(\frac{g}{g_c})$  to the  $g > 2$  case; this unphysical behaviour is necessary for the conductance jump in the  $d = 2$  case (dashed line) [30].

$$\beta(G) = (d - 2) - \alpha G^{(-1)} \quad (2.14)$$

In the 2D case, the conductance between length scales is given by

$$G(L) = G_B - \alpha \ln\left(\frac{L}{l}\right) \quad (2.15)$$

From perturbation theory, we obtain  $\alpha = 1/\pi^2$ . The 2D conductivity then becomes

$$\sigma(L) = \sigma_B - \frac{e^2}{\pi^2 \hbar} \ln \left( \frac{L}{l} \right) \quad (2.16)$$

where  $\sigma_B$  is the Boltzmann conductivity.

When the conductivity correction is comparable to the Boltzmann conductivity, the localisation length can be estimated from the length  $L$ :

$$\xi_{2d} = \text{lexp} \left( \sigma_B \frac{\pi^2 \hbar}{e^2} \right) \quad (2.17)$$

$$= \text{lexp} \left( \frac{\pi k_F l}{2} \right) \quad (2.18)$$

The conductivities in 3, 2 and 1 dimensions (corrected by perturbation theory) are respectively given by:

$$\sigma(L)_{3d} = \sigma_B - \frac{e^2}{2\pi^2 \hbar} \ln \left( \frac{1}{l} - \frac{1}{L} \right) \quad (2.19)$$

$$\sigma(L)_{2d} = \sigma_B - \frac{e^2}{\pi^2 \hbar} \ln \left( \frac{L}{l} \right) \quad (2.20)$$

$$\sigma(L)_{1d} = \sigma_B - \frac{e^2}{\pi \hbar} (L - l) \quad (2.21)$$

These corrections predicted by scaling and perturbation theories, are known as weak localisation. Because they result from interference between electronic waves, they are also known as quantum interference.

Consider a metallic material satisfying  $k_F l \gg 1$ . The electrons can travel from point  $A$  to point  $B$  by many different routes. As the distance between  $A$  and  $B$  is much longer than the mean free path  $l$ , the electron motion is diffusive. The probability  $T$  of the electrons travelling from  $A$  to  $B$  through all routes is given by

$$T_{AB} = \left| \sum_i A_i \right|^2 = \sum_i |A_i|^2 + \sum_{i \neq j} A_i A_j^* \quad (2.22)$$

This equation describes both classical and quantum behaviours. In most routes, the last term of Eq.(2.22) is zero. However, if the route self intersects, the electron is allocated to two amplitudes  $A_1$  and  $A_2$ , and travel around the loop in either directions (clockwise or anti-clockwise). Both phases of these coherent waves have equal amplitude ( $A_1 = A_2$ ); thus, the probability of travelling from  $A$  to  $C$  is

$$T_{AC} = |A_1|^2 + |A_2|^2 + 2\text{Re}(A_1 A_2^*) \quad (2.23)$$

$$= 4|A_1|^2 \quad (2.24)$$

This result reduces the probability of an electron travelling from  $A$  to  $B$ , which is equivalent to increasing the resistance. In other word, interference reduces the diffusion constant of the electrons. In any mechanism, that loses

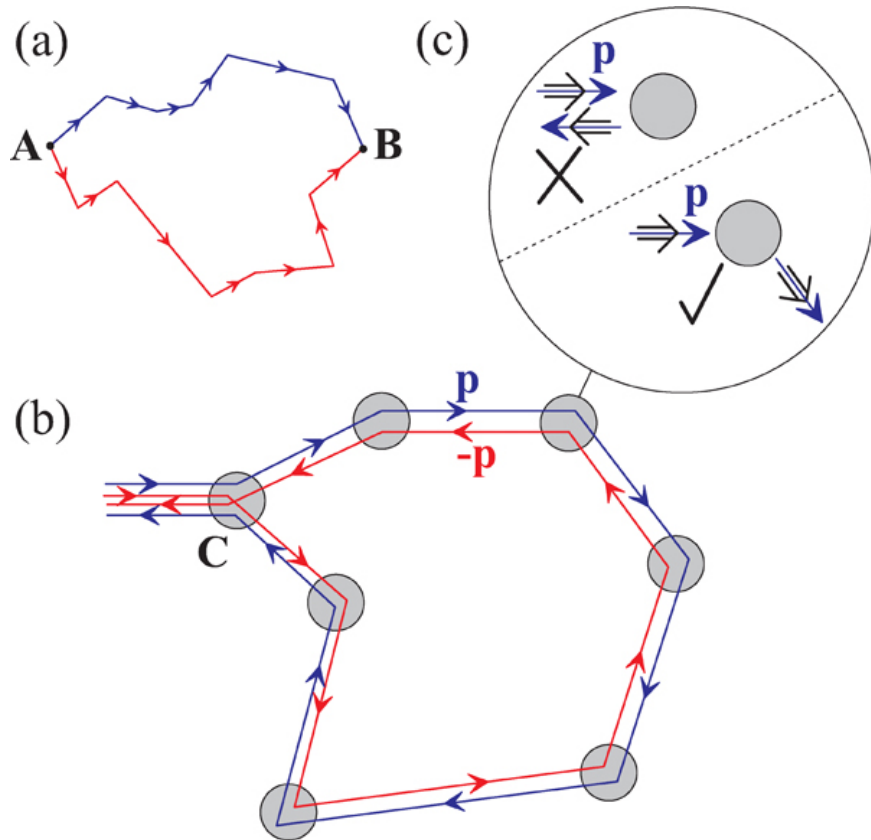


Figure 2.3: (a) Two classical paths connecting arbitrary points  $A$  and  $B$  in a two-dimensional disordered conductor. (b) A pair of closed paths contributing to the weak localisation correction. (c) In a single scattering event, a long-range potential cannot backscatter the chiral quasiparticles (upper left) because it cannot reverse the pseudospin direction (black arrows), but scattering in the forward or sideways direction (lower right) is allowed [35].

phase memory, this correction is voided. Thus, phase coherence is necessary for this correction effect.

Consider an electron that loses its phase memory after a certain lifetime  $\tau_\phi$ , if  $\tau_\phi \gg \tau$ , the electron will transport diffusively through a distance  $L_\phi$  before losing its phase coherence, where

$$L_\phi = \sqrt{D\tau_\phi} \quad (2.25)$$

If this length is shorter than the sample size,  $\tau_\phi$  is always the inelastic scattering time in a highly inelastic mechanism, such as electron-electron scattering. However, in an event such as electron-phonon scattering,  $\tau_\phi$  no longer equals the inelastic scattering time [36]. In a 2D system the system size exceeds than  $L_\phi$  in both directions, the quantum interference is two dimensional. If  $L_\phi > W$  (where  $W$  is the width of the conducting channel), the quantum interference exhibits 1D behaviour.

## 2.4 Magnetoresistance of quantum interference

When a sample is placed in a magnetic field, the phase difference between two coherent waves travelling in opposite directions around a loop is given by

$$\Delta\phi = 2eBS \quad (2.26)$$

where  $S$  is the area of the loop projected onto the plane perpendicular to the magnetic field  $B$ . The reduced phase coherence of the two waves reduces the probability of the electron returning to its origin, and hence increases the global conductivity.

Altshuler et al. [37] and Hikami et al. [38] calculated the 2D quantum interference correction in a magnetic field as

$$\delta\sigma(B, T) = \frac{e^2}{2\pi^2\hbar} \left[ \Psi \left( \frac{1}{2} + \frac{\tau_B}{2\tau_\phi} \right) - \Psi \left( \frac{1}{2} + \frac{\tau_B}{2\tau} \right) \right] \quad (2.27)$$

where  $\Psi(x)$  is the digamma function, and  $\tau_B = \frac{\hbar}{2DeB}$  is the timescale of diffusive motion. This equation is valid only in a very weak magnetic field, where  $\frac{2\tau}{\tau_B} \ll l$ . The magnetoconductivity is given by

$$\Delta\sigma(B) = \delta\sigma(B, T) - \delta\sigma(0, T) \quad (2.28)$$

$$= \frac{e^2}{2\pi^2\hbar} \left[ \Psi \left( \frac{1}{2} + \frac{\tau_B}{2\tau_\phi} \right) - \Psi \left( \frac{1}{2} + \frac{\tau_B}{2\tau} \right) + \ln \left( \frac{\tau_\phi}{\tau} \right) \right] \quad (2.29)$$

Altshuler et al. [39] also considered the case of  $L_\phi > W$  (In one dimension), and obtain the following correction to the conductance:

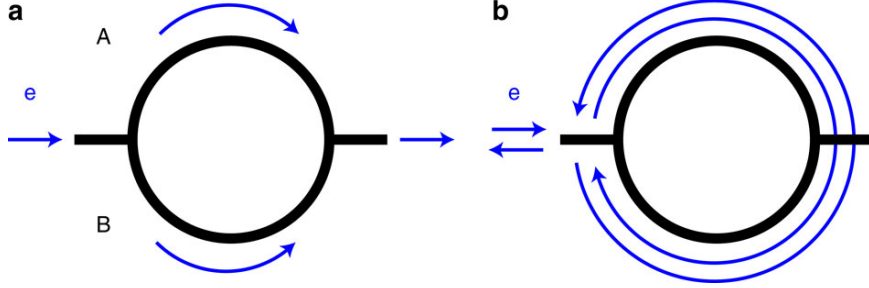


Figure 2.4: Schematic of an Aharonov-Bohm ring showing the interference trajectories that cause  $\frac{h}{e}$  oscillations (left) and  $\frac{h}{2e}$  oscillations (right).

$$\delta G(B) = -\frac{e^2}{\pi\hbar L} \left( \frac{1}{D\tau_\phi} + \frac{1}{D\tau_B} \right)^{-\frac{1}{2}} \quad (2.30)$$

Here  $L$  is the sample length in one dimension, and  $\tau_B = (3\hbar^2)/D(eBW)^2$ .

The magnetoconductance can be written as

$$\Delta G(B) = \delta G(B) - \delta G(0) \quad (2.31)$$

$$= \frac{e^2}{\pi\hbar L} \left[ L_\phi - \left( \frac{1}{D\tau_\phi} + \frac{1}{D\tau_B} \right)^{-\frac{1}{2}} \right] \quad (2.32)$$

This expression requires that the magnetic length exceeds  $W$ . If the magnetic length is shorter than  $W$ , the 2D magnetoconductance will be recovered. In all discussions of this topic, the mean free path is assumed to be much shorter than  $W$ , so that boundary scattering can be neglected. However, boundary scattering must be considered in high mobility samples.

In 1959, Aharonov and Bohm conducted an experiment that unequivocally justified the interference effect of weak localisation. They considered

that a partial wave of the electrons encloses a magnetic potential, and undergoes a phase shift. The interferences as a function of the phase shift is the well-known Aharonov-Bohm (AB) effect [40]. The AB effect can be testified by the ring pattern on the 2DEG shown in Figure 2.4. The circumference of the ring must be smaller than the phase coherence length. As the magnetic field varies, the resistance behaviour the ring oscillates with a period of  $h/e$ . If the phase breaking length is large, the two partial waves will interfere from the beginning (right panel of Figure 2.4). The period of this oscillation is  $h/2e$ , half of the AB effect. This effect is called the Altshuler-Aronov-Spivak (AAS) effect [41].

## 2.5 Bergmann's approach

Bergmann [33,42] physically interpreted weak localisation in reciprocal space rather than in real space. In his approach, a plane wave scattered by impurities builds up an echo in the backward direction.

Bergmann considered an electron with momentum  $k$  in  $k$ -space at  $t = 0$ . The probability of this electron scattering to the  $-k$  state is represented by a scattering sequence of momentum transfers  $k_1, k_2, k_3, \dots, k_n$ . With equal probability, the electron can be scattered from  $k$  state to the  $-k$  state by reverse sequence  $k_n, k_{n-1}, k_{n-2}, \dots, k_1$ . These complementary scattering series have identical changes of momentum and phase. As in the real space description, the total intensity of the final state is  $4|A|^2$ . For states that are sufficiently far from  $-k$ , an incoherent superposition with an intensity of  $2|A|^2$  occurs at every two sequences. The coherent backscattering eventually terminates after a time  $\tau_\phi$  by some inelastic mechanism, as expected. The

original momentum decays within the elastic time  $\tau$ , and is echoed in the opposite direction at some later time, diminishing and finally vanishing at  $\tau_\phi$ . The magnitude of the conductivity correction is calculated by finding the coherent fraction of the total area available for scattering in the  $k$ -space, and integrating this fraction with a time interval  $\tau \leq t \leq \tau_\phi$ . Coherent backscattering is not restricted to the exact state  $-k$ , but is also contributed by a small area with a radius of  $q$  around  $-k$  (Because the approach is considering in  $k$ -space, the  $q$  here is also a momentum). To determine the size of this region, we note that the electron diffuses a distance  $L = \sqrt{Dt}$  in time  $t$ . Therefore, the uncertainty in the momentum of this small area is  $\hbar q = \hbar/L$ , and interfere within the range  $-k \pm q$ .

In 2D, this effect manifests as a backscattering circle of area  $\pi q^2 = \pi/L^2$ . In narrow 2D systems, the wavenumber uncertainties in the directions parallel and perpendicular to the channel are given by  $\Delta k_x = 1/\sqrt{Dt}$  and  $\Delta k_y = 1/W$ , respectively. The backscattering region becomes an ellipse with area of  $\pi/W\sqrt{Dt}$ . To determine the total area available for scattering in  $k$ -space, we note that elastic scattering broadens the Fermi surface  $1/l$ . Therefore, the total scattering area of the 2D density of states is  $2\pi k_F/l$ .

The coherent fraction is then

$$I_{coh} = \frac{l}{2k_F W \sqrt{Dt}} \quad (2.33)$$

Integrating Eq.(2.33) between  $\tau_\phi$  and  $\tau$ , we get

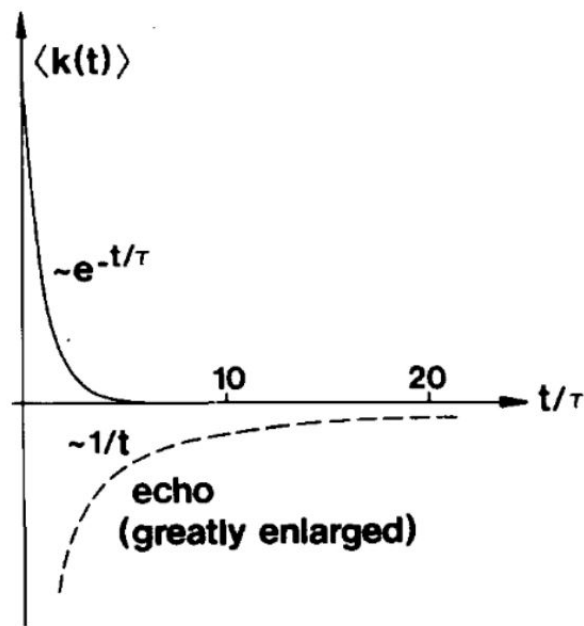


Figure 2.5: Contribution of an electron in state  $k$  to the momentum as a function of time. The original state and its momentum decay exponentially within time  $\tau$  (assuming  $s$  scattering). An echo with momentum  $-k$  is formed, which decays as  $1/t$ . And this echo reduces the electron's contribution to the current, the resistance must increase proportionally to  $\log(t/\tau)$  [42].

$$\delta\sigma = \frac{ne^2}{m} \frac{l}{2\pi k_F W \sqrt{D}} \int_{\tau}^{\tau_{\phi}} \frac{l}{\sqrt{t}} dt \quad (2.34)$$

$$\approx \frac{e^2}{\pi\hbar} L_{\phi} \quad (2.35)$$

In the presence of a magnetic field  $B$ , the coherent backscattering contribution is obtained by integrating between  $\tau$  and  $\tau_B = \hbar/4DeB$ , assuming that  $\tau_B < \tau_{\phi}$ . Constructive interference is suppressed over a time proportional to  $1/B$ , and reduces the field to  $B'$ . By these phenomena, we can observe the backscattering between  $\tau_B$  and  $\tau_{B'}$ .

## 2.6 Spin-orbit interaction

In perfect lattices, the spin-orbit interaction can be ignored. However, in real systems, any defects will induce spin-orbit interactions of the electrons. When the spin coherence time  $\tau_{SO}$  is much longer than the phase coherence time  $\tau_{\phi}$ , the correction due to the spin-orbit interaction is very small. If the spin-orbit interaction is sufficiently strong, then  $\tau_{SO} < \tau_{\phi}$ , and positive magnetoresistance arises in a weak magnetic field.

The effects of spin-orbit interactions on magnetoresistance in 2D systems were investigated by Hikami et al. in 1980 [38]. They showed that

$$\delta\sigma(B) = -\frac{e^2}{2\pi^2\hbar} \left[ \Psi\left(\frac{1}{2} + \frac{B_1}{B}\right) - \frac{3}{2}\Psi\left(\frac{1}{2} + \frac{B_2}{B}\right) + \frac{1}{2}\Psi\left(\frac{1}{2} + \frac{B_3}{B}\right) \right] \quad (2.36)$$

where

$$B_1 = B_\tau + B_{\tau_{SO}} + B_{\tau_s} \quad (2.37)$$

$$B_2 = \frac{4}{3}B_{\tau_{SO}} + \frac{2}{3}B_{\tau_s} + B_{\tau_\phi} \quad (2.38)$$

$$B_3 = 2B_{\tau_s} + B_{\tau_\phi} \quad (2.39)$$

The fields  $B_\tau, B_{\tau_\phi}, B_{\tau_{SO}}, B_{\tau_s}$  are the effective magnetic fields of elastic scattering, inelastic scattering, spin-orbit scattering and spin scattering, respectively, with  $B = \hbar/4Det(t = \tau, \tau_\phi, \tau_{SO} \text{ or } \tau_s)$ .

Magnetic scattering arises from interactions between the electrons and magnetic impurities. By perturbing the Hamiltonian, Bergmann derived the magnetic scattering time as a function of the electron spin,  $S$ , and the magnetic impurity spin,  $I$ ,

$$\tau_s = \frac{\hbar}{2\pi N(E_F)n_i I^2 S^2} \quad (2.40)$$

where  $N(E_F)$  is the density of states at the Fermi level, and  $n_i$  is the magnetic impurity concentration. In the absence of magnetic impurities,  $B_{\tau_s}$  is generally set to 0.

## 2.7 Electron interactions

Localisation theories neglect the electron-electron interactions in the system. A system with strongly interacting electrons can be modelled by Fermi-liquid theory. Altshuler and Aronov [43,44] investigated the interactions in a disor-

dered Fermi liquid. As quasiparticle motion is diffusive, the electrons spend extended time in a region, which enhances their Coulomb interactions. Consequently, the energy levels shift and broaden, forming a small dip of density-of-states near the Fermi level. This dip is observed only at temperatures low enough for the occurrence of electron-electron interactions.

Altshuler and Aronov [45] also corrected the conductivity for the following phenomena:

1. Interactions in diffusion channels

2. Interactions in Cooper channels

### 2.7.1 Interactions in diffusion channels

Diffusion channel interactions are the dominant form of electron-electron interactions in doped semiconductors. To correct for this effect, we introduce the interaction parameter  $F$ , defined as the average of the static screened Coulomb potential over the Fermi surface measures the importance of screening. Altshuler and Aronov derived the conductivity correction in one, two and three dimensions as follows:

$$\delta\sigma_d(T) = x \frac{e^2}{4\pi^2\hbar} \left( \frac{4}{d} + \frac{3}{2} \lambda_\sigma^{j=1} \right) \left( \frac{k_B T}{\hbar D} \right)^{\frac{d}{2}-1} \quad (2.41)$$

$$x = \begin{cases} 0.915, & d = 3 \\ \ln\left(\frac{k_B T \tau}{\hbar}\right), & d = 2 \\ -4.91, & d = 1 \end{cases} \quad (2.42)$$

where

$$\lambda_\sigma^{j=1} = \begin{cases} \frac{32}{d(d-2)} \frac{1 + \frac{F}{4} d - \left(1 + \frac{F}{2}\right)^{\frac{d}{2}}}{F}, & d = 1, 3 \\ 4 \left[ 1 - \frac{2\left(1 + \frac{F}{2}\right) \ln\left(1 + \frac{F}{2}\right)}{F} \right], & d = 2 \end{cases} \quad (2.43)$$

The strong and weak screening limits are defined by  $F = 0$  and  $F = 1$ , respectively. The static limit of the screened Coulomb potential manifests from the of Hartree process, which involves momentum transfer up to  $2k_F$ . As discussed by Fukuyama [46], the interaction dynamics play a minor role in large momentum transfer, so they can be ignored.

## 2.7.2 Interactions in Cooper channels

Electronic attractions in Cooper channels, lead to superconducting states. Even when  $T > T_c$ , interactions in the metallic state perturb the superconductivity. Altshuler and Aronov [45] showed that Cooper channel interactions reduce the conductivity by  $\ln(E_F/k_B T)$ . They calculated the correction factors in one, two and three dimensions as follows,

$$\delta\sigma_d(T) = x \frac{e^2}{2\pi^2\hbar} \left( \frac{k_B T}{\hbar D} \right)^{\frac{d}{2}-1} \quad (2.44)$$

$$x = \begin{cases} \frac{0.915}{\ln\left(\frac{E_F}{k_B T}\right)}, & d = 3 \\ \ln\left(\frac{k_B T \tau}{E_f \hbar}\right), & d = 2 \\ \frac{-4.91}{\ln\left(\frac{E_F}{k_B T}\right)}, & d = 1 \end{cases} \quad (2.45)$$

A second correction for Cooper channel interactions is the Maki-Thomson term [45]. This correction is always opposite in sign to the weak localisation correction, but is much smaller. Indeed, the Maki-Thomson is much smaller than the above Derived by Altshuler and Aronov.

## 2.8 Magnetoresistance of interaction effects

A magnetic field  $B$  produces the Zeeman spin splitting subbands. The bandgap between lowest unoccupied spin-up and highest occupied spin-down subbands is  $g\mu_B B$ , where  $g$  is the Landé  $g$ -factor and  $\mu_B$  denotes the Bohr magneton. Magnetic field interactions suppress the contribution of the magnetic field to the conductance correction.

The conductivity differential in a magnetic field is written as

$$\delta\sigma_d(B) = \delta\sigma_d(T) - \delta\sigma_d(B, T) \quad (2.46)$$

The field dependent terms  $\delta\sigma_d(B, T)$  in three and two dimensions were determined by Lee and Ramakrishnan [47] as

$$\delta\sigma_d(B, T) = \begin{cases} -\frac{e^2 F g_{3d}(B)}{4\pi^2 \hbar} \sqrt{\frac{k_B T}{\hbar D}}, & d = 3 \\ -\frac{e^2 F g_{2d}(B)}{4\pi^2 \hbar}, & d = 2 \end{cases} \quad (2.47)$$

where  $F = -\delta\sigma_i''(B, T)$ . The respective numerically limiting behaviours are

$$g_{3d}(B) = \begin{cases} \sqrt{\frac{g\mu_B B}{k_B T}} - 1.3, & \text{when } \frac{g\mu_B B}{k_B T} \gg 1 \\ 0.053 \times \left(\frac{g\mu_B B}{k_B T}\right)^2, & \text{when } \frac{g\mu_B B}{k_B T} \ll 1 \end{cases} \quad (2.48)$$

and

$$g_{2d}(B) = \begin{cases} \ln\left(\frac{g\mu_B B}{1.3k_B T}\right), & \text{when } \frac{g\mu_B B}{k_B T} \gg 1 \\ 0.084 \times \left(\frac{g\mu_B B}{k_B T}\right)^2, & \text{when } \frac{g\mu_B B}{k_B T} \ll 1 \end{cases} \quad (2.49)$$

The magnetoresistance is non-negligible only when  $g\mu_B B > k_B T$ . Under this condition, the field is much larger than the magnetoresistance of the weak localisation,  $B = \hbar/4De\tau_\phi$ .

Altshuler et al. [45, 48] defined the characteristic magnetic field as

$$B > \frac{k_B T}{2eD} \quad (2.50)$$

denoting that a positive magnetoresistance arises in diffusive channels.

## 2.9 Inelastic scattering

At very low temperatures, electrons remain in one state for a finite time,  $\tau_{in}$ , called the inelastic scattering time. Thereafter, the electrons scatter to other states. The phase coherence time obtained by measuring the negative magnetoresistance, is associated with the inelastic life-time of the quantum interference, and it is the shortest inelastic relaxation time in the system. The inelastic scattering mechanisms can be understood from the behaviour of  $\tau_\phi$ .

### 2.9.1 Electron-electron scattering

Electron-electron scattering dominates in semiconductor systems at low temperatures. In the clean limit,  $k_F l \gg 1$ , the scattering time is proportional to  $T^2$ . Baber predicted this effect in 1937 [49]. He also proposed that an electron with energy close to the Fermi energy can transfer its momentum to another nearby electron within  $k_B T$ ; otherwise, a fraction of the electron-electron collisions exist in an occupied state. The scattering time is given by

$$\tau_{in} = A \frac{\hbar E_F}{(k_B T)^2} \quad (2.51)$$

This idea was elaborated by Abrahams [50], who obtained

$$\tau_{in} = \frac{1}{n\pi a_0^2 v_F} \frac{\hbar E_F}{(k_B T)^2} \quad (2.52)$$

in 3D electron gases. Here,  $n$  is the carrier concentration in units of  $10^{17}m^{-3}$ , and  $a_0$  is the Bohr radius.

Schimid [51] argued that in the above calculations, the mean free path of the electrons is assumed to be infinite. He considered the effect of impurity scattering in 3DEG, and extended the Landau-Baber scattering for large momentum transfers to small momentum transfers. He calculated the electron scattering time for the electrons whose energy  $E$  above the Fermi level  $E_F$ , at  $T = 0$  as

$$\frac{1}{\tau_{in}} = \frac{\pi E^2}{8\hbar E_F} + \frac{3E^{\frac{3}{2}}}{2\hbar(k_F l)^{\frac{3}{2}}\sqrt{E_F}} \quad (2.53)$$

Eq.(2.53) can be rewritten in terms of the temperature:

$$\frac{1}{\tau_{in}} = A \frac{(k_B T)^2}{\hbar E_F} + B \frac{(k_B T)^{\frac{3}{2}}}{\hbar(k_F l)^{\frac{3}{2}}\sqrt{E_F}} \quad (2.54)$$

A similar result was obtained by Altshuler and Aronov [44].

The correction for disorder in 2DEG is derived similarly. Specifically, Abrahams et al. [52] and Fukuyama and Abrahams [53] obtained

$$\frac{1}{\tau_{in}} = A \frac{k_B T}{k_F l} \ln \left( \frac{T_0}{T} \right) \quad (2.55)$$

where  $T_0 = \frac{\hbar}{k_B \tau}$ ,  $\tau$  is the elastic scattering rate from the static disorder. Abrahams et al. [54] also obtained

$$\frac{1}{\tau_{in}} = \frac{k_B T}{2\pi\hbar DN(E_F)} \ln(\pi\hbar DN(E_F)) \quad (2.56)$$

which was confirmed in 2D disordered systems by Fukuyama [55].

Isawa [56] suggested that in 2D systems, the  $T^{\frac{3}{2}}$  term in 3D systems becomes linear in  $T$ . He predicted this crossover occur at the temperature given by

$$T_c = 0.166 \frac{\hbar}{k_B \tau} \quad (2.57)$$

## 2.9.2 Electron-phonon scattering

Electron-phonon scattering makes a small contribution to inelastic scattering at low temperatures. Price [57] determined the scattering time by acoustic phonons in 2DEG as

$$\frac{1}{\tau_{ep}} = \left[ \frac{m^* e E^2 k_B}{\hbar^3 n v^2 d} + 1.46 \times \frac{m^* (e D_{14})^2 k_B}{2\pi \hbar^3 n v^2 k_F} \right]^T \quad (2.58)$$

where  $n$  is the density,  $v$  is the longitudinal velocity,  $D_{14}$  is the piezoelectric coefficient and  $d$  is the effective thickness of the 2DEG.

Bergmann [33] refined electron-phonon scattering in 2DEG by considering a finite mean free path. The inelastic lifetime (inelastic scattering time) was obtained as

$$\frac{1}{\tau_{in}} = 2.47 \times \frac{n(k_B T)^2}{2Mm^*v^3l} \quad (2.59)$$

where  $M$  is the mass of the ion.

Localised electrons conduct in a non-metallic manner. Classically, this phenomenon is modelled by Mott's ' $T^{1/4}$  law', which expresses the conductivity in terms of localised quantum states.

$$\sigma(T) = \sigma_0 \cdot \exp \left[ - \left( \frac{T_0}{T} \right)^{\frac{1}{4}} \right] \quad (2.60)$$

where  $T_0 = \frac{18}{k_B N(E_F) e^3}$ .

The conductivity can be envisaged by a phonon-assisted hopping mechanism. Hopping occurs when localised states are energetically close to each other, but have small localisation lengths relative to the spatial distance between their localisation centres.

At low temperatures, the hopping probability  $p$  between the states is proportional to the overlap integral of the two wavefunctions, which is an exponentially decreasing function of their spatial separation  $R$ , and a Boltzmann factor defining their mean energetic separation  $\Delta$

$$p \propto \exp(-\alpha R - \beta \Delta) \quad (2.61)$$

Here,  $\alpha$  is proportional to the inverse of the exponential decay length of the states, and  $\beta$  is the inverse temperature. If the hopping range  $R$  is small, a large hopping probability requires a small energy separation of the states available for the hopping process. If the mean energy separation of the states is large, the hopping probability is reduced by the Boltzmann factor. Conversely, when  $R$  is large, there are many states available for hopping from a given site, and the hopping probability is enhanced by increasing  $\Delta$ . To maximise  $p$ , we must know how  $\Delta$  depends on  $R$ .

Assuming that the localisation centres are distributed homogeneously in space, we estimate  $\Delta$  (the energy separation in a  $d$ -dimensional system) as

$$\Delta \propto \frac{1}{R^d n(E_F)} \quad (2.62)$$

To obtain the distance  $R_{max}$  that maximises  $p$ , we then minimise the exponent

$$R_{max} = \left( \frac{d\beta}{dn(E_F)} \right)^{\frac{1}{d+1}} \quad (2.63)$$

By inserting this result into Eq.(2.60), we obtain the  $d$ -dimensional version of Mott's law

$$\sigma(T) = \sigma_0 \cdot \exp \left[ - \left( \frac{T_0}{T} \right)^{\frac{1}{d+1}} \right] \quad (2.64)$$

## 2.10 Phase coherence

The phase coherence time  $\tau_\phi$  is the time during which the wavefunctions retain coherence. It is the shortest physical inelastic scattering time in systems.

As noted by Fukuyama and Abrahams [53], the phase coherence time  $\tau_\phi$  in weak localisation is not the electron-electron collision time  $\tau_{in}$ , discussed in the previous section. In 3D systems with large energy transfer between the electron collisions, the phase coherence time is very close to  $\tau_{in}$ , but in lower dimensions, these times largely differ because electron scattering with small energy transfer makes an important contribution. As the energy transfer decreases, elastic or quasi-elastic collisions become increasingly less effective at destroying the phase coherence, and more scattering events are required. Altshuler et al. [54] reported that the low-energy scattering is equivalent to the interaction of an electron with a fluctuating electromagnetic field generated by other electrons, the so-called Nyquist noise. They derived a phase coherence time of the form

$$\frac{1}{\tau_N} \sim \left[ \frac{k_B T}{\hbar^2 D^{\frac{d}{2}} N(E_F)} \right]^{\frac{2}{4-d}} \begin{cases} \ln(\pi \hbar D N(E_F)), & d = 2 \\ 1, & d = 1 \end{cases} \quad (2.65)$$

From this equation, we obtained

$$\frac{\tau_N}{\tau_{in}} \sim \left( \frac{k_B T \tau_N}{\hbar} \right)^{\frac{d-2}{2}} \quad (2.66)$$

Provided that  $\frac{k_B T \tau_N}{\hbar} \gg 1$ ,  $\tau_N$  is shorter than  $\tau_{in}$  for  $d \leq 2$ , and the phase

coherence time  $\tau_\phi \equiv \tau_N$ . In two dimensions, Altshuler and Aronov [45] obtained

$$\frac{1}{\tau_N} = \frac{k_B T}{\pi \hbar^2 D N(E_F)} \ln(\pi \hbar D N(E_F)) \quad (2.67)$$

$$= \frac{k_B T}{\hbar k_F l} \ln(k_F l) \quad (2.68)$$

In one dimension, they showed that

$$\frac{1}{\tau_N} = \left( \frac{\sqrt{D} e^2 k_B T}{\hbar^2 G L} \right)^{\frac{2}{3}} \quad (2.69)$$

where  $G$  and  $L$  are the conductance and length, respectively. The phase coherence length is then given by

$$L_N = \sqrt{D \tau_N} = \left( \frac{\hbar^2 D G L}{e^2 k_B T} \right)^{\frac{1}{3}} \quad (2.70)$$

Altshuler and Aronov further derived the change in conductance per unit length

$$\delta G = \frac{e^2}{\pi \hbar} L_N \frac{1}{\ln \left[ A_i \left( \frac{L_N}{L_\phi} \right)^2 \right]} \quad (2.71)$$

where  $A_i(x)$  is the Airy function, which is associated with phase coherence mechanisms rather than Nyquist noise. If  $\tau_N \ll \tau'_\phi$ , we have

$$\delta G \approx 0.62 \times \frac{e^2}{\hbar} L_N \quad (2.72)$$

If  $\tau_N \gg \tau'_\phi$ ,

$$\delta G = -\frac{e^2}{\pi\hbar} L'_\phi \left[ 1 - \left( \frac{\tau'_\phi}{\tau_\phi} \right)^{\frac{3}{2}} \right] \quad (2.73)$$

Because  $\tau_N$  is not independent of  $\tau'_\phi$ , the total scattering time is not the simply sum of the inverse of two terms. This result indicates that the phase coherence events are broken after (not during) the quasielastic collisions.

To summarise the above, 3D systems are dominated by large energy transfer processes, and  $\tau_\phi \equiv \tau_{in}$ . In 2D and 1D systems, where  $k_B T \tau_\phi \gg \hbar$ , we have  $\tau_\phi \equiv \tau_N$  with  $\tau_N^{-1} \sim T^{\frac{2}{4-d}}$ . Because the electron-electron interactions enter the weak localisation regime in lower dimensions, the quantum interferences and electron-electron interactions are dimension-dependent. If the phase coherence length exceeds the width of the sample (i.e.  $L_\phi > W$ ), the quantum interference corrections are those of a 1D system; conversely, if the thermal length  $L_T = \sqrt{\hbar D / k_B T} < W$ , the magnitude and temperature dependence of  $L_\phi$  are governed by 2D equations.

## 2.11 Narrow Devices

Some of the earliest work on narrow systems was carried out in narrow metal films and fine wires. However, although these structures are easily fabricated, interpreting their results is complicated by spin-orbit scattering, magnetic impurity (or spin-flip) scattering, and superconducting fluctuations, which readily occur in metals.

Giordano et al [58] fabricated narrow wires of  $Au_{60}Pd_{40}$  with cross sectional areas ranging from  $30nm^2$  to  $200nm^2$ . They employed a step-edge shadowing method in which the metal is evaporated over a reactive ion-etched step on a substrate material. All metal not shadowed by the step is then removed by angled ion-beam milling. The cross-sectional area of the wire is controlled by varying the substrate step size. At a similar time, Chaudhari and Habermeier [59] investigated narrow films of amorphous  $W - Re$  defined by electron-beam lithography, achieving areas as small as  $25nm \times 10nm$ . White et al [60] fabricated wires of  $Cu$ ,  $Ni$  and  $AuPd$ , with cross sections down to  $22nm \times 20nm$  by the step-edge shadowing technique. They found a relationship  $\Delta R/R \sim T^{-1/2}$ , consistent with the one-dimensional form of the electron-electron interaction correction (Eq. 2.41), and with results of Giordano et al [58] and Chaudhari and Habermeier [59]. However, if these results are true, the localisation correction is rather small. Santhanam et al [61] attributed this small correction to strong spin-orbit or magnetic scattering.

Later, Giordano et al studied the temperature dependencies of thin  $Pt$  wires fabricated by step-edge technique [62]. More recent, they extended their work on  $AuPd$  wires separating the quantum interference and interaction effect by magnetoresistance [63]. They observed a positive magnetoresistance

indicating a strong spin-orbit interaction. To extract the electronic phase coherence time due to electron scattering, they fitted the magnetoresistance traces to a generalised equation describing for the spin-orbit and magnetic impurity scattering, and approximated the two scattering times. The phase coherence time was well fitted to a power law of the form  $T^{-2/3}$ , exactly as predicted for electron-electron scattering with small energy transfers in the 1D limit (the Nyquist rate Eq. 2.69 in Section 2.10). The magnitude also satisfactorily agreed with the theory. Lin and Giordano [64] claimed to have reported the first observation of the Nyquist mechanism. The zero field temperature dependence  $\sim T^{-1/2}$  of Nyquist rate was ascribed to interactions.

Wind et al [65] questioned these conclusions, pointing out that the wires were wider than the length scales of both magnetic and spin-orbit scattering, so the 1D localisation theory could not apply (this idea was further discussed by Lin and Giordano [64]). Wind et al. also mentioned that the wire was wider than the thermal length  $L_T$  throughout the entire temperature range, so electron-electron scattering was also outside of the 1D limit. They argued that the above studies do not unambiguously demonstrate the 1D Nyquist rate, and that the interaction correction should be considered as two-dimensional. Their own studies were performed on *Al* and *Ag* wires of thickness  $20nm$  and width 35 to  $110nm$  defined by electron beam lithography. Satisfied that their wires were sufficiently one-dimensional, they fitted their magnetoresistance data to the 1D form, accounting for spin-orbit scattering, Maki-Thompson superconducting fluctuations in *Al*, and magnetic scattering in *Ag*. The phase-breaking rate was well described by a combination of electron-phonon scattering and the Nyquist mechanism. Their results also

matched the width dependence predicted by Eq. 2.69.

Heraud et al. [66] examined *AuPd* wires of rectangular cross - section with widths between 25 and 40nm, again defined by electron beam lithography. Considering the strong spin-orbit scattering, they fitted their magnetoresistance data to an equation involving a 3D spin-orbit term, and a 1D length determined by inelastic and magnetic scattering. They noted that the electron-electron scattering time  $\tau_\phi$  cannot be unambiguously decided without assuming a value for the exponent in the temperature dependence of the scattering time. Their data  $\tau_\phi$  were equally well fitted to a phase breaking process governed by the Nyquist mechanism ( $\tau_\phi \sim T^{-2/3}$ ), and to the large-energy transfer process,  $\tau_\phi \sim \tau_{ee} \sim T^{-1/2}$ . Analysing Wind et al.'s [65] data, they arrived at the same conclusions. Thus, although wires are sufficiently thin to reach the one-dimensional regime, whether the Nyquist mechanism applies is debatable.

Santhanam et al [67] reviewed their work on narrow *Al* films defined by X-ray contact printing. They concluded that although the wires satisfy a one-dimensional quantum interference correction, their phase coherence times are identical to those of their co-evaporated 2D films, because their width exceeds the thermal length  $L_T$ . Thus, with regard to electron-electron scattering regime, wires are two-dimensional. Gordon [68] reported the same behaviour, consolidating the mixed dimensionality effect.

## 2.12 Heterostructures

Quantum conductivity corrections are better tested in the 2DEG of *GaAs/Al-GaAs* heterostructures than in wires. These gases have negligible spin-orbit

coupling, are apparently free of magnetic impurities and are not complicated by superconducting fluctuations. Therefore, the data can be fitted without requiring additional adjustable parameters, and the experiment can access a wide temperature range. At sufficiently low temperatures, electron-phonon scattering is suppressed and all dephasing occurs by electron-electron scattering, allowing direct comparison with theory.

The *GaAs/AlGaAs* heterostructure system is advantaged by high mobility and a simple band structure. Choi et al. [69, 70] etched heterostructures into channels with widths between 1.1 and  $156\mu m$ . They investigated the quantum corrections for electron-electron interactions as functions of width and length under classically strong magnetic fields (which completely suppress the weak localisation). When the width and the thermal length were of the same order of magnitude, the interaction correction transitioned from 2D to 1D. A similar condition for the heterostructure length induced a transition from 2D to 0D (a temperature independent regime). When the width is below the elastic mean free path  $l$ , boundary scattering becomes important and leads to significant deviations in the electron-electron interaction behaviour.

Thornton et al [71] investigated the narrow channels formed by the split-gate of a *GaAs/AlGaAs* heterojunction FET. In this system, the electron gas is confined by applying of a negative gate bias with a  $0.06\mu m$  gap, defined by electron beam lithography. The low field magnetoresistance fitted the 1D model, and the estimated channel width at a gate bias of  $-1.2V$  was  $45nm$ . The magnitude and temperature dependence of the phase coherence length  $L_\phi$  were consistent with the Nyquist mechanism, scaling as  $L_\phi \sim T^{-1/3}$ . The interaction correction also agreed with the 1D model. Increasing the reverse

bias on the gate strengthened the temperature dependence, suggesting a transition to strong localisation. Higher-field magnetoconductance depopulates the 1D subbands [72]. Zheng et al. [73] also studied the split-gate device, but did not achieve the 1D limit of electron-electron scattering.

# Chapter 3

## Experimental Techniques

This chapter introduces the experimental techniques involved in fabricating the nanostructure samples and measuring their transport properties. Section 3.1 briefly describes the fabrication process. All experimental results were obtained at low temperatures (below  $4.2K$ ; the temperature of liquid helium). Section 3.2 introduces the concepts and techniques of generating this low temperature environment, and Section 3.3 describes the techniques for measuring the electrical transport properties of the nanostructure samples.

### 3.1 Fabrication techniques

Fabricating the nanostructures is a major challenge in mesoscopic transport experiments. The quality of the fabrication, which directly affects the experimental results, depends on the material purity, lithographic resolutions and many other factors. The major processes of fabrication are wafer growth and patterning.

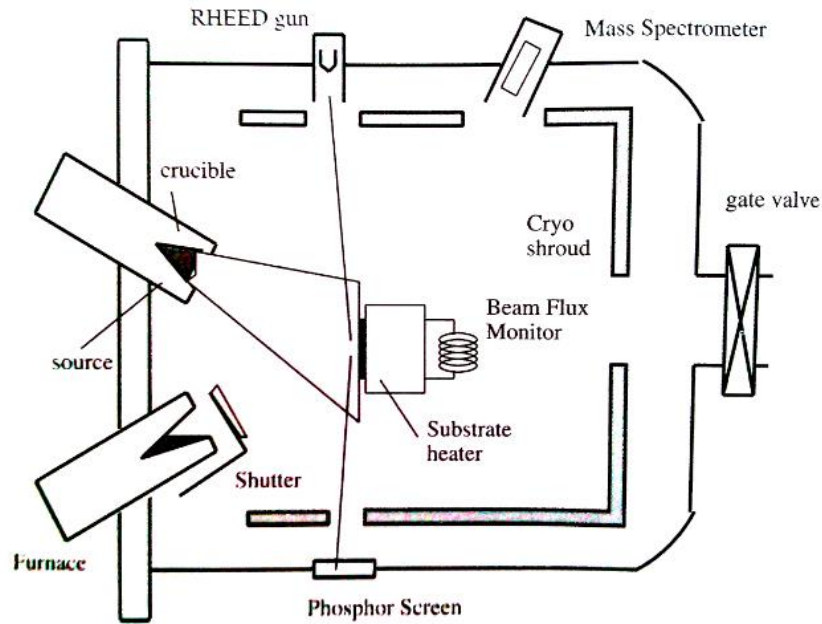


Figure 3.1: Schematic of a molecular beam epitaxy growth chamber

### 3.1.1 Wafer growth

There are two techniques for growing III-V semiconductor devices: chemical vapour deposition (CVD) and molecular beam epitaxy (MBE). In the CVD process, the substrate is mounted in a vacuum chamber, and the atoms of the semiconductors to be grown are introduced via suitable molecular gas flows. The molecules crack at the surface and deposit the semiconductor atoms on the substrate. CVD is a low-cost technique, but is disadvantaged by the high toxicity of the gases involved in the deposition. In addition, the grown material is not clean, and its interface is rougher than an MBE-formed interface.

The MBE growth technique deposits a specific number of atomic layers on the substrate. The formed interfaces are abrupt, both in material composition and their intentional impurity-doping profiles. The epitaxial growth

occurs in an ultra-high vacuum chamber with its base pressure maintained at  $10^{-8}$  to  $10^{-10}$  torr. The high vacuum chamber is illustrated in Figure 3.1. A starting GaAs wafer is mounted on the substrate heater, which heats the substrates to approximately  $600^\circ\text{C}$ . The target substrate is faced with multiple (typically eight) effusion cells (or furnaces) containing different solid source materials. Each effusion cell heats the source material to its melting temperature, and ejects it through a shutter that opens once the melting temperature is reached. Because the chamber is maintained at ultra-high vacuum, the evaporated source molecules form separate molecular beams that do not collide, but impinge directly on the semiconductor substrate. The high substrate temperature promotes the diffusion of the impinging molecules around the substrate surface, allowing them to locate proper crystalline sites. The evaporation rate of the source material is determined by the furnace temperature, which is maintained at the desirable values through a thermocouple tapped either at the bottom or around the centre of the crucible. As the switching time of the shutters is much shorter than the growth time of an atomic layer, the number of grown atomic layers is precisely controllable. As shown in Figure 3.1, the flux of each source material approaches a specific part of the substrate at a different angle. To reduce this directional non-uniformity, the substrate is rotated during the growth.

### **3.1.2 Wafer patterning**

The devices used in the experiments were fabricated as split-gate devices in which narrow one-dimensional channels are established in 2DEG.

The pattern of the experimental devices on the wafer is defined by the

photolithography technique. This technique can easily defines the Hall-bar, ohmic contacts and optical gates in very high resolution. Following these procedures, the metallic gates are defined by electron-beam lithography (EBL).

EBL technology is commonly used for fabricating ultra-fine and small structures because of the incomparable high resolution of electron beam. In EBL, the sample surface is coated by an electron-sensitive material and scanned by a focused electron beam. The most popular high-resolution positive resist is polymethyl methacrylate (PMMA), a long chain polymer whose solubility in certain solvents depends on the relative molecular mass of the individual chains. A beam of high-energy electrons cleaves the chains at random sites, reducing the relative molecular mass in the regions exposed to the beam. The resolution of PMMA (approximately  $10nm$ ) cannot be improved by increasing the accelerating voltage or reducing the beam diameters below  $10nm$ . The defined pattern must be developed and transferred from from the resist layer to the material of interest.

Figure 3.2 illustrates the standard photolithography procedure. To coat the sample with the thin photoresist layer, the resist is dropped onto the samples. The sample are then rotated at high speed and baked on a hot plate. Next, the sample is mounted onto a mask aligner illuminated by a strong UV light. Once the photoresist has been hardened and rendered removable by the UV irradiation, it resists etching in chemical etchant solution. The sample is then developed by immersion in suitable etchant solution for an appropriate time.

In the metallisation step, a metal film is deposited on the semiconductor surface. Ohmic contacts are formed by evaporating and alloying a suitable

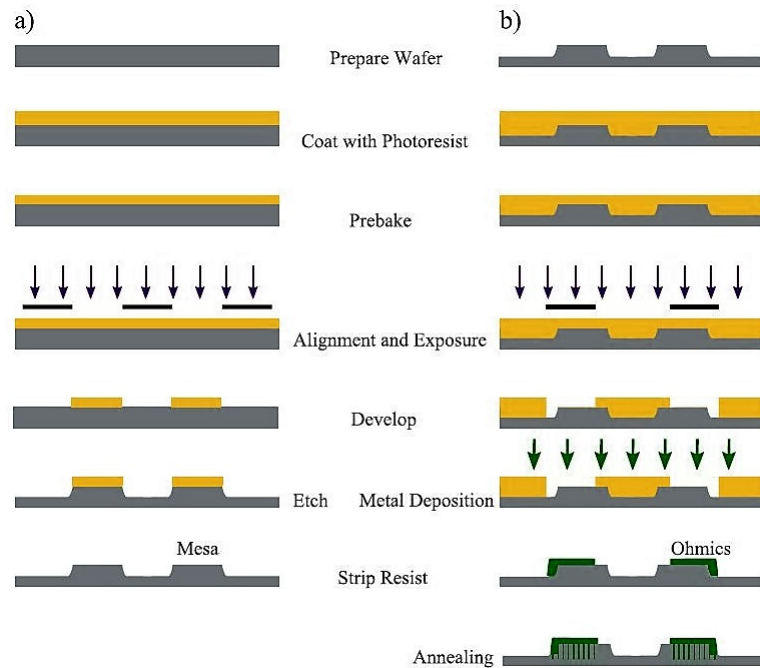


Figure 3.2: Fabrication process using a negative photo-resist of the desired pattern. After deposition of the ohmic material the sample is annealed at an appropriate temperature, allowing diffusion of the ohmic metals into the wafer. (a) Definition of regions containing the 2DEG; (b) fabrication of the ohmic contacts.

metal film on the semiconductor. Normally, evaporation is followed by an annealing process, which can effectively decrease the resistivity of Ohmic contacts.

The last step of fabrication is the fine-gate fabrication. Customised patterns are formed on the sample by a focused electron beam. These patterns are then selective removed by the developing solution. EBL offers much better resolution than photolithography, but requires a longer processing time. The EBL preparation procedures are similar to the fabrication of mesa and ohmic contacts. Before entering the EBL process, the mesa and ohmic contacts should be fabricated on the sample, and the optical gates should be

defined. Before exposure to an electron beam, the device must be coated with polymeric resist (PMMA). For good resist adhesion, the sample surface must also be cleaned with isopropanol (IPA) and completely dried with nitrogen before spinning. To avoid mismatch and to preserve the quality of the EBL-fabricated device, the electron beam must be properly focused and aligned with the sample. The lithography process is followed by development in a 3:1 mixture of IPA: methyl isobutyl ketone (MIBK) solvent. The developed sample is then washed with IPA and blow dried. Finally, the gate is evaporated with an e-beam evaporator and fabricated by lift-off (remove the undefined part of metal deposited on the sample surface). This process is identical to ohmic contact and optical gates fabrication.

## 3.2 Low-temperature techniques

Helium is the only element that remains liquid when cooled to the lowest possible temperature ( $4.2K$ ) under atmospheric pressure. Therefore, helium is the best refrigeration medium for temperature below the condensation temperature of nitrogen ( $77K$ ). The vast majority of mesoscopic transport experiments are performed in this temperature range.

### 3.2.1 $^4\text{He}$ cryostat

Helium cryostats are classified by the two type of their helium isotopes; bosons ( $^4\text{He}$ ) or the fermion ( $^3\text{He}$ ). Temperature below  $4.2K$  can be achieved by pumping liquid  $^4\text{He}$  vapour to a very low pressure using a rotary pump. The vapour pressures reduces the exact temperature of the liquid  $^4\text{He}$  to

$T = 1.2 - 1.6K$ . At such low temperatures, quantum phenomena such as the quantum Hall effect and 1D conductance quantisation can be observed.

### 3.2.2 $^3\text{He}$ cryostat

Temperatures below  $1K$  can be achieved by  $^3\text{He}$ , which has higher vapour pressure than  $^4\text{He}$ . Maintenance at  $0.3K$  requires a much more complicated system than the  $^4\text{He}$  cryostat used to maintain  $1.2 - 1.6K$ .

In a  $^3\text{He}$  cryostat, the  $^3\text{He}$  gas is isolated from the  $^4\text{He}$  pre-cooling stage by an inner vacuum chamber. After most of the gas has condensed into the  $^3\text{He}$  pot, the temperature of the liquid  $^3\text{He}$  (in which the sample is immersed) is approximately  $1.5K$ . Once the  $^3\text{He}$  pot has stably reached this temperature and the condensation is complete, it is further cooled (along with the experimental setup) to below  $300mK$  by an adsorption pump. The measurements were performed at the London Centre for Nanotechnology, using a Teslatron PT  $^3\text{He}$  cryostat with an 8-T superconducting magnet (Oxford Instruments, UK).

### 3.2.3 $^4\text{He}/^3\text{He}$ dilution cryostat

This cryostat exploits the special properties of  $^4\text{He}/^3\text{He}$  mixtures, to achieve temperature of  $10mK$  and even lower. Below some a critical temperature, the  $^4\text{He}/^3\text{He}$  mixture separates into two phases: a concentrated  $^3\text{He}$ -rich phase and a dilute  $^4\text{He}$ -rich phase. The  $^3\text{He}$  concentration in each phase is temperature dependent. The different  $^3\text{He}$  enthalpy in the two phases causes the diffusion of  $^3\text{He}$  from the concentrated to the dilute phase, providing a high cooling power. This process works even at the lowest temperatures

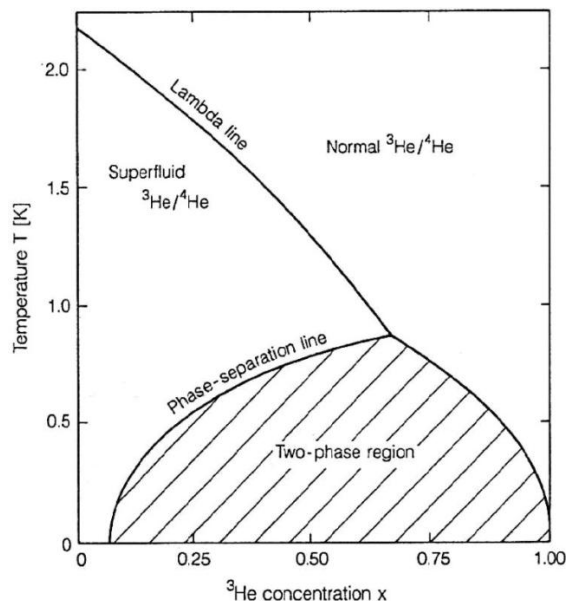


Figure 3.3: Phase diagram of mixed helium  ${}^4\text{He}/{}^3\text{He}$  isotopes. Pure liquid  ${}^4\text{He}$  enters the superfluid phase at  $2.17\text{K}$  (left portion of the figure). The presence of  ${}^3\text{H}$  shifts the superfluid transition to lower temperatures. If the  ${}^3\text{H}$  content is sufficient, the phase separates at low temperatures. At near-zero temperatures, the  ${}^4\text{He}$ -rich phase contains at most 6%  ${}^3\text{H}$  (lower left corner). The other phase comprises essentially pure  ${}^3\text{He}$  (lower right corner).

because the equilibrium concentration of  ${}^3\text{He}$  in the dilute phase is finite down to  $0\text{K}$ .

### 3.3 Measurement techniques

Low-temperature measurements require a very limited signal power to avoid electrons heat-up, typically  $V = 10\mu\text{V}$ , or  $I = 10\text{nA}$ . Therefore, the instruments must employ a very sensitive detection technique, such as the lock-in technique.

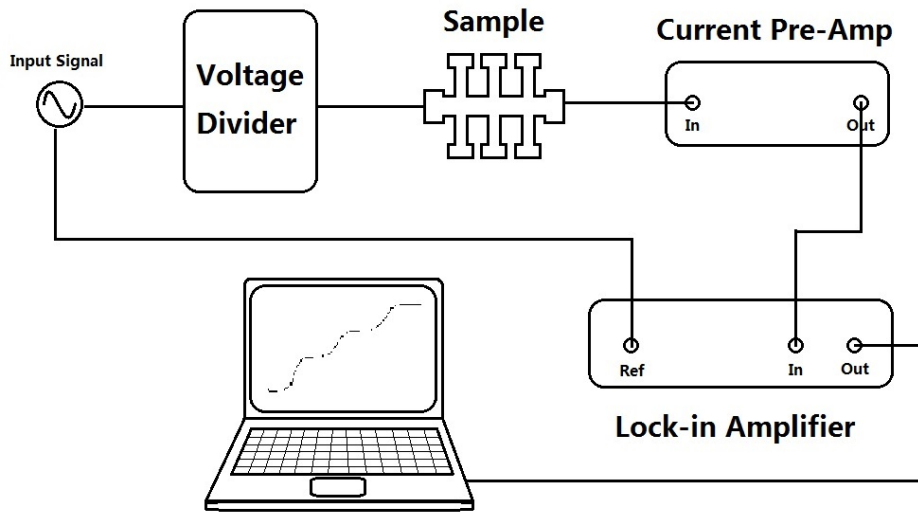


Figure 3.4: Circuit diagram of the two-terminal measurement system, all of the instruments are in one common ground.

### 3.3.1 Two-terminal measurement

Quantized conductance was measured by the two-terminal system as shown in Figure 3.4. The potential divider at the input side sets the AC input voltage (typically  $77\text{Hz}$  in our situation, this is to avoid the harmonic waves from  $50\text{Hz}$  fundamental frequency) to  $V = 10\mu\text{V}$ . The nA-level current flowing through the sample needs to be amplified by a current pre-amplifier before acquisition. The output of the pre-amp is then measured by a lock-in amplifier, which 'locks' the signal at the given reference frequency ( $77\text{Hz}$ ). This signal is transmitted to the LabVIEW CryoMeas program over a general purpose interface bus.

The signal measured by the two-terminal system is proportional to the conductance of the circuit, which is dominated by the sample but is also contributed to by the wires, ohmic contacts, or other components. This

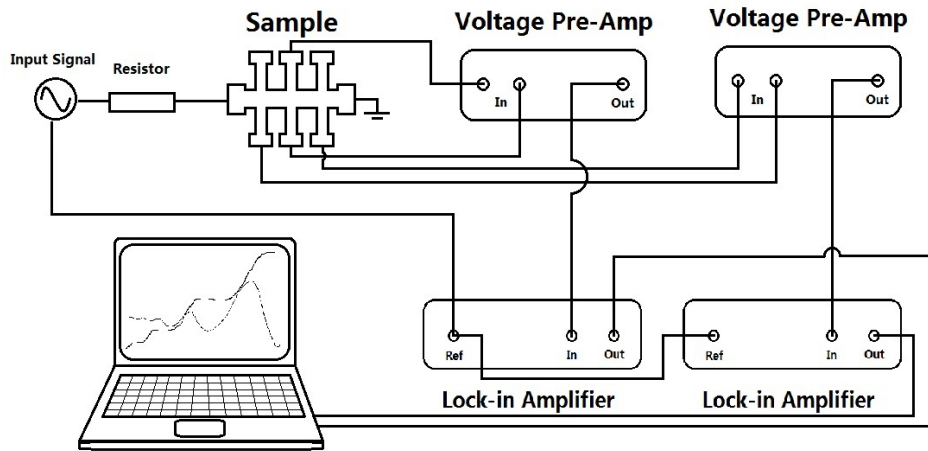


Figure 3.5: Circuit diagram of the four-terminal measurement system, all of the instruments are in one common ground.

additional series resistance must be removed by data post-processing to reveal the actual conductance of the samples.

### 3.3.2 Four terminal measurement

The four-terminal measurement circuit (see Figure 3.5) directly measures the resistance across the sample removing the need for subtracting the series resistance. This system is commonly used for measuring quantum Hall effects and Shubnikov-de Haas oscillations, which manifest as transverse and longitudinal resistance, respectively.

To deliver a sufficiently small constant current ( $I \leq 10$  nA) for measuring the voltage variance in both transverse and longitudinal directions, a very large resistance ( $100$  M $\Omega$ ) is required. The voltage pre-amps in Figure 3.5 amplify the signal prior to lock-in amplifier.

# Chapter 4

## Magneto-transport in GaAs/AlGaAs Heterojunctions

Transport in quasi one-dimensional disordered systems has become a very active research field. Experimental work is being encouraged by emerging technologies that can fabricate the fine structures required. This chapter first discusses the various regimes in which a sample exhibits one-dimensional behaviour, then briefly reviews the results of other researchers. It also reports my investigations on the quantum conductivity corrections in the weakly localised regime. These results, obtained in a narrow channel heterostructure, constitute a major part of this dissertation. Both the quantum interference and electron interaction corrections are presented in their one-dimensional limits, and compared with theoretical predictions. Anomalous behaviour, which appeared in the magnetoresistance, is also discussed.

The quantum limit of a single one-dimensional (particle in a box) sub-band has never been achieved in experimental studies, but one-dimensional behaviour can be explored by other criteria. In Chapter 2, we discussed

the relative lengths  $L_\phi$ ,  $L_T$  and  $W$  and their effects on the dimensionality of the quantum conductivity corrections in the weakly localised regime. At finite temperature, the phase coherence length is the effective sample length; when this length  $L_\phi$  exceeds the device width  $W$ , the quantum interference correction becomes one-dimensional, but if  $L_\phi$  also exceeds the localisation length  $\xi$ , the 1D transport becomes strongly localised. Dean [74] generalised the fine wire argument of Thouless [29] to the present case by considering the resistance of a thin sheet, instead of a wire resistance. Assuming a 2D density of states, the resistance of a thin sheet of length  $L$  and width  $W$  is given by

$$R = \frac{L}{W} \frac{1}{\sigma_B} = \frac{L}{W} \frac{2\pi\hbar}{ne^2 k_F l} \quad (4.1)$$

Thouless found that localisation effects become important when the wire resistance approaches  $\hbar/e^2$ . They reported the localisation length as simply the length of wire with this critical resistance. Equating Eq. 4.1 to  $\hbar/e^2$ ,  $\xi$  for a narrow sheet is obtained as:

$$\xi \sim \frac{W n k_F l}{2\pi} \quad (4.2)$$

In the strongly localised transport regime, an electron can diffuse through the localisation length before being inelastically scattered to a new state and propagating further through the device. As the confinement time within the localisation length is characterised by  $\tau_\phi$ , the effective diffusion constant

can be much smaller than the Boltzmann value. Thouless [75] proposed an expression for the diffusion constant that is valid in both weakly and strongly localised 1D regimes:

$$D = D_0 \left[ 1 - \left( \frac{4D_0\tau_\phi}{\xi^2} \right)^{\frac{1}{2}} \tanh \left( \frac{\xi^2}{4D_0\tau_\phi} \right)^{\frac{1}{2}} \right] \quad (4.3)$$

where  $D_0$  is the Boltzmann value of  $D$ . When  $\tau_\phi$  is short ( $L_\phi \ll \xi$ ), Eq. 4.3 gives the weak localisation correction proportional to  $L_\phi$ , as found in Chapter 2. Conversely, when  $L_\phi \gg \xi$ , Eq. 4.3 reduces to

$$D \approx \frac{\xi^2}{12\tau_\phi} \quad (4.4)$$

As  $\tau_\phi$  depends on the temperature, the conductivity will vary as a power function of  $T$ . This behaviour, known as Thouless hopping, describes the hopping of an electron through distance  $\xi$  in a mean time interval  $\tau_\phi$ .

At very low temperatures the energy separation between the overlapping localised states exceeds  $k_B T$ , and exponentially activated hopping is expected. If there are no nearest-neighbour states within  $k_B T$  of  $E_F$ , variable-range (Mott) hopping occurs. In one-dimensional transport, the device width must be smaller than the most probable hopping distance. The conductivity is then given by Eq. 2.64.

The number of states in a 2D sample of area  $A = \xi W$  with energy within  $k_B T$  of  $E_F$  is given by

$$N = \frac{nm^*k_B T A}{\pi \hbar^2} \quad (4.5)$$

Setting  $N = 1$ , we obtain the temperature below which variable-range hopping occurs:

$$k_B T = \frac{\pi \hbar^2}{nm^* \xi W} \quad (4.6)$$

This temperature is experimentally accessible for very small  $W$  and  $\xi$  (or  $k_F l$ ).

At much lower temperatures, conduction through short sample lengths is dominated by resonant tunnelling through localised sites. The conductance as a function of Fermi energy should largely depend on the sample structure, because at special Fermi energies, resonant states are generated near the centre of sample. Consequently, the electrons can tunnel through the sample, with a large transmission coefficient. The various regimes of one dimensional transport are summarised in Figure 4.1.

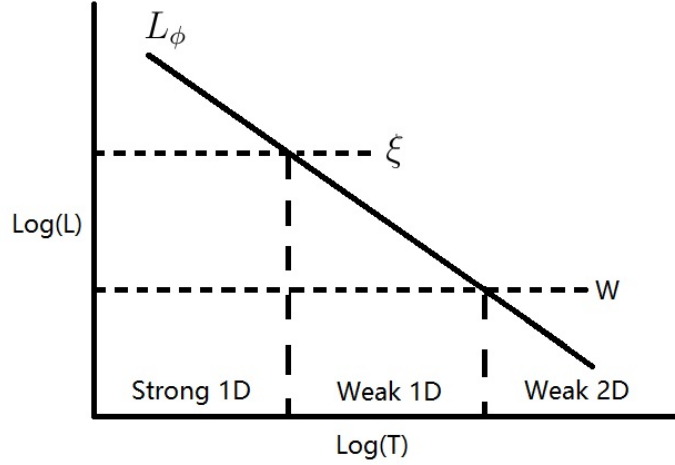


Figure 4.1: Schematic of the various localisation regimes in a narrow two-dimensional system. As the temperature decreases, the regime changes when  $L_\phi$  becomes sufficiently larger than  $W$ , and again when  $L_\phi$  becomes sufficiently larger than  $\xi$  (the localisation length).

## 4.1 Quantum transport and dimensionality transitions in GaAs/AlGaAs heterostructures

### 4.1.1 Devices used in this work and experimental setup

The devices were fabricated on a *GaAs/AlGaAs* heterojunction wafer encoded *W923*. The wafer was grown by MBE in the Cavendish Laboratory, University of Cambridge by Dr. Ian Farrer. The devices were also fabricated in the Cavendish Laboratory by Dr. Graham Creeth. The dimensions of the Hall-bar were  $1200\mu\text{m} \times 80\mu\text{m}$ . The length of the split-gates was varied as  $2\mu\text{m}$ ,  $4\mu\text{m}$  and  $8\mu\text{m}$ ; the width was constant at  $1\mu\text{m}$ . The aim was to observe the length effect of the behaviour. The lengths are multiples of the phase

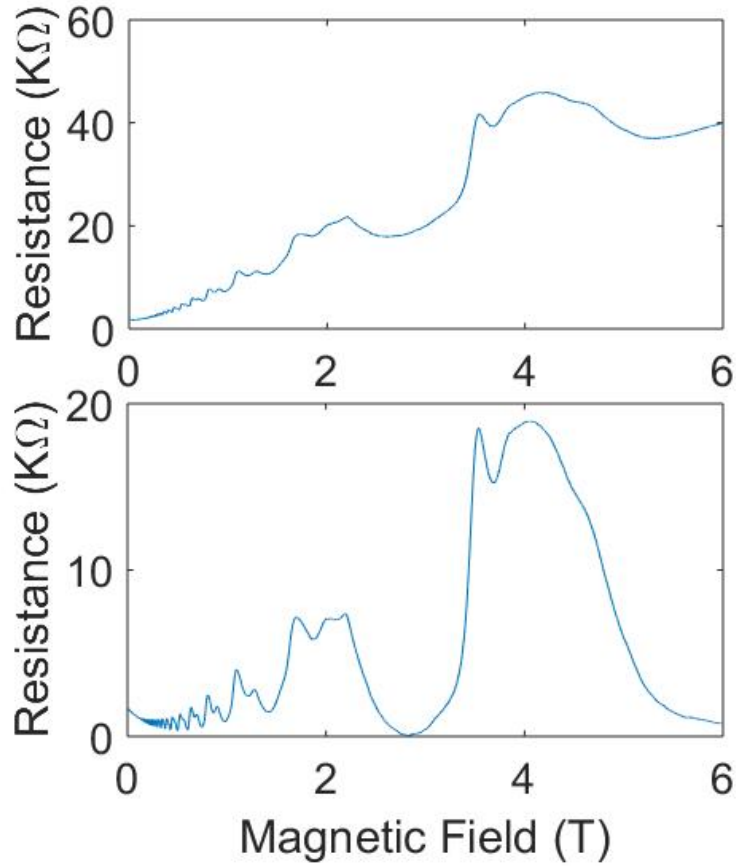


Figure 4.2: Shubnikov-de Haas oscillations of the  $GaAs/AlGaAs$  heterojunction. Upper panel shows the original data. Lower panel shows the oscillations after removing the longitudinal background signal.

coherence length (predicted as much greater than  $1\mu m$  at the base temperature of the dilution system). To characterise the signal, we fabricated four pairs of ohmic contacts; unfortunately, only one pair (in x-x direction) was functional. Although this problem did not affect the magnetoresistance data acquisition, it prevented us from measuring the quantum Hall effect in the direction perpendicular to the current. A constant  $77Hz$  AC current of  $10nA$  was applied between ohmic contacts.

The Shubnikov-de Haas oscillations are plotted in Figure 4.2. Clearly,

the oscillations are not ideal; in fact, rather than oscillatory behaviour, the heterojunction exhibits a kind of plateau behaviour with no zero minima. We infer that the oscillations are deteriorated by the longitudinal proportion of the background signal in the highly disordered system. Because the ohmic contacts measure over a rectangular area, the expected result is a combination of SdH oscillations and QHE plateaus. The result of removing the QHE background signal is presented in the bottom panel of in Figure 4.2. The good oscillation results confirm our speculation. From this plot, the 2D carrier concentration was determined as  $1.26 \pm 0.1 \times 10^{11} \text{cm}^{-2}$ . The effective mass of 0.12 was calculated from the temperature-dependent SdH oscillations using Eq. 1.18. The result (0.12) is much larger than the theoretical effective mass of *GaAs* (0.067), which may indicate the existence of strong electron-electron interactions.

We also attempted to reproduce the magneto-depopulation of one dimensional subbands reported by Berggren et al. [72]. To this end, we varied the split-gate voltage and observed the changes in the SdH oscillations. However, we detected no evidences of magneto-depopulation of the Landau levels, so we do not elaborate on the this result.

### 4.1.2 Two-dimensional quantum transport

The temperature dependence of the phase coherence length was measured in a dilution cryostat with  $11 \text{mK}$  base temperature. The superconducting magnetic field was swept from  $-0.1 \text{T}$  to  $0.1 \text{T}$ . As the applied voltage was varied between the individual pairs of split-gates, changes in the electric confinement at both arms of the split-gate were expected, and in the channel

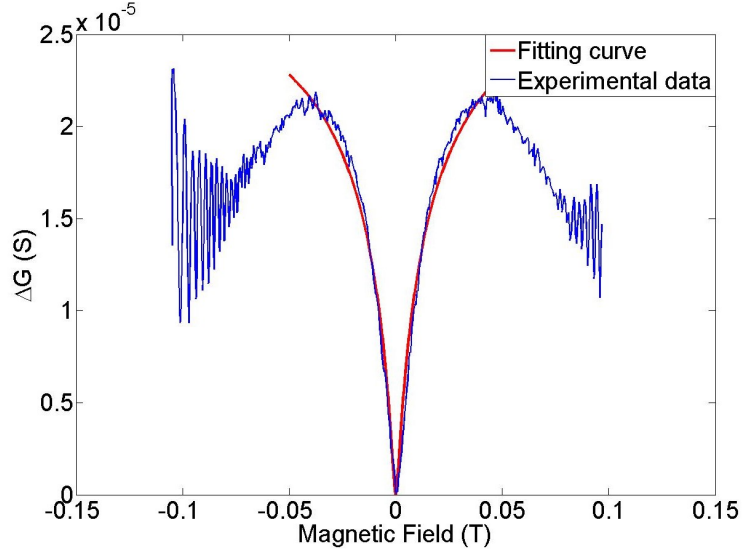


Figure 4.3: Example of experimental data fitting with a digamma function

width. To extract the value of  $L_\phi$ , the experimental magnetoconductance data were fitted to the theoretical model using Matlab (2015b), treating  $\tau$  and  $\tau_\phi$  as variables. All of the experimental data must be pre-processed before analysis. First, the background signal must be removed from the transverse resistances measured at four terminals. According to the Schrödinger equation, this background signal is parabolic. During a single run at base temperature, the system thermometer recorded significant temperature rises ( $\sim 35mK$ ) during the magnetic field sweeping. We surmised that the base temperature of the system was lower than the electron temperature; consequently, the electrons heated by the magnetic field sweeping contributed to the transport. Thus, the base temperature of experiment was corrected to  $35mK$ .

In the 2D case, the data were fitted to the digamma function as shown in Eq. 2.32. In this equation, only two parameters (scattering time and phase

coherence time) are unknown. Hence, these two parameters are considered as variables with values within a reasonable range. Data are normally fitted by least-mean squares, but this approach was discarded mid-analysis because the complexity of the programming exceeded our programming knowledge. Our replacement approach (fixing one variable per run and leaving one free parameter) greatly simplified the analysis, but reduced its accuracy. First we fixed the phase coherence length to different values ( $500nm$ ,  $1\mu m$  and  $1.5\mu m$ ), and ran a self-coded program at each of these values, treating  $\tau$  as the only variable. The fitted scattering time was quite insensitive to the phase coherence length; all coherence lengths yielded  $1.1 \pm 0.1 \times 10^{-12}s$ . The parameter-independent scattering time suggests the feasibility of our fitting method. We also note the existence of another unknown parameter: the effective width-to-length ratio. After transforming the ratio to a relation between mobility and scattering time, we determined this ratio in terms of the scattering time alone. The curve fitting yielded a ratio of  $\sim 0.9$ , much smaller than the proportional dimensions of the Hall bar, indicating a high level of impurities. This simplified method is prone to error not only because the fitting was judged by eye, but also because the adjacent variables were widely spaced. Next, to find the best fitted phase coherent length, we fixed the scattering time inside the digamma function. Figure 4.3 shows the best fitting result at base temperature ( $35mK$ ) with zero gate voltage. Using Eq.2.25, the phase coherence length was calculated as  $540 \pm 10nm$ , much smaller than the coherence length determined at the design stage of the experiments ( $\sim 1\mu m$ ). As phonon scattering is subdued at the selected base temperature, the system is dominated by electron-electron scattering. The

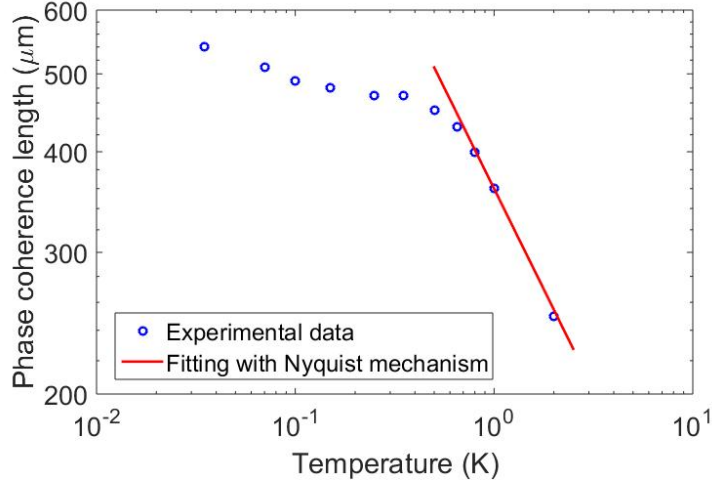


Figure 4.4: Log-log plot of phase coherence length versus temperature. At high temperatures, the data are well fitted to the solid line  $T^{-1/2}$  at high temperature. The deviation at low temperatures may result from magnetic impurities.

reason for the unexpected low phase coherence length is discussed later in the text. The magnetic field for the fitting equation was varied from  $-0.05T$  to  $0.05T$ . Within this range, the condition  $D\tau_B > W^2$  was satisfied.

The experimental data in 2D (at 0 split-gate voltage) were plotted as function of temperature, and the phase coherence time was extracted from the fitting results. The phase coherence length was then calculated by Eq.2.25. The temperature dependence of the phase coherence length is presented in Figure 4.4. Both axes of this figure are logarithmically transformed. Clearly, the phase coherence lengths are smaller than the channel, and exhibit two-dimensional behaviour (i.e. scaling as  $L_\phi \sim T^{-1/2}$  at high T). The limiting results indicate impurities in the device, and  $L_\phi$  is determined as  $0.36(\pm 0.01) \times 10^{-6}(T/K)^{-1/2}m$ . The 2D version of the Nyquist mechanism was presented in Chapter 2. From Eq.2.68,  $L_N$  is given by

$$L_N = \sqrt{\frac{D\hbar k_F l}{k_B T \ln(k_F l)}} \quad (4.7)$$

where  $k_F l > 1$ .

Inserting the parameters into Eq.4.7,  $L_N$  was determined as  $0.373 \times 10^{-6}(T/K)^{-1/2}m$ . The 2D Nyquist mechanism requires that  $k_B T \tau_\phi \gg \hbar$ . The experimental data are consistent with the Nyquist prediction, despite the limited data range.

### 4.1.3 Width estimates

When analysing and comparing data from various quantum point contacts (QPCs), one of the important quantities is the degree of confinement at the QPC in the direction perpendicular to the current flow. The effective width of the electron gas in the QPC cannot be measured directly.

Furthermore, the shape of the confining potential is not known, but is most easily modelled by the square well and the harmonic oscillator. In both models, we can estimate the effective width of the QPC, and thereby characterise the confinement. We estimate the effective width by the Sharvin formula, which is based on the confining potential and on theoretical assumptions about transport. In this estimation, we ignore the finite length of the QPC, and treat the potential associated with the gates as one-dimensional.

In the Landauer formalism with zero magnetic field, the current in the sample is equally distributed among the 1D subbands which are the transversal (propagating) modes of the confining potential in the constriction. Consequently, the conductance is proportional to the number of propagating modes

at the Fermi level,

$$G = \frac{2e^2}{h} N_{QPC} \quad (4.8)$$

Assuming a hard-wall confining potential, the width of each 1D subband is half the Fermi wavelength  $\lambda_F/2$ . Therefore, the number of conducting 1D subbands in a QPC of width  $W$  is given by

$$N_{QPC} = \mathbb{Z} \left( \frac{W}{\lambda_F/2} \right) \quad (4.9)$$

Here,  $\mathbb{Z}(x)$  means the integer value of  $\frac{W}{\lambda_F/2}$ . In the ballistic electron transport regime at zero magnetic field, the resistance becomes

$$R(B = 0) = \frac{h}{2e^2} \frac{\lambda_F}{2W} \quad (4.10)$$

Eq.4.10 is the 2D analogue of the resistance through a 3D QPC. The Fermi wavelength is estimated from the 2D electron density in the QPC, as explained below. By measuring the resistance at zero magnetic field we can then estimate the width of the QPC.

This method estimates the width from the zero-field resistance of the sample. Alternatively, we can measure the magnetic field dependence of the resistance. The 1D transport subbands discussed above can be depleted by

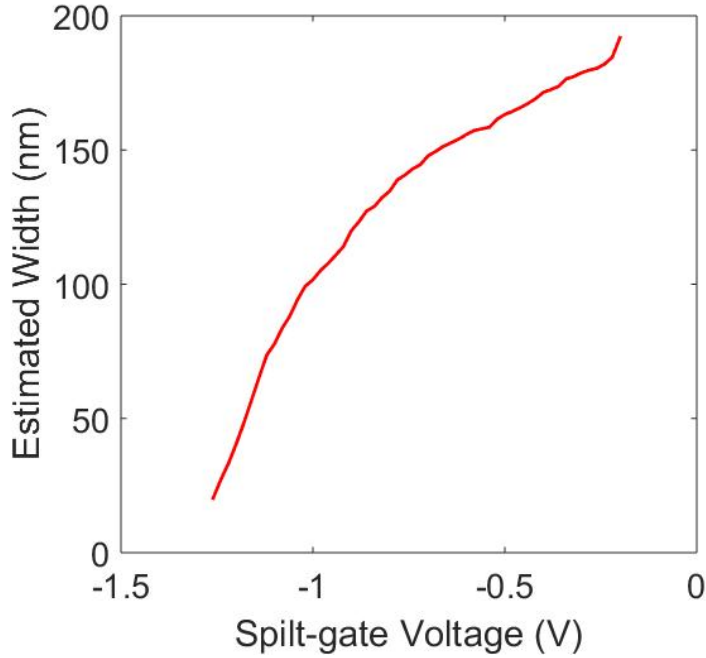


Figure 4.5: Estimated width versus split-gate voltage

reducing the width of the QPC, modifying the Fermi energy, or applying a magnetic field perpendicular to the plane of the sample. In the presence of a magnetic field, the corresponding subbands are called magneto-electric subbands. They are depopulated by increasing the magnetic field.

Figure 4.5 plots the channel widths estimated by the Sharvin formula at different split-gate voltages. These channel widths were used in the curve fittings described later in this chapter.

#### 4.1.4 One-dimensional quantum transport

The 1D magnetoconductance can be computed by Eq. 2.32 in Chapter 2. The scattering time indirectly enters this equation through the diffusion coefficient  $D$ . Here we note that the form of the diffusion coefficient differs between one

and two dimensions. Specifically, the diffusion coefficient depends on the dimensionality as:

$$D = \frac{1}{d} v_F^2 \tau \quad (4.11)$$

where  $d$  is the dimensionality,  $v_F$  is the Fermi velocity and  $\tau$  is the scattering time.

Once the channel widths have been estimated, we can compute the phase coherence time. In the following content, the results will be presented in separate sections, providing a comprehensive description of the whole device. Note, that the prerequisite in our analysis is the constant split-gate voltage, not the width. As the width variability is small, we can assume that a device with a constant split-gate voltage also has the same width.

### (1) 2D to 1D transition

This transition occurs when the split-gate voltage increases from zero to the definition voltage. In this device, the definition voltage is slightly smaller than  $-0.24V$ . The behaviour of the magnetoresistance corrections also converts from 2D to 1D in this voltage range. The data are fitted to both 2D and 1D formulas, and the most compatible fitting is assumed as the correct dimensionality of the system.

Figure 4.6 plots the magnetoconductances as a function of split-gate voltage in the 2D-to-1D transition. The 2D fitting results from  $0V$  to  $-0.18V$  are plotted in Figure 4.7. The behaviour were better fitted to the 2D than the 1D formula. The fitting part of the curves become narrows as the volt-

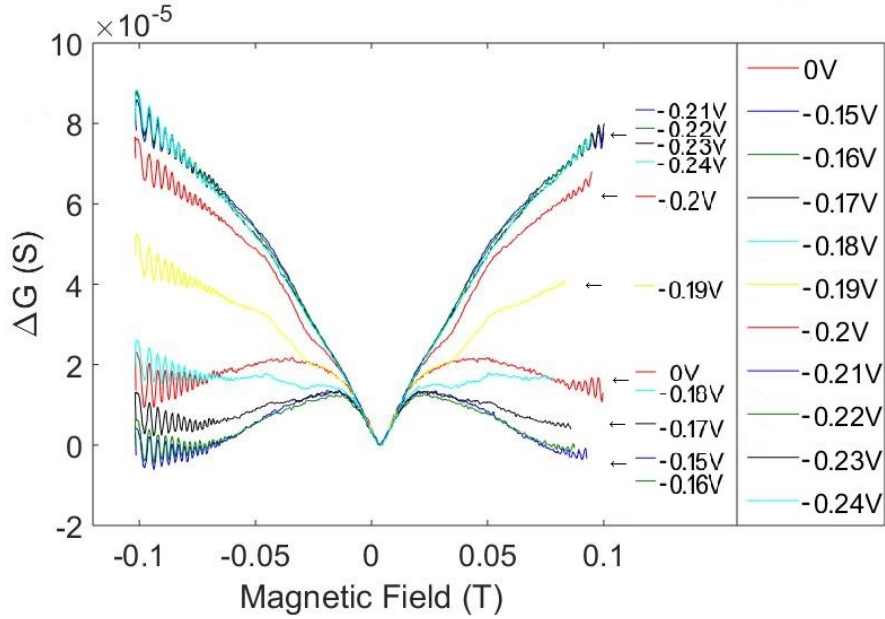


Figure 4.6: Magneto-conductance behaviour at split-gate voltages from  $0V$  to  $-0.24V$ . The upper limit of this range is the definition voltage of the split-gate device. Inside this range, the magneto-conductance transits from 2D to 1D.

age increases, reflecting the dominant magnetic effect as the phase coherence length surpasses the magnetic length. The 2D phase coherence length decreases with increasing split-gate voltage, reducing the magnetic field that maximises the magnetic length.

Transport theory predicts that the 2D-to-1D transition occurs when the phase coherence length exceeds the channel length. In the previous subsections, we estimated the channel width of the QPC. The transition was expected by the applied split-gate voltage, but no 1D behaviour appeared in the experimental data at the beginning of the voltage application. We infer that the 1D construction was not finally formed, the electrons beneath the QPC was not depleted completely until exceeds the definition point (voltage).

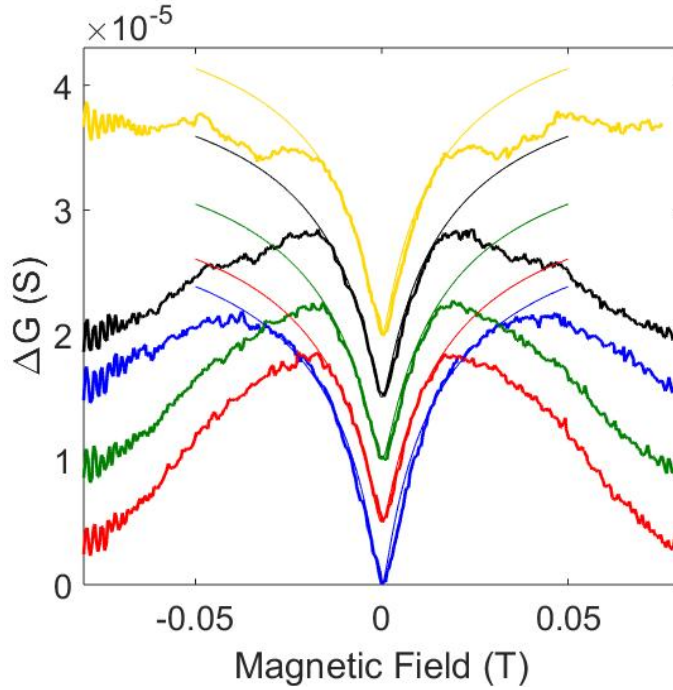


Figure 4.7: Magneto-conductance fitting by a 2D digamma equation at split-gate voltages ranging from  $0V$  (lowest plot) to  $-0.18V$  (highest plot). The curves are offset for visibility. The phase coherence lengths corresponding to each split-gate voltages are  $540 \pm 10nm$ ,  $480 \pm 10nm$ ,  $460 \pm 10nm$ ,  $480 \pm 10nm$  and  $510 \pm 10nm$ .

In figure 4.8, the data are fitted to the 1D equation at split-gate voltages from  $-0.18V$  to  $-0.24V$ . The fitting curves yield longer phase coherence length than 2D fitting. This result is expected, because there are fewer disorder events in 1D channels than 2D channels.

The fitting results reveal some shoulder behaviour. This occurs at the magnetic field when the magnetic length becomes shorter than the phase coherence length. Thornton et al [76] reported a similar behaviour in *GaAs* quantum wires, which they attributed to the analogous phenomenon of scattering. In their case, the mean free path was much longer than the wire width; thus, their observed shoulders reflected the size effect of the electrons

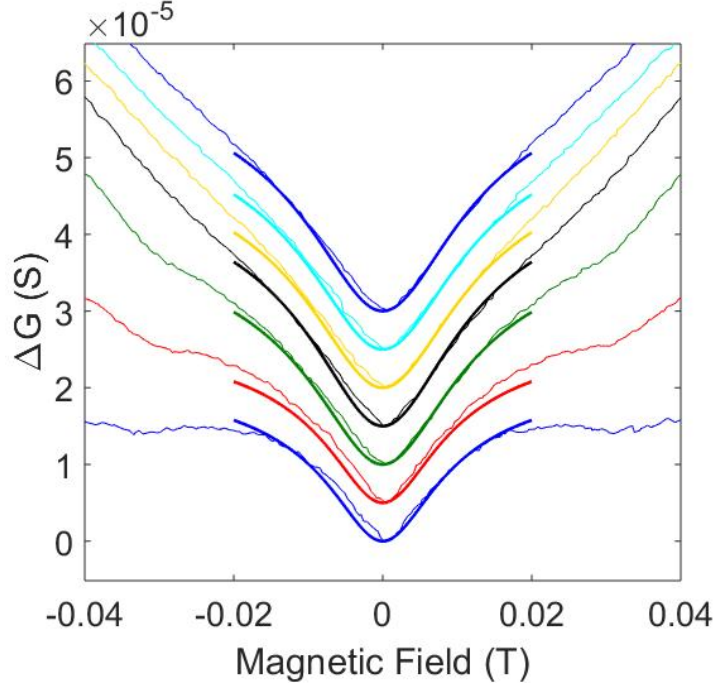


Figure 4.8: Magneto-conductance fitted to the 1D equation at split-gate voltages ranging from  $-0.18V$  (lowest plot) to  $-0.24V$  (highest plot). The curves are offset for visibility. The phase coherence lengths corresponding to each split-gate voltage are  $760 \pm 10nm$ ,  $740 \pm 10nm$ ,  $690 \pm 10nm$ ,  $660 \pm 10nm$ ,  $670 \pm 10nm$ ,  $650 \pm 10nm$ ,  $650 \pm 10nm$  and  $660 \pm 10nm$ .

scattering from the wire boundary. In our device, the shoulder behaviour appears in the 2D-to-1D transition region, where the mean free path is much smaller than the channel width. Therefore, the shoulder cannot result from boundary scattering. Figure 4.9 shows the colour-scale results of magneto resistance when a small DC current bias was applied to the device in the AC current direction (transverse direction). The x- and y-axes represent the magnetic field and split-gate voltage, respectively. Blue region indicate the zero differential regions. In Figure 4.9, the shoulder behaviours slightly weaken as the DC bias increases. The DC bias could not only broaden the channel width, but could also strongly decrease the phase coherence length.

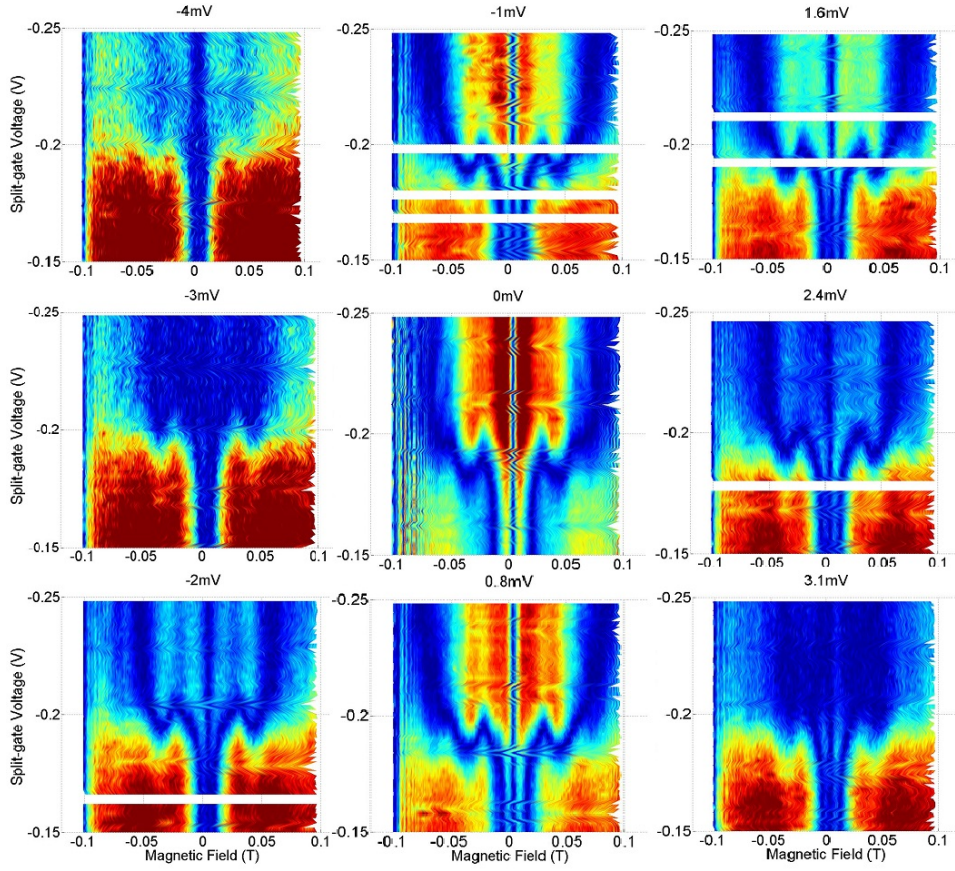


Figure 4.9: Colour-scale plots of magnetoresistance in our device at DC bias voltages ranging from  $-4\text{mV}$  (top-left) to  $3.1\text{mV}$  (bottom-right).

In other word, it can shift the system towards 2D. However, we observed no position change at the magnetic fields of these shoulders, confirming the absence of boundary scattering.

Bockhorn et al. [77–81] observed a similar shoulder behaviour in magnetoresistance measurements. They proposed several possible origins, and experimentally investigated the plausibility of each origin. They attribute the formation of the shoulder behaviour to interactions between smooth disorder and macroscopic defects in the material itself. The feasibility of their model to our devices still needs further investigation.

During fitting work, we detected variability in our channel length. Initially, we fixed the channel length at  $2\mu m$ , but most of the fittings were imperfect at this length. Thus, we allowed the length to vary, and obtained the best fitting result at  $1.4\mu m$ . Masden and Giordano [82] measured and discussed the length dependence of the localisation effect in detail. Choi et al. [83] systematically calculated the effective length scale. Further discussion will be presented later in this chapter.

## (2) Quasi 1D regime

The channel enters the quasi-1D transport regime when the split-gate voltage exceeds  $-0.25V$ . At this regime, the channel width is shorter than the phase coherence length.

### a. A split-gate voltage of $-0.3V$ , the estimated width is $\sim 0.18\mu m$

Figure 4.10a shows the temperature dependence of the phase coherence length at this split-gate voltage. At higher temperatures, the data are well fitted to  $T^{-1/2}$ , indicating 2D behaviour. In 1D transport, the phase coherence should increase at the 1D Nyquist rate  $T^{-1/3}$ . We consider that electron-electron scattering becomes 1D limited when  $L_T > W$ . If  $L_T < W$ , the 2D temperature dependence of the phase coherence length is recovered. At this split-gate voltage, the thermal de-phasing length  $L_T$  cannot exceed the width until the temperature approaches  $1K$ . Above this temperature, we expect the 2D limit of electron-electron scattering to vary as  $T^{-1/2}$ . From the good  $T^{-1/2}$  fitting above  $T = 1K$ ,  $L_\phi$  was determined as  $0.55 \times 10^{-6}(T/K)^{-1/2}m$ . At temperatures below  $1K$ , the curve is much better fitted to  $T^{-1/3}$ . Because  $L_T$  is lengthening relative to  $W$ , this result confirms our prediction.

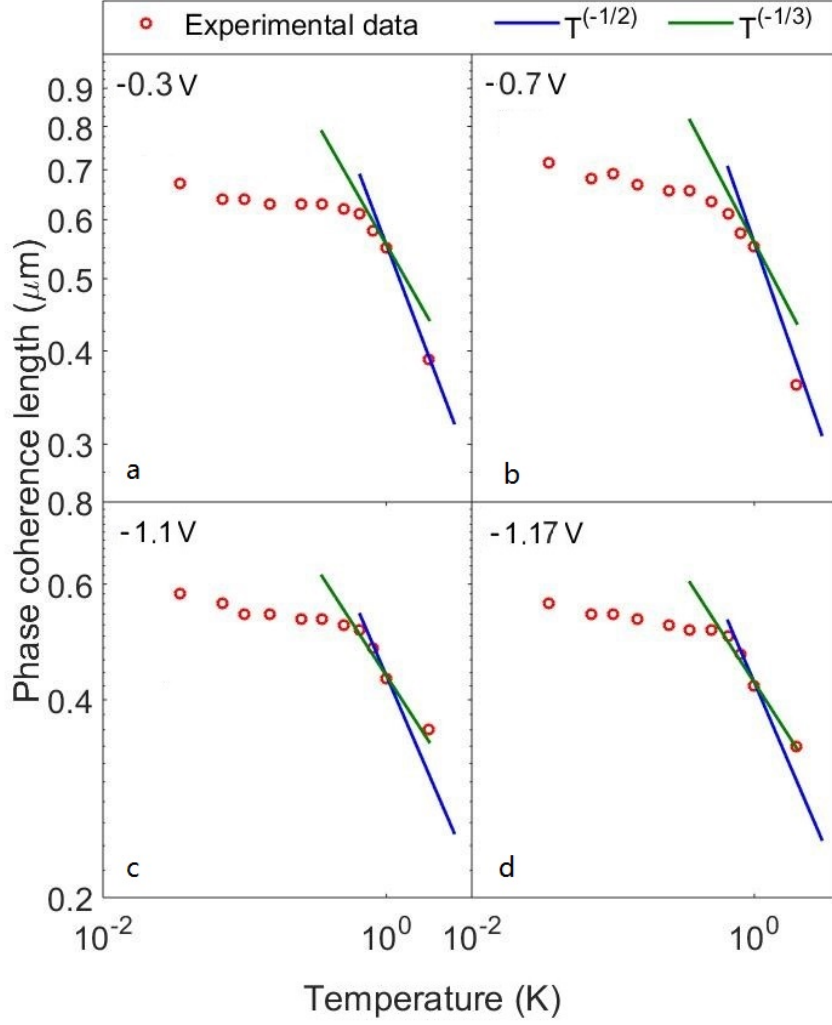


Figure 4.10: Log-log plots of phase coherence length versus temperatures at different channel widths. In panel (a) and (b),  $V_{SG}$  (and estimated width) are  $-0.3V$  ( $0.18\mu m$ ) and  $-0.7V$  ( $0.15\mu m$ ), respectively. Both curves are well-fitter to  $T^{-1/2}$ , indicating 2D behaviour. In panel (c) and (d),  $V_{SG}$  (and estimated width) are  $-1.1V$  ( $0.08\mu m$ ) and  $-1.16V$  ( $0.05\mu m$ ), respectively. Both curves are well-fitter to  $T^{-1/3}$ , indicating 1D behaviour.

**b. When split-gate voltage increases to  $-0.7V$ , the estimated width is  $\sim 0.15\mu m$**

The phase coherence length at this split-gate voltage is plotted as a function of temperature in Figure 4.10b. The behaviour mimics that at  $-0.3V$ . The width remains more-or-less constant, and 2D and 1D behaviour appear across the temperature range.

**c. At split-gate voltage of  $-1.1V$ , the estimated width is  $\sim 0.08\mu m$**

At this split-gate voltage, the behaviour of the system changes. First, the estimated width continuously decreases. The temperature calculated from the condition  $L_T > W$  increases to approximately  $5K$ , implying that the device behaves in the 1D limit throughout the experimental temperature range. Indeed, the phase coherence length at higher temperatures is well-fitted to the  $T^{-1/3}$  (Figure 4.10c). The deviation below  $650mK$  indicates that the Nyquist mechanism fails in parts of the whole temperature range. In this case, we must consider the pure metal limit (as discussed later). The effective length evaluated from the best fitting at this split-gate voltage increases to  $\sim 2\mu m$ .

**d. Finally, when the split-gate voltage increases to  $-1.16V$ , the estimated width is  $\sim 0.05\mu m$**

The higher temperature data exhibit  $T^{-1/3}$  behaviour. The effective length becomes  $\sim 3\mu m$ , which exceeds the split-gate length. The effective electric confinement length, which is used in the magnetoresistance fitting, increases with the increased electric field, and (in this case) appears to exceed the lithography confinement a lot. However, we found no literature to verify

this finding. The Nyquist rate in 1D is given by

$$L_N = \left( \frac{GDL\hbar^2}{e^2k_B T} \right)^{\frac{1}{3}} \quad (4.12)$$

From this expression, the phase coherence length is calculated as  $0.53 \times 10^{-6}(T/K)^{-1/3}m$ . This result is of the correct order of magnitude, implying very good agreement with fitting results.

### (3) Pure 1D regime

As the split-gate voltage increases, the channel resistance rises to  $h/2e^2$ . At this time, only one energy level is occupied. The channel becomes shorter than the mean free path, and the transport enters the quasi-ballistic regime or pure metal regime, where boundary scattering plays an essential role.

In our device, the split-gate voltage is maintained at  $-1.24V$ , and the resistance exceeds  $14K\Omega$ . The channel is nearly pinched off, and the estimated width remains at  $\sim 25nm$ . Figure 4.11 shows the fitting result at this split-gate voltage. The phase coherence length exhibits well-behaved  $T^{-1/3}$  dependence at higher temperature ( $> 650mK$ ), but deviates from this law at lower temperature. This behaviour is discussed in detail in the following section. The shoulder behaviour does not appear at this high split-gate voltage, confirming the absence of boundary scattering.

The phase coherence length always deviates from 1D or 2D behaviour at low temperature, and appears to saturate below some temperature. Such low-temperature saturation has been reported in many materials [84–88], so is unlikely to arise from thermal contact. Bäuerle et al. [89] and Saminadayar

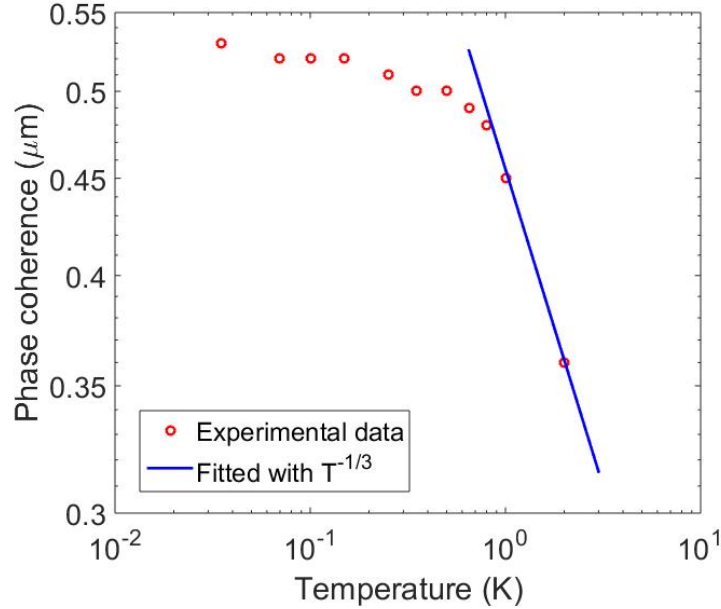


Figure 4.11: Log-log plot of coherence length versus temperatures at  $V_{SG} = -1.24V$ . The higher temperature data are well fitted to the  $T^{-1/3}$  law.

et al. [90] suggested that saturation manifests from spin-flip scattering by magnetic impurities. They provided a theoretical explanation based on the Kondo effect, which is beyond the scope of our present study.

The phase coherence lengths extracted from the fitting formulae are always shorter in the 2D case than in the 1D case. Similarly, the Nyquist rate calculations predict that the phase coherence lengths are longer in 1D than in 2D down to  $\sim 120mK$ . Because the temperature dependence differs between two regimes, a low-temperature crossover must exist (in our device, the crossover temperature is  $\sim 120mK$ ). However, as the temperature dependence disappears at low temperature, we cannot properly compare the phase coherence length between 1D and 2D regimes. We can only confirm that the phase coherence length adheres to the Nyquist rate at temperatures

above  $650mK$ .

## 4.2 One-dimensional quantum interference

Above, we mentioned that the temperature dependence of the phase coherence length deviates from the established rules at lower temperatures. The failure of Nyquist mechanism may reflect the crossover of the system to the metal limit.

At very low temperatures, the quasi-particle lifetime consists of two terms, the pure metal limit  $\tau_{ee}^0$  with large momentum transfer collisions, and the disordered systems limit  $\tau_{ee}^1$  with small momentum transfer. The Landau-Baber scattering (Fermi liquid theory) of the electron-electron collision time  $\tau_{ee}^0$  has been well established. The theory describes the scattering governed by large momentum or energy transfers, and is independent of electron interactions. Conversely, the Nyquist mechanism describes the random scattering of electrons with very small energy change. Matthiessen's rule, which combines the Landau-Baber and Nyquist terms at very low temperature, gives the total phase coherence scattering time as

$$\tau^{-1} = AT^2 + BT^{2/3} \quad (4.13)$$

where  $A$  and  $B$  are the Landau-Baber and Nyquist parameters, respectively. The condition of the Nyquist mechanism,  $k_B T \tau_\phi \gg \hbar$ , admits more than one possible phase breaking mechanism. Pooke [91] suggested a weaker temperature dependence  $L_\phi (T^{-1/4})$  with large energy transfer rather than

$T^{-1/3}$  dependence.

Thus, we identify three possible mechanisms for the temperature dependence of phase coherence length  $L_\phi$  in one dimension:

(a) At higher temperatures, electron-electron scattering becomes 2D, and the temperature dependence is  $T^{-1/2}$ ;

(b) At lower temperatures where  $k_B T \tau_\phi > \hbar$ , electron-electron scattering becomes 1D, and  $L_\phi$  consists of both  $L_N$  ( $T^{-1/3}$ ) and the Landau-Baber term ( $T^{-1}$ );

(c) At lower temperatures where  $k_B T \tau_\phi < \hbar$ , electron-electron scattering is 1D, and  $L_\phi$  consists of both the  $T^{-1/4}$  term and the Landau-Baber term ( $T^{-1}$ ).

Figure 4.12 shows the fitting result to  $AT^2 + BT^{2/3}$  at  $-1.24V$ . From this fitting, the parameters  $A$  and  $B$  were determined as  $0.9(\pm 0.1) \times 10^{12} m^{-2}$  and  $0.32(\pm 0.1) \times 10^{12} m^{-2}$ , respectively. We noted the diffusion constant we got here is larger than the previous estimation. Thus, the Landau-Baber and 1D Nyquist terms become

$$\text{Landau - Baber : } A^{-1/2} = 0.95(\pm 0.01) \times 10^{-6} m \quad (4.14)$$

$$\text{Nyquist : } B^{-1/2} = 0.56(\pm 0.01) \times 10^{-6} m \quad (4.15)$$

The factor  $B^{-1/2}$ , which defines the temperature pre-factor for  $L_N$ , agrees well with previously calculated values. The assumption of the Nyquist rate in the fitting procedure may seem rather artificial, and  $1/L\phi^2$  might be better described combining the  $T^{-1/2}$  and  $T^{-1}$  terms. In our case, we can rule out

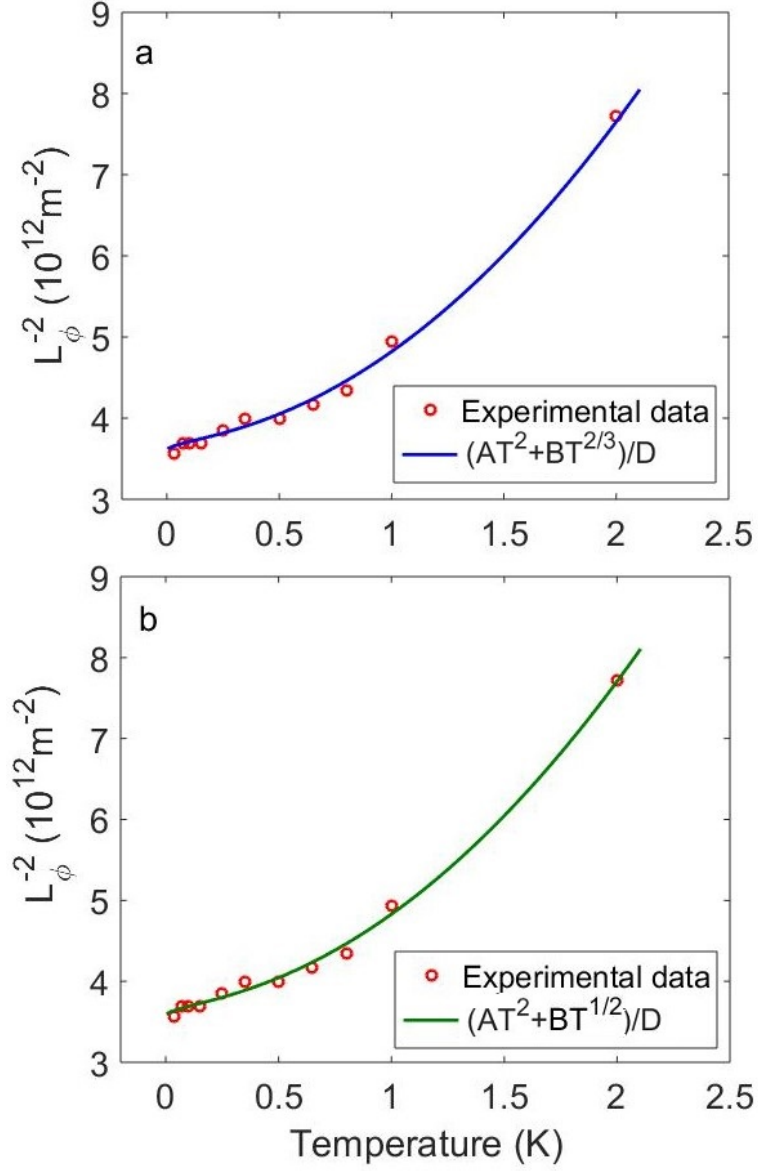


Figure 4.12:  $L_{\phi}^{-2}$  versus temperatures at  $V_{SG} = -1.24V$ . a.The best-fitting  $AT^2 + B^{2/3}$  curve yields  $A = (0.9 \pm 0.1) \times 10^{12} \text{m}^{-2}$ ,  $B = (0.32 \pm 0.1) \times 10^{12} \text{m}^{-2}$  and Diffusion constant  $D = 0.249$ ; b.The best-fitting with  $AT^2 + B^{1/2}$  curve yields  $A = (0.91 \pm 0.1) \times 10^{12} \text{m}^{-2}$  and  $B = (0.35 \pm 0.1) \times 10^{12} \text{m}^{-2}$ .

the Nyquist mechanism, because  $k_B T \tau_\phi < \hbar$  at lower temperatures. We also tried a data fitting to  $AT^2 + BT^{1/2}$ , which yielded

$$L_\phi^{-2} = 0.91(\pm 0.1) \times 10^{12} m^{-2} (T/K)^2 + 0.35(\pm 0.1) \times 10^{12} m^{-2} (T/K)^{\frac{1}{2}} \quad (4.16)$$

The correctness of this  $T^{-1/4}$  dependence, and the applicability of the Nyquist rate when  $k_B T \tau_\phi < \hbar$  cannot be proven. However, the two parameters in each regime are not significantly different, implying that the 1D temperature dependence of the phase coherence length  $L_\phi$  in our device is probably governed by the 1D Nyquist mechanism with a contribution from the Landau-Baber term in the pure metal limit, although the transport occurs in the region of  $k_B T \tau_\phi < \hbar$ .

### 4.3 Weak anti-localisation

The spin-orbit effect on magnetoconductance was presented in Section 2.6. All of the spin-orbit interactions manifested as weak anti-localisation (WAL). In our measurements, WAL features also appeared at higher temperature ( $2K$ ).

Figure 4.13 plots the magnetoresistance at  $2K$  and split-gate voltages of  $0V$  (lower panel) and  $-0.7V$  (upper panel). The upper plot exhibits a small WAL dip at zero magnetic field, but it still cannot confirm the existence of spin-orbit interaction. This WAL feature is absent in the 2D transport regime at zero split-gate voltage. This can happen where the spin-orbit coherence time is longer than the 2D phase coherence time, but shorter than

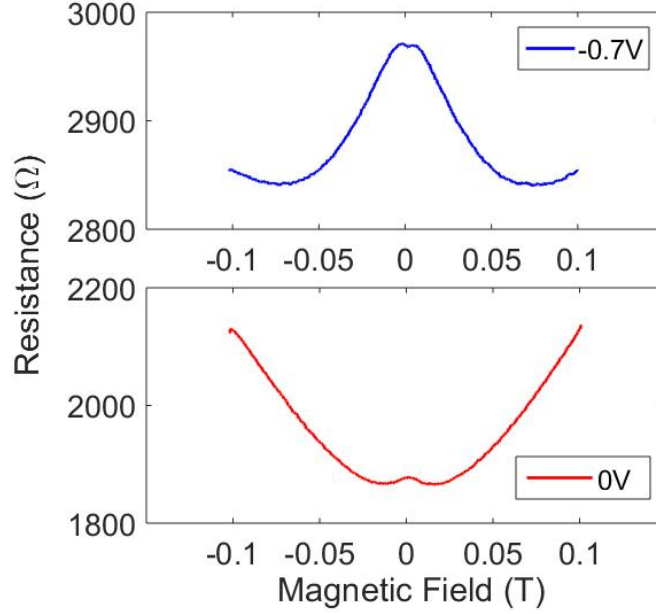


Figure 4.13: Magnetoresistance at  $2K$  and split-gate voltage of  $0V$  (lower) and  $-0.7V$  (upper). Weak anti-localisation (WAL) behaviour appears in the 1D region ( $-0.7V$ ).

the 1D phase coherence time.

In Section 2.6, we presented the conductance correction of spin-orbit interactions in 2D systems. In the 1D case, this correction becomes:

$$\delta G(B) = -\frac{e^2}{\pi\hbar L} \left[ 3 \left( \frac{1}{D\tau_\phi} + \frac{4}{3D\tau_{SO}} + \frac{1}{D\tau_B} \right)^{-\frac{1}{2}} - \left( \frac{1}{D\tau_\phi} + \frac{1}{D\tau_B} \right)^{-\frac{1}{2}} \right] \quad (4.17)$$

Thus, the magnetoconductance can be written as

$$\Delta G(B) = \frac{e^2}{\pi\hbar L} \left[ L_\phi - 3 \left( \frac{1}{D\tau_\phi} + \frac{4}{3D\tau_{SO}} + \frac{1}{D\tau_B} \right)^{-\frac{1}{2}} + \left( \frac{1}{D\tau_\phi} + \frac{1}{D\tau_B} \right)^{-\frac{1}{2}} \right] \quad (4.18)$$

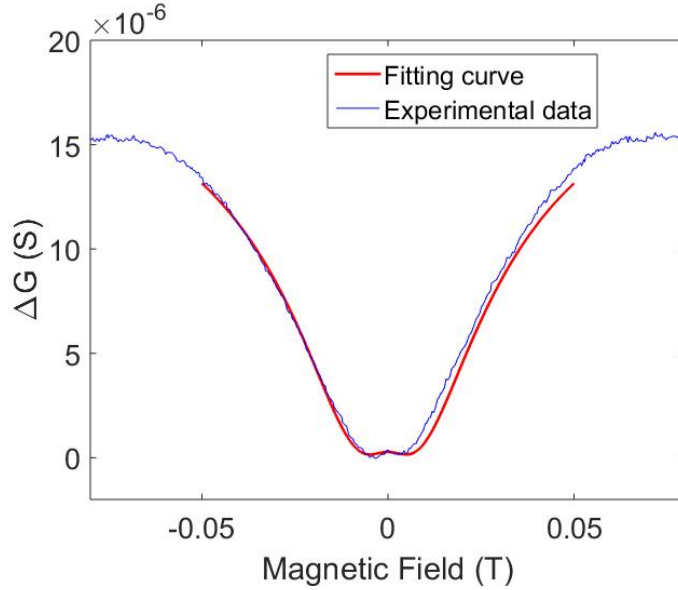


Figure 4.14: Fitting result of 1D magnetoresistance with the WAL effect at  $2K$  and  $V_{SG} = -0.7V$ . The fitting curve yields  $\tau_{SO} = 17 \pm 1ps$ .

Figure 4.14 shows the fitting result of the magnetoresistance at  $-0.7V$  split-gate voltage. The curve is very well fitted, at a spin-orbit coherence time of  $1.7 \pm 0.1 \times 10^{-11}s$ . Surprisingly, the phase coherence length obtained by this estimation was  $650 \pm 10nm$ , almost twice that of the previous obtained value, but consistent with the 1D Nyquist rate at this temperature  $680 \pm 10nm$ . Moreover, the thermal dephasing length is much shorter than this phase coherence length, indicating 1D transport at this temperature. As mentioned earlier, the system at  $-0.7V$  split-gate voltage exhibits  $T^{-1/2}$  rather than 1D behaviour. We conclude that a spin-orbit coherence term influences the simulations. Hikami [38] also mentioned the possibility of non-zero spin-orbit interactions, and recommended a pre factor  $\aleph$  less than one in front of the fitting equation (2.29). In all of our fittings, this parameter was treated as unity (i.e. spin-orbit interactions were neglected). The tem-

perature dependence of the spin-orbit coherence time has been frequently reported [92–94]. As the spin-orbit coherence increases faster than the phase coherence time, the WAL becomes vanishingly small at lower temperature. Therefore, we cannot explore in detail the spin-orbit coherence temperature dependence in our results.

We also understand that phase coherence time decreases with increasing split-gate voltage. Assuming constant spin-orbit coherence time, the WAL behaviour will disappear at sufficiently high split-gate voltages, when the phase coherence time falls below the spin-orbit coherence time. However, we observed a strengthening of the WAL feature with increasing split-gate voltage. This result requires that the spin-orbit coherence time is not constant, but a varying function of the carrier concentration. The fitting result acquired at higher split-gate voltage ( $-1.1V$ ) yielded a spin-coherence time of  $1.4 \pm 0.1 \times 10^{-11}s$ , consistent with our supposition.

From these discussions, we infer that the spin-orbit term is temperature dependent, and also electric-field tunable. Given also that the wafer grows along the [001] direction, it can be determined the spin-orbit term is confirmed as a Rashba term rather than a linear Dresselhaus term.

The discussion in Section 4.3, suggests that WAL might alternatively arise from spin-flip scattering. The system probably contains magnetic impurities, and spin-flip scattering exhibits temperature dependence similar to that of spin-orbit interactions. Therefore, our results cannot distinguish between spin-orbit interactions and spin-flip scattering individually.

## 4.4 Interaction effect in low-dimensional GaAs heterojunctions.

To study the electron interaction contribution to the temperature dependence of the device resistance, we quenched the quantum interference with small magnetic fields. Magnetic fields enhance the interactions only when  $g\mu_B B > k_B T$ . At the base temperature of  $35mK$ , the maximum magnetic field of quenching the interference was calculated as  $0.12T$ .

### 4.4.1 Interactions in two dimensions

The magnetoresistance data applied in the interaction correction has removed the weak localisation correction from the original data. The theoretically calculated localisation correction used to be subtracted to get the interaction effect correction only data. The form of the 2D interaction correction was discussed in Section 2.71. The correction can also be expressed as the change in conductance per unit length:

$$\Delta\sigma(T) = \frac{e^2}{4\pi^2\hbar} \left( 2 + \frac{3}{2}\lambda_\sigma^{j=1} \right) \ln \left( \frac{k_B T \tau}{\hbar} \right) \quad (4.19)$$

where

$$\lambda_\sigma^{j=1} = 4 \left[ 1 - \frac{2 \left( 1 + \frac{F}{2} \right) \ln \left( 1 + \frac{F}{2} \right)}{F} \right] \quad (4.20)$$

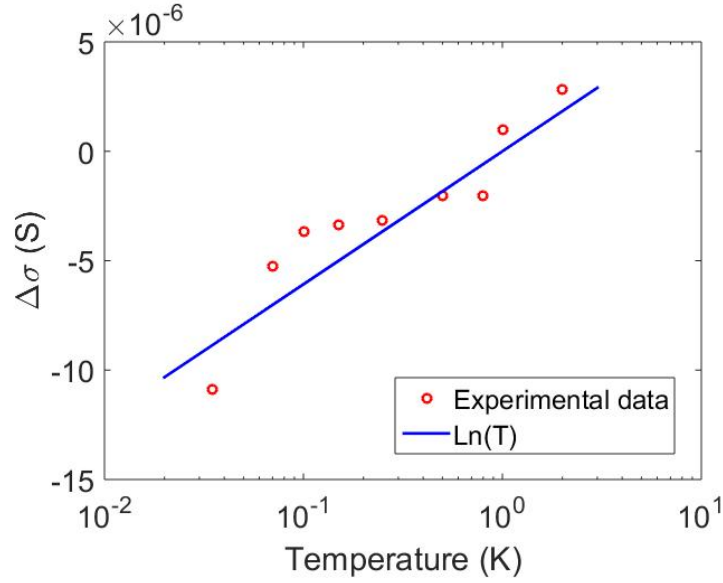


Figure 4.15: Conductivity versus temperature, with weak localisation quenched. The curve is well fitted to  $\sim \ln(T)$ .

In figure 4.15, the data are fitted to Eq. 4.19. The best fitted curve yields  $F = 1.24$ . Theoretically, this value should lie between 0 and 1. However, Altshuler and Aronov [45] included only the Coulomb repulsion of electrons in their  $F$  calculations, which may dramatically vary from the short-range interactions.

#### 4.4.2 Interactions in one dimension

The form of the 1D interaction correction was discussed in Section 2.71. The corrections can be written as:

$$\Delta\sigma(T) = -4.91 \times \frac{e^2}{4\pi^2\hbar} \left( 4 + \frac{3}{2}\lambda_{\sigma}^{j=1} \right) \left( \frac{k_B T}{\hbar D} \right)^{-\frac{1}{2}} \quad (4.21)$$

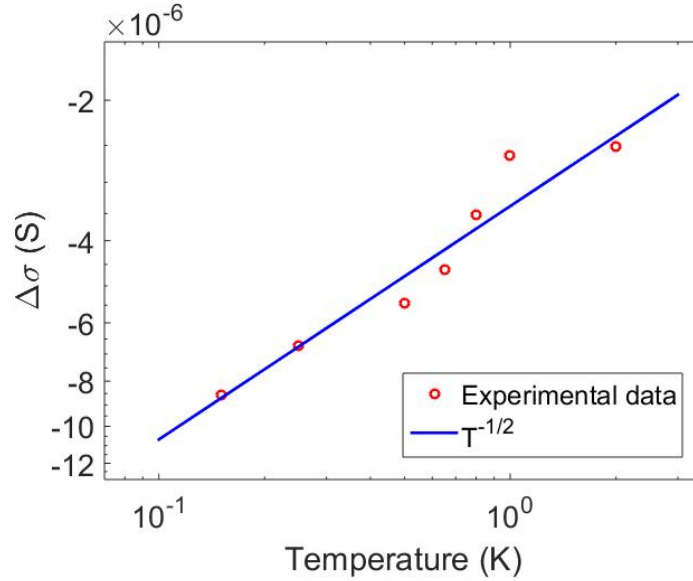


Figure 4.16: Conductance versus temperature at  $-0.7V$  split-gate voltage, with weak localisation quenched. The curve is well fitted to  $\sim T^{-1/2}$ .

where

$$\lambda_{\sigma}^{j=1} = -\frac{32}{F} \left( 1 + \frac{F}{4} - \left( 1 + \frac{F}{2} \right)^{\frac{1}{2}} \right) \quad (4.22)$$

The WL correction has been already removed from the original conductance. The 1D interaction correction for the device was investigated at split-gate voltages of  $-0.7V$  and  $-1.2V$ . The correction results are plotted as functions of temperature in Figure 4.16 and 4.17, respectively. At both voltages, the conductance correction exhibited  $\sim T^{-1/2}$  behaviour. The best-fit lines at  $-0.7V$  and  $-1.2V$  yielded Coulomb screening potentials  $F$  of 5.88 and 5.96, respectively. This higher potential at  $-1.2V$  reflects the weaker screening at this split-gate voltage. This occurs because increasing split-gate voltage, the carrier concentration decreases, thus weakening the interaction.

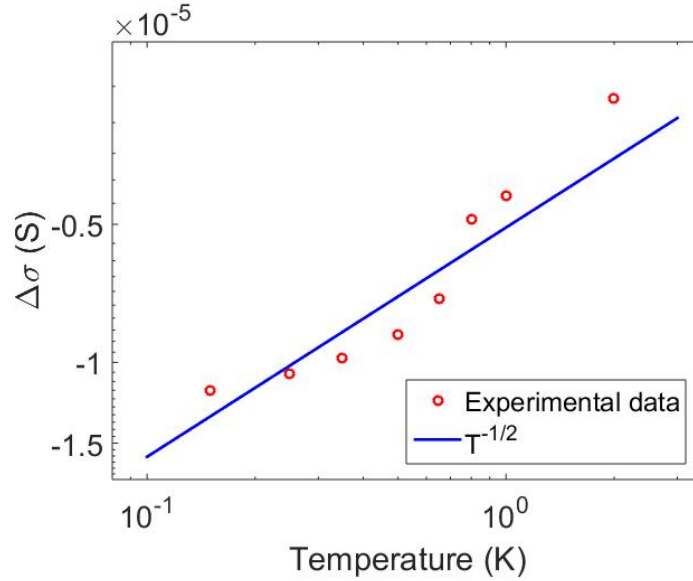


Figure 4.17: The conductance against temperature at  $-1.2V$  split-gate voltage, with weak localisation quenched. The curve is also well fitted with  $\sim T^{-1/2}$ .

The values of  $F$  rising above 1 as  $k_F l$  drops is valid. Similarly Lin et al. [95] calculated a large value for  $F$  in the 2DEG of a  $GaAs - AlGaAs$  heterostructure. Mensz and Wheeler [96] presented data for  $Si - MOSFETs$  in parallel fields indicating a strong enhancement of  $F$  with decreasing carrier concentration. They also suggest spin fluctuations induced by disorder leading to itinerant ferro-magnetism could explain the results.

### 4.4.3 2D-to-1D transitions

Equations 4.19 and 4.21 imply that 2D to 1D transitions occur when the conductivity variance changes from positive to negative at  $1K$ . At temperature above  $1K$ , the variance of the conductivity is positive and negative in 2D and 1D, respectively.

Given this knowledge, we investigated the interaction correction of the

conductivity for several sets of split-gate voltages, and found a 2D-to-1D transition at a split-gate voltage of  $-1.8V$ . Because the plots are similar to those presented previously, we do not display them here. We emphasise, however, that the transition does not depend on the phase-dephasing length, but is influenced only by the channel width and phase coherence length.

# Chapter 5

## Universal Conductance Fluctuations

Universal conductance fluctuations are well reproducible, aperiodic fluctuations in the conductance of small systems. They have bewildered researchers for many years, and have long been regarded as annoying artefacts obscuring the true behaviour of systems. However, these random fluctuations are now considered to be valuable for understanding quantum conductance and measurement. Briefly, mesoscopic systems contain some scattering centres that cannot be explained by the classical technique of averaging over all possible configurations. Specific scattering configurations in the systems will manifest as quantum mechanical interference.

This chapter outlines the theoretical results relating to conductance fluctuations. According to these conductance fluctuations theories, a device that is longer than the phase coherence length in the current direction exhibits conductance fluctuations with universal amplitude at zero temperature. The fluctuations are analysed as functions of the magnetic field in a

*GaAs/AlGaAs* split-gated heterostructure device. The aim is to determine the dominant electronic phase breaking mechanism in the system.

## 5.1 Universal behaviour at $T=0$

The universal nature of conductance fluctuations was first reported by Altshuler [97] and Stone [98]. Stone [98] numerically simulated the magnetoresistance of mesoscopically sized samples, and qualitatively reproduced the aperiodic fluctuations in the fine structures. He concluded that this structure is universal in metal wires. He also found that the field-dependent density of the structure was proportional to the area of the wire, indicating interference among the electronic trajectories in the wire. As the simulations and experiments are all performed in the highly conducting, diffusive regime, the problem is solved by perturbation theory. Altshuler [97] used the perturbation approach to calculate sample-to-sample variations, and Lee and Stone [99] perturbed the chemical potential or magnetic field. The conductance was found to fluctuate at the order of  $e^2/h$ , independently of both the degree of disorder and the sample size at zero temperature. Hence, the conductance fluctuations were dubbed 'universal'. This universality property implies that fluctuations are not merely a finite-size effect, but reveal something fundamental about quantum transport.

The typical amplitude of the fluctuations as a function of energy or magnetic field can be characterised by the root mean square deviation of the conductance:

$$\Delta G = rms(G) = [var(G)]^{\frac{1}{2}} \quad (5.1)$$

At  $T = 0$ , Lee and Stone [99] found that

$$\Delta G = \alpha \frac{e^2}{h} \quad (5.2)$$

where the factor  $\alpha$  reflects a size dependence. In quasi-1D, 2D square samples and 3D cubic samples,  $\alpha = 0.729, 0.862, 1.088$ , respectively.

The origin of the aperiodicity may be understood as follows. Consider the probability of propagating from one point to another in a disordered system. There are many classical random-walk trajectories, each with its own amplitude. Any two of these routes  $p$  and  $p'$ , have an arbitrary phase relationship, and do not contribute the contribution to the interference. In a magnetic field, these two routes form closed loops, acquiring an additional phase difference  $2\pi\phi_{pp'}/\phi_0$  (where  $\phi_{pp'}$  is the flux enclosed by the loop,  $\phi_0 = h/e$ ). The interference term appears only when  $p = p'$ , but is negligible in a small magnetic field. However, if the sample is sufficiently small, then that one route dominates the propagation probability; consequently, the interference terms associated with this route become more important and are no longer negligible. In the metallic regime, many trajectories traverse the sample with similar amplitudes, and stochastically interfere to yield a large fluctuation effect. This suggests that fluctuations in the metallic regime are primarily sourced from configuration changes in impurities, which arbitrarily alter the

phases and cause chaotic interference. Indeed, the fluctuations are found to be extremely sensitive to the changing chemical potential of impurities, as when an impurity move through a small distance. This effect could reveal the extremely slow diffusion of impurities, and may also originate the  $1/f$  noise [100].

The phase of a given impurity configuration, alters under an applied magnetic field. The field must induce a relative phase change of  $2\pi$ . Beyond some field correlation range,  $B_c$ , the phase correlations break. Assuming that a typical pair of routes encloses the sample area,  $B_c$  is given by the field at which the flux passes through the area with magnitude  $\phi_0 = h/e$ . Kaplan and Harstein [101] confirmed this interpretation by demonstrating magnetoconductance fluctuations in pinched channel MOSFETs. Because the interfering routes finally have no fixed phase, the fluctuations in a magnetic field will persist at higher fields, whereas the weak localisation contribution is suppressed at relatively low fields.

A similar correlation length should exist for energy,  $E_c$ . If an energy change simply changes the phase accumulated along a route, then the energy change required for a random phase is related to the time required for the particles to diffuse across the sample; that is,  $E_c \sim hD/(L_x^2)$ , where  $D$  is the diffusion constant.

The correlation ranges are characterised by the conductance correlation function

$$F(\Delta E, \Delta B) = \langle \delta G(E_F, B) \delta G(E_F + \Delta E, B + \Delta B) \rangle \quad (5.3)$$

where  $\delta G = G(E_F, B) - \langle G(E_F, B) \rangle$ . Here, the angular brackets denote the ensemble average. When  $\Delta E = \Delta B = 0$ , this function reduces to the variance  $\Delta G$ , and the correlation ranges  $B_c$  and  $E_c$  are the half widths of  $F(\Delta E = 0, \Delta B)$  and  $F(\Delta E, \Delta B = 0)$ , respectively. These quantities are directly comparable with experimental data.

At  $T = 0$ , further analysis gives [102]:

$$E_c \approx \frac{\pi^2 h D}{L_x^2} \quad (5.4)$$

$$B_c \approx 1.2 \times \frac{\phi_0}{L_x L_y} \quad (5.5)$$

where  $L_x L_y$  is the sample area exposed to the field.

Next, we explore whether the weak localisation behaviour will be masked by amplitude fluctuations of order  $e^2/h$  in  $G(B)$ . In one and two dimensions this is certainly possible, because in 1D, the maximum amplitude of the average conductance at  $T = 0$  (while quenching the weak localisation) is of order  $e^2/h$  in 1D, whereas in 2D, an extra logarithmic correction is required. Thus, the strengths of the two effects should be comparable.

In four-terminal measurements, Büttiker [103] showed that the magnetic field fluctuations are asymmetric around  $B = 0$ . They set the separation of the voltage probes comparable to the phase coherence length, and considered that the wavefunction also extended into the probes. The measured resistance was symmetric around  $B = 0$  after exchanging the roles of the current and voltage leads. A two-terminal measurement also yielded a symmetric result.

## 5.2 Fluctuations at finite temperatures

The typical representation of quantum transport, based on the scaling theory of localisation, applies up to phase coherence length  $L_\phi$ ; at larger length scales, the transport dynamics follow the classical Boltzmann transport law. At sufficiently high temperatures,  $L_\phi$  becomes shorter than the sample dimensions, and the amplitude of the fluctuations depend on the temperature. Within the spatial extent of  $L_\phi$ , electrons propagate at an energy with a defined phase, and interfere in a fixed, time-dependent-manner, giving rise to chaotic fluctuations and weak localisation effects.

Typically, some temperature dependence of  $\text{var}(G(L_\phi))$  is introduced by energy averaging or thermal smearing of the energy levels of  $k_B T$ . This smearing will mix the uncorrelated energy levels in the sum of all routes. The energy fluctuates on a scale of  $E_c = \hbar D/L^2$ . Therefore, the largest system dimension in which the uncorrelated energies are not mixed by thermal broadening is the thermal length, defined as  $L_T = (\hbar D/k_B T)^{1/2}$ .

The conditions for dimensional crossover are determined by the length scales  $L_\phi$  and  $L_T$ . If  $L_\phi < L_T < L$ , the transport is typical quantum transport or combined with classical transport, depending on the ratio of the channel width  $W$  (or  $L_y$ ) to the phase coherence length  $L_\phi$ . When  $L_T < L_\phi < L$ , thermal self-averaging within the spatial extent of  $L_T$  becomes important as explained in Lee et al [102]. If  $L_T < L < L_\phi$ , the temperature dependence of the sample variance is caused only by energy averaging. If all of the temperature-dependent lengths exceeds the sample dimensions, the behaviour matches that at  $T = 0$ .

For variance of  $G(T)$  is given by

$$\Delta G(T) \sim \frac{e^2 L_T}{h L} \left( \frac{L_\phi}{L} \right)^{\frac{1}{2}}, \quad d = 1 \quad \text{and} \quad L_T \ll L_\phi < L_x \quad (5.6)$$

$$\sim \frac{e^2}{h} \left( \frac{L_T}{L} \right)^{\frac{4-d}{2}}, \quad d = 2, 3 \quad \text{and} \quad L_T \ll L_\phi < L_x \quad (5.7)$$

$$\sim \frac{e^2}{h} \left( \frac{L_\phi}{L} \right)^{\frac{4-d}{2}}, \quad d = 1, 2, 3 \quad \text{and} \quad L_\phi \ll L_T < L_x \quad (5.8)$$

where  $L_x$  is the current direction. Other cases, such as  $L_\phi > L_x$  are treated in Altshuler and Khmelnitskii [104] and Lee et al [102].

The dimensionality of the fluctuations depends on  $L_T$ ,  $L_\phi$  and on the sample dimensions  $L_y (\equiv W)$  and  $L_z$  (thickness), as summarised below:

Transition	When	
$3D \rightarrow 2D$	$L_z < L_T, L_\phi$	(5.9)

$2D \rightarrow 1D$	$W < L_\phi$	(5.10)
---------------------	--------------	--------

Note that  $L_\phi$  is the relevant length in 1D even when  $L_\phi > L_T$

In one dimension, the temperature dependence of the magnetic correlation length is always determined by  $L_\phi$ , and matches that at  $T = 0$  until  $L_\phi < L_x$ . That is,

$$B_c(T) \sim 1.2 \times \frac{\phi_0}{L_\phi W}, \quad L_\phi < L_x \quad (5.11)$$

$$\sim 1.2 \times \frac{\phi_0}{L_x W}, \quad L_\phi > L_x \quad (5.12)$$

For narrow devices with  $W < L_\phi < L_x, L_z$ , we have

$$B_c(T) \sim 1.2 \times \frac{\phi_0}{L_{min}W}, \quad W < L_\phi < L_x, L_z \quad (5.13)$$

where  $L_{min}$  is the smaller of  $L_\phi$  and  $L_T$ .

In 2D and 3D samples,  $B_c$  is determined by a change in flux of order  $\phi_0$  through the area defined by  $L_\phi$  and  $L_T$  (whichever is shorter):

$$B_c(T) \sim 1.2 \times \frac{\phi_0}{L_{min}^2} \quad (5.14)$$

At the 1D-to-2D transition, the above equations are inconsistent for  $L_\phi > L_T$ . Here, we must apply the aforementioned corrections to the asymptotic dependences, and  $B_c(T)$  will depend on both  $L_\phi$  and  $L_T$ .

The energy correlation ranges are obtained as:

$$E_c(T) \sim \frac{\hbar}{\tau_\phi}, \quad d = 1 \quad \text{and} \quad L_T < L_\phi < L_x \quad (5.15)$$

$$\sim k_B T, \quad d = 1 \quad \text{and} \quad L_\phi < L_T < L_x \quad (5.16)$$

$$\sim k_B T, \quad d = 2, 3 \quad \text{and} \quad L_\phi, L_T < L_x \quad (5.17)$$

The slow power law dependence of the fluctuation amplitude on temperature, typically  $T^{-1/2}$  to  $T^{-1/4}$ , suggests that the fluctuations are well observable above  $T = 0$ .

## 5.3 Fluctuations in GaAs/AlGaAs heterojunctions

In this section, we analyse the conductance fluctuations in our *GaAs/AlGaAs* heterostructure. The 2D and 1D cases are investigated separately.

### 5.3.1 Fluctuations in 2D

The data were acquired from the device investigated in the previous two chapters; namely a  $2\mu\text{m} \times 1\mu\text{m}$  split-gate on a  $1200\mu\text{m} \times 80\mu\text{m}$  Hall bar. The conductance fluctuations were extracted from the magnetoconductance data in the WL behavioural analysis. The over-filtered data (regarded as the data with no fluctuations) was subtracted from raw data. The relationship between the temperature dependence of the fluctuation variance and  $L_\phi(T)$  (in both 1D and 2D) provides a useful tool to investigating the phase coherence mechanism.

Figure 5.1 shows the conductance fluctuations at different temperature. The traces clearly vary among the temperatures. In general, the amplitude of the trace decreases with increasing temperature, consistent with Eq. 5.7 and 5.8. In the previous two chapters, we found that the thermal dephasing length exceeds the phase coherence length at temperature below  $500\text{mK}$ . This does not affect the temperature dependence because both the phase coherence length and thermal dephasing length exhibit  $\sim T^{-1/2}$  behaviour. In such a long device ( $1200\mu\text{m}$  between the two probes, where the effective length may be much shorter than  $1200\mu\text{m}$ , but still exceeds tens of  $\mu\text{m}$  range) universal fluctuations might not be expected. However, the classical self-

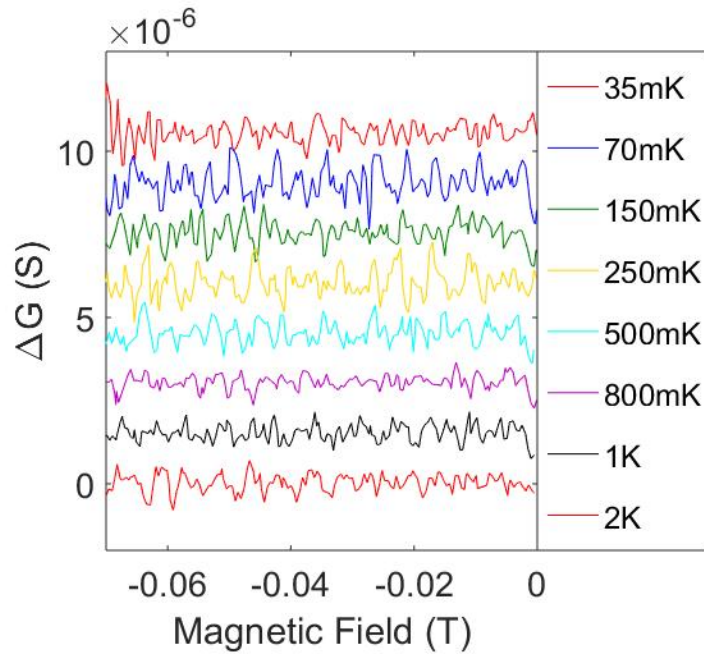


Figure 5.1: 2D conductance fluctuation amplitudes obtained at different temperatures. Each trace is offset by  $1.5\mu S$ .

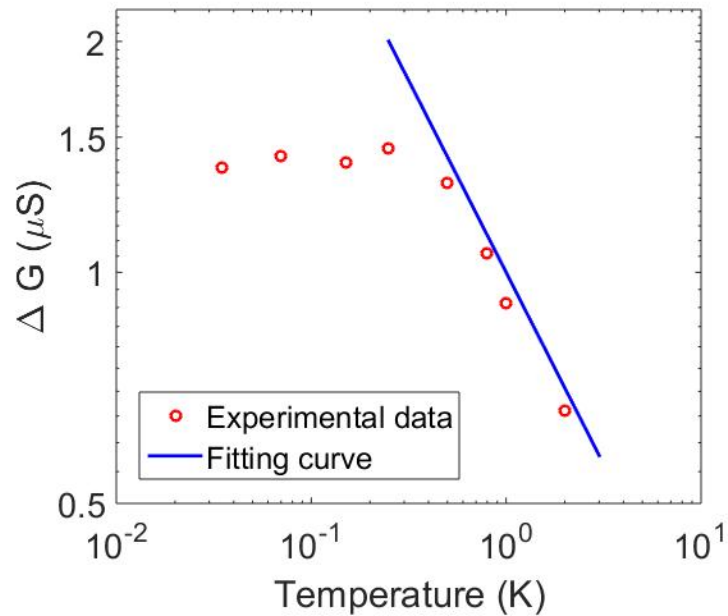


Figure 5.2: Log-log plot of 2D conductance variance versus temperatures. The  $T^{-1/2}$  line is plotted for comparison.

averaging increases very slowly with increasing sample size; namely  $\Delta G \sim e^2/h(L_\phi/L)^{(4-d)/2}$ . In a typical device, this fluctuation constitutes a few percent of the total data, and should be observable. Experimentally, the approximate magnitude of the fluctuation agreed with this estimate.

From the previous section, we understand that the conductance variance should equal the root mean square (RMS) value of the amplitude. The temperature dependence of this conductance variance is plotted in Figure 5.2. The data are well fitted to  $\sim T^{-1/2}$  at higher temperatures, and deviate from this law at lower temperatures. This curve is very similar to Figure 4.4, strongly suggesting that the digamma function simulations are correct. Unfortunately, the phase coherence length cannot be calculated exactly, because the effective length is unpredictable. Assuming that the phase coherence length was correctly estimated in the previous chapters, the present calculation implies that the coherence length cannot exceed  $20\mu m$ .

### 5.3.2 Fluctuations in 1D

One-dimensional fluctuations were investigated at split-gate voltages of  $-0.7V$  and  $-1.1V$  on our sample device. Figure 5.3 displays the RMS variances of the conductance at different temperatures and a split-gate voltage of  $-0.7V$ . In Chapter 4, we found that at this split-gate voltage, the phase coherence length exhibits  $\sim T^{-1/2}$  behaviour at higher temperatures, because it exceeds the thermal dephasing length. Moreover, the channel width exceeds the thermal dephasing length, so the 2D regime is recovered. The  $T^{-1/2}$  behaviour reappears in Figure 5.3, satisfying the WL fitting result. Beyond  $800mK$ , the conductance variances are well fitted to the  $T^{-1/2}$  line.

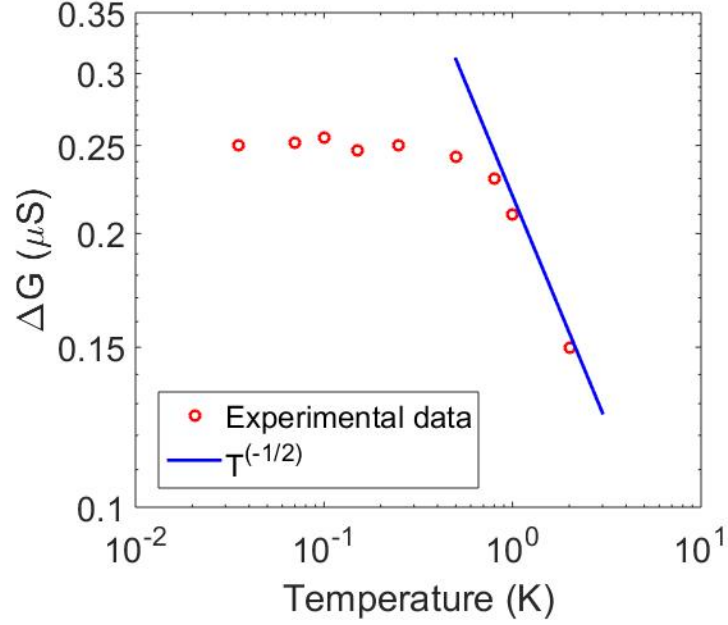


Figure 5.3: Log-log plot of 1D conductance variance versus temperatures at  $-0.7V$  split-gate voltage. The  $T^{-1/2}$  line is also plotted for comparison.

From Eqs. 5.6 and 5.8, conductance variances are given by

$$\Delta G \sim T^{-\frac{1}{2}} \quad L_T > L_\phi \quad (5.18)$$

$$\sim T^{-\frac{2}{3}} \quad L_T < L_\phi \quad (5.19)$$

Therefore, the temperature dependence of variance for 1D exhibits  $T^{-1/2}$  at lower temperatures and  $T^{-2/3}$  behaviour at higher temperatures. Figure 5.4 shows the variance-temperature relationship for the  $-1.1V$  split-gate voltage. The data are properly fitted to the two regimes, but the phase coherence length was wrongly calculated, differing from WL-extracted result by orders of magnitude. We surmise that the pre-processing of the amplitude

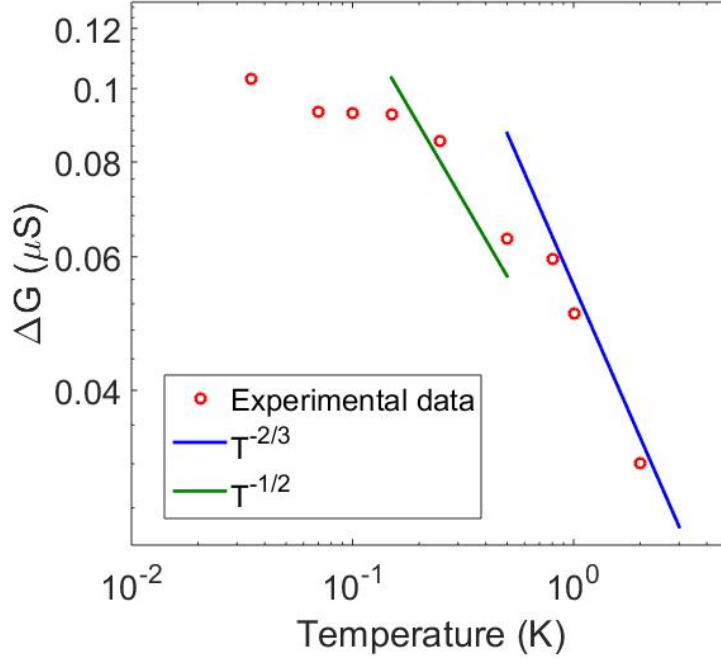


Figure 5.4: Log-log plot of 1D conductance variance versus temperatures at  $-1.1V$  split-gate voltage. The  $T^{-2/3}$  and  $T^{-1/2}$  lines are also plotted for comparison. The correction from 2D ( $T^{-1/2}$ ) to 1D ( $T^{-2/3}$ ) transition happens when  $L_\phi > W$ , but will breakdown and recovered to 2D regime when thermal dephasing length  $L_T > W$ .

fluctuations was insufficient. Nonetheless, the magnitude discrepancy does not affect the temperature dependence of the conductance variance.

In conclusion, the fluctuations observed in the *GaAs/AlGaAs* split-gate device are consistent with accepted theories of quantum conductance in heterojunctions, although the devices are not ideal for investigating such effects. The universal conductance fluctuations were consistent with the weak localisation results. The temperature dependence of conductance fluctuations could provide another tool additional to WL analysis, for exploring dimensional transitions in semiconductor devices.

# Chapter 6

## Magneto-transport in InGaAs/InAlAs Heterojunctions

Indium-based material offer exciting prospects in quantum transport research, on account of their relatively low effective mass, high g-factor and large Rashba effect. Therefore, these materials have become extremely popular. The magnetoresistance behaviour of Indium-based material also have been investigated by many different research groups [105–110]. Knap et al. presented the magnetoconductivity measurements in *InGaAs/InAlAs* quantum well, and had a good agreement between theories and experiments [106]. Koga et al. investigated the Rashba coefficient  $\alpha$  in *InGaAs/InAlAs* quantum well, and compared this  $\alpha$  between theory calculations and experimental values [107]. Hansen et al. [108] and gao et al. [109] both reported on the magnetoconductance measurements in *InAs* nanowires. Hansen et al. [108]

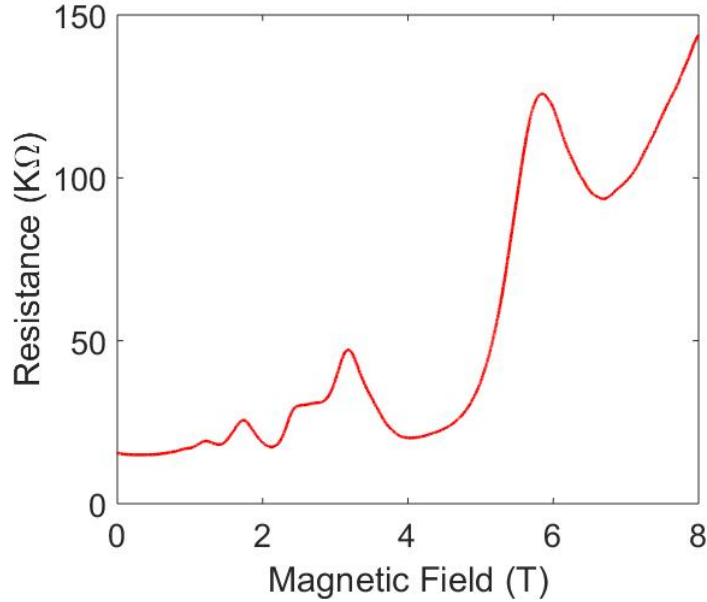


Figure 6.1: Shubnikov-de Haas oscillations at  $0V$  top-gate voltage. The oscillation yield a carrier concentration of  $1.52 \pm 0.1 \times 10^{11} \text{cm}^{-2}$ .

also investigated a crossover from weak localisation to weak antilocalisation by controlling gate voltage. In this chapter, we investigate the magneto-transport properties of the *InGaAs/InAlAs* heterojunction.

## 6.1 Transport in top-gate devices

The experimental devices were fabricated on an *In<sub>0.75</sub>Ga<sub>0.25</sub>As/In<sub>0.75</sub>Al<sub>0.25</sub>As* heterojunction wafer encoded *W402* which was grown by Dr. Ian Farrer in the Cavendish Laboratory, University of Cambridge. The device was fabricated with a global top-gate and Hall bar dimensions of  $1200\mu\text{m} \times 80\mu\text{m}$ . All the experiments were performed in a  $^4\text{He}$  system with a base temperature of  $1.5\text{K}$ .

Figure 6.1 shows the Shubnikov-de Haas oscillation at zero top-gate volt-

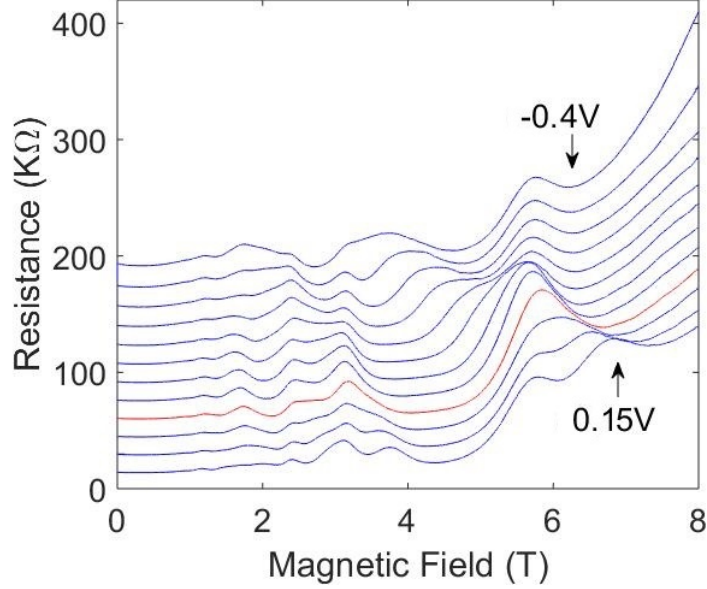


Figure 6.2: Shubnikov-de Haas oscillations at top-gate voltages ranging from  $-0.4V$  to  $0.15V$ . The red trace highlights the zero top-gate voltage.

age. From these oscillations, the carrier concentration was estimated as  $1.52 \pm 0.1 \times 10^{11} \text{cm}^{-2}$  and the mobility was  $5 \pm 0.2 \times 10^4 \text{cm}^2 / (\text{V} \cdot \text{s})$ . Figure 6.2 shows the Shubnikov-de Haas oscillation at various top-gate voltages (including  $0V$ ). An obvious crossing appears at magnetic fields between  $4T$  and  $7T$ . This crossing should originate from spin-orbit interactions, which are expected in *InGaAs/InAlAs* heterojunctions. Figure 6.3 presents Fourier transform spectra of the SdH data. The top-gate normally is designed as micrometres shorter than the whole channel at both ends along the channel, thus there will always include a 2D region no matter what gate voltages applied. This constant carrier concentration is also reflected in Fourier transform spectra. The spectra also reveal two different conducting channels in the device, designated  $\alpha$  and  $\beta$ . Both channels exhibit two peaks at a top-gate voltage of  $-0.4V$ , confirming spin-orbit interactions.

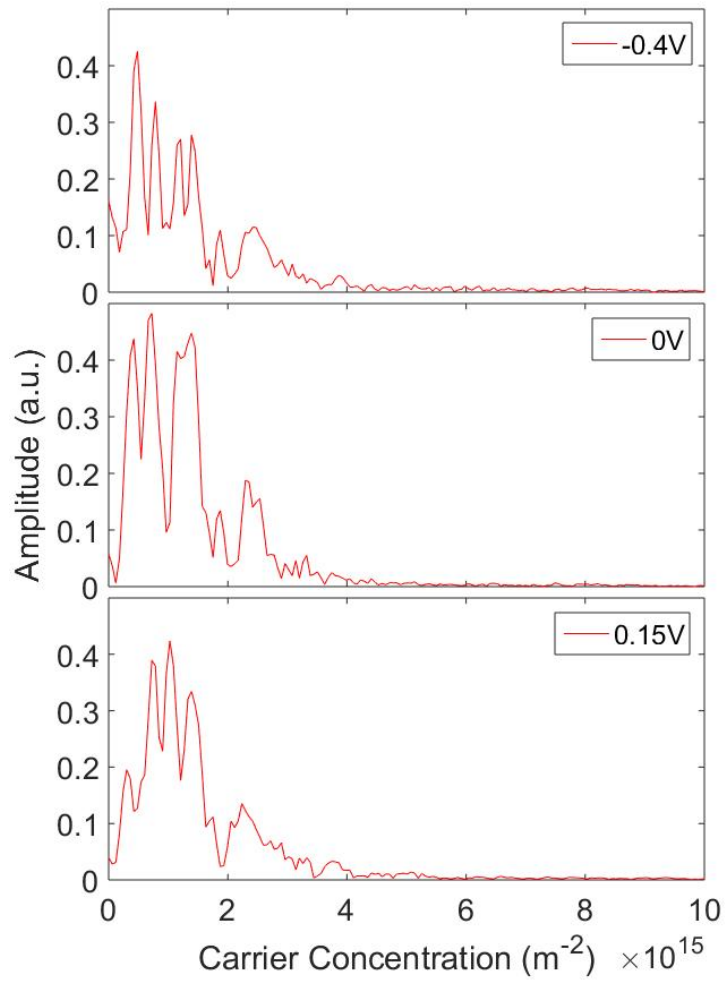


Figure 6.3: Fourier transform spectra of SdH data at different top-gate voltages.

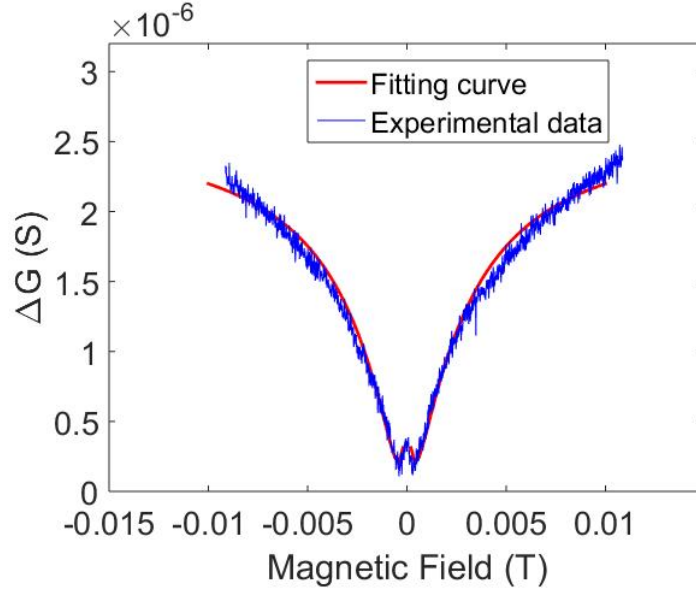


Figure 6.4: Fitting result of 2D magnetoresistance with a WAL effect. The  $\tau_{SO}$  is obtained by the fitting is  $5ps$ .

The magnetoresistance was also measured at various top-gate voltages. The resulting curves were fitted to digamma function including a spin parameter. Figure 6.4 displays the general fitting result at zero top-gate voltage. The WAL feature is visible but not strong. The estimated phase coherence length was  $550 \pm 10nm$ , and spin-orbit coherence time is  $4 \pm 0.1 \times 10^{-12}s$ . This value is smaller than the one we get from *GaAs/AlGaAs* heterostructure ( $17ps$ ). At negative top-gate voltages (lower density), the WAL feature becomes weakened and eventually smeared out. This is predictable because the top-gate breaks the structure inversion asymmetry of the device.

Next, we investigated the temperature dependence of the phase coherence length. An unexpected result appeared even before the temperature-dependence measurements began. The device presented a huge resistance (as though non-conducting), and was revived only under one minute of full

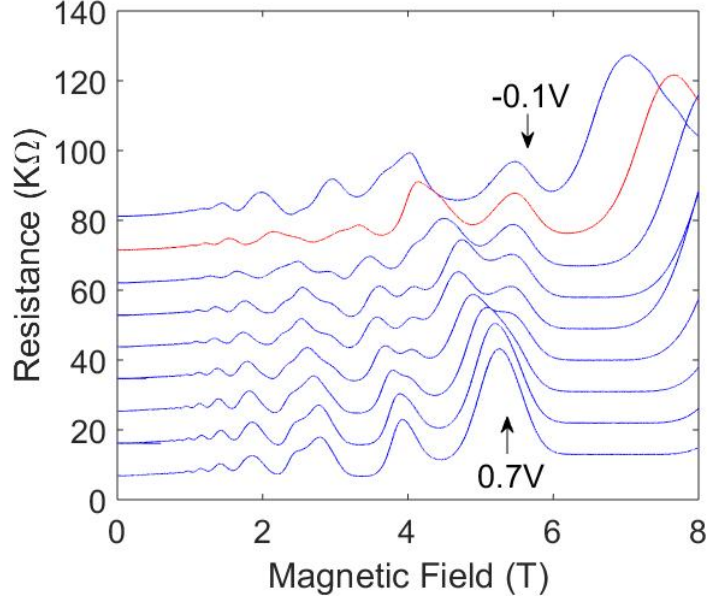


Figure 6.5: Shubnikov-de Haas oscillations in the device revived by illumination at top-gate voltages ranging from  $-0.1V$  to  $0.7V$ . The red trace highlights the zero top-gate voltage.

illumination. However, the illumination completely changed the device characteristics. The SdH measurements of the device after flashing are shown in Figure 6.5. From these oscillations, the carrier concentration was calculated as  $2.99 \pm 0.1 \times 10^{11} cm^{-2}$ . The Fourier transform spectra of the post-flashing SdH data are presented in Figure 6.6.

Figure 6.7 plots the result of temperature dependence of the phase coherence length at zero top-gate voltage. Here, we employed the digamma function without a spin parameter is occupied because no obvious WAL feature appeared. The temperature dependence ( $T^{1/2}$ ) is consistent with the 2D regime.

We also studied the interaction effect of this device. Figure 6.8 shows the result of fitting to  $\log(T)$ , from which the screened Coulomb potential  $F$  was

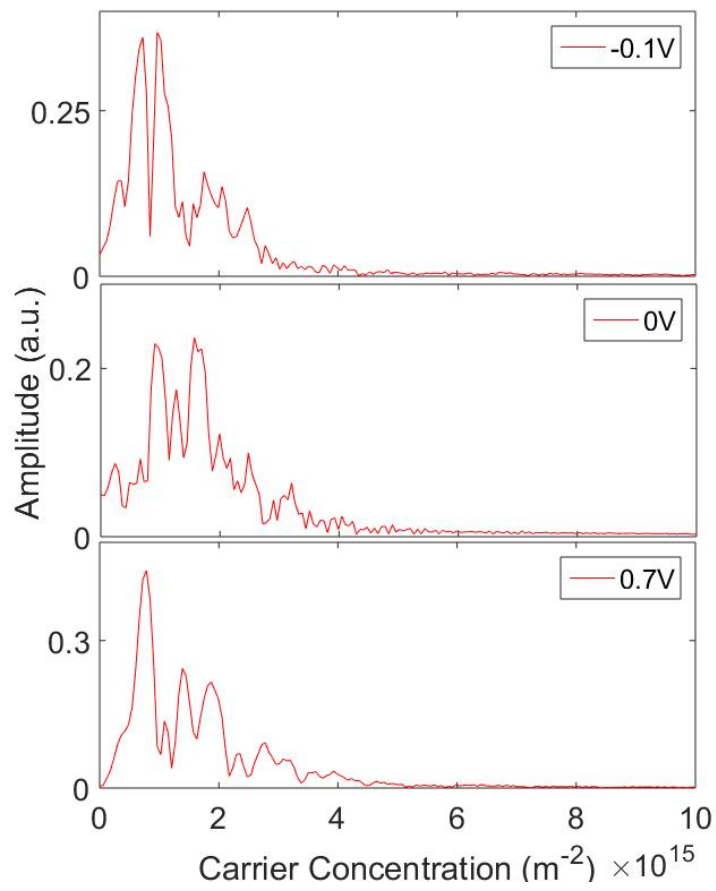


Figure 6.6: Fourier transform spectra of SdH data at different top-gate voltages.

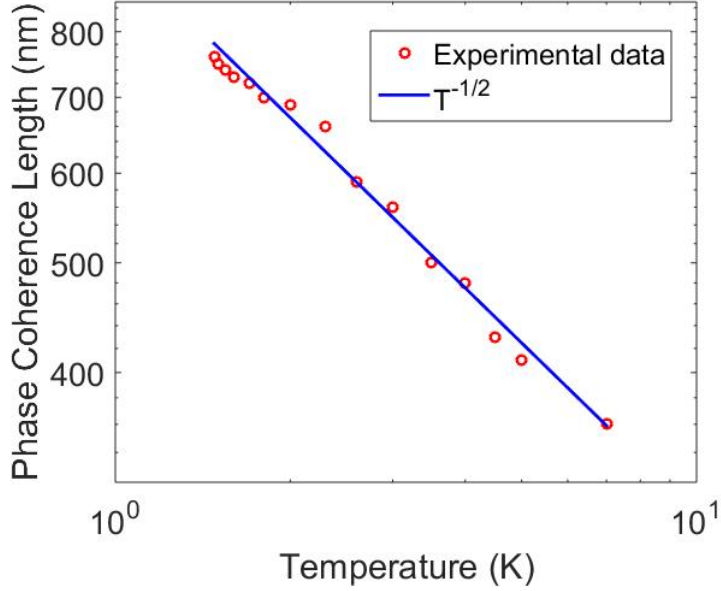


Figure 6.7: Temperature dependence of phase coherence length. The  $T^{-1/2}$  regime is plotted for comparison.

determined as 0.362. This value indicating the interaction is weak compare to the previous *GaAs/AlGaAs* heterostructure.

## 6.2 Transport in split-gate devices

The transport properties were measured in a  $In_{0.75}Ga_{0.25}As/In_{0.75}Al_{0.25}As$  heterojunction wafer encoded *W436*. This wafer was also grown by MBE in the Cavendish Laboratory, University of Cambridge. The dimensions of the split-gate were  $1\mu m \times 5\mu m$  ( $L \times W$ ). All experiments were performed in a dilution system at a base temperature of  $35mK$ .

Figure 6.9 shows the Shubnikov-de Haas oscillations at various split-gate voltages. The pinch-off voltage of this device was  $\sim -2V$ . At higher split-gate voltages, the oscillations fluctuated more randomly, so we limited the

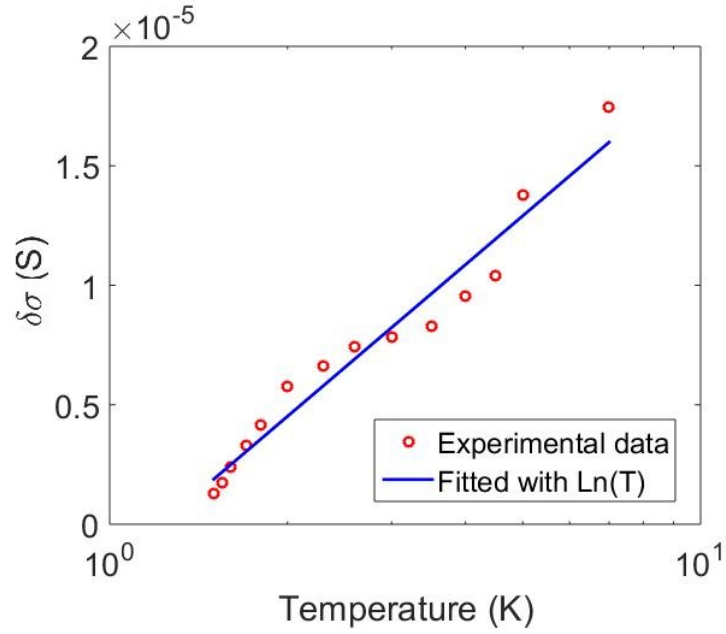


Figure 6.8: Conductance versus temperature, with weak localisation quenched. The curve is well fitted to  $\sim \ln(T)$ .

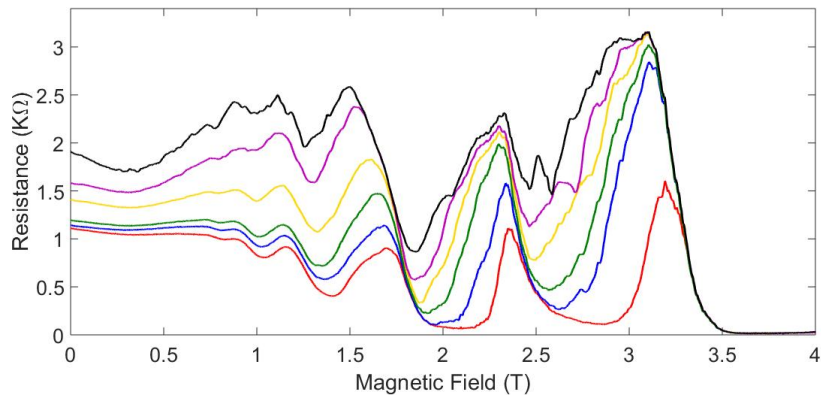


Figure 6.9: Shubnikov-de Haas oscillations at various split-gate voltages (From bottom to top:  $0V$ ,  $-0.2V$ ,  $-0.4V$ ,  $-0.6V$ ,  $-0.8V$  and  $-1V$ ).

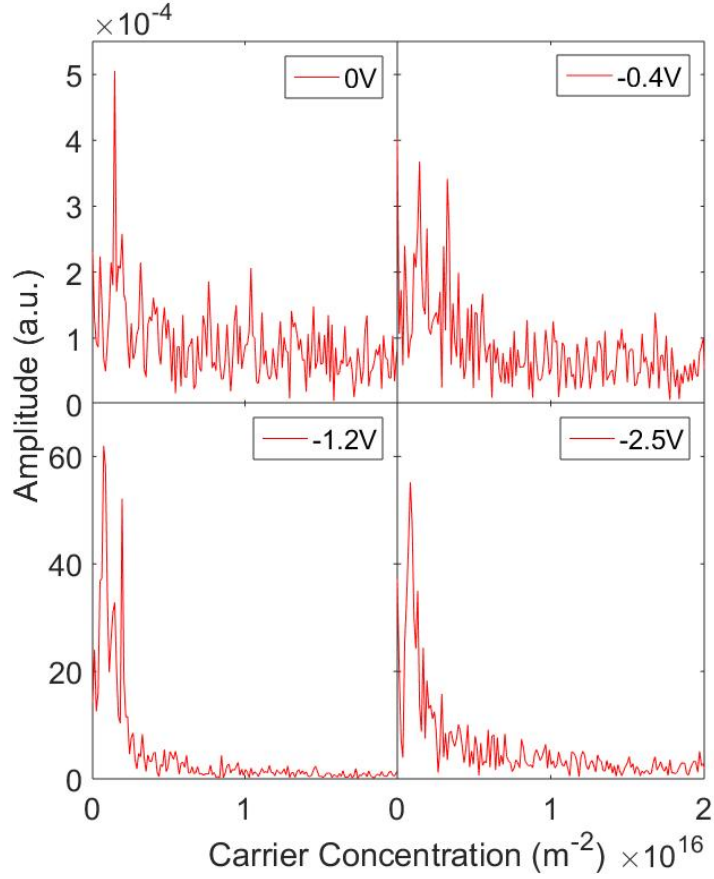


Figure 6.10: Fourier transform spectra of SdH data at different split-gate voltages.

SdH measurement to low split-gate voltages. Figure 6.10 presents the Fourier transform spectra of the SdH data. Only one channel appears at zero split-gate voltage, but two channels exist at non-zero split-gate voltages. The system reverts to one-channel at the split-gate voltage of near pinch-off of the channel.

In these data, the positions (magnetic fields) of the oscillation minima clearly vary, indicating magneto-depopulation of the Landau levels. Figure 6.11 plots the oscillation peak as a function of  $1/B$ . As the split-gate volt-

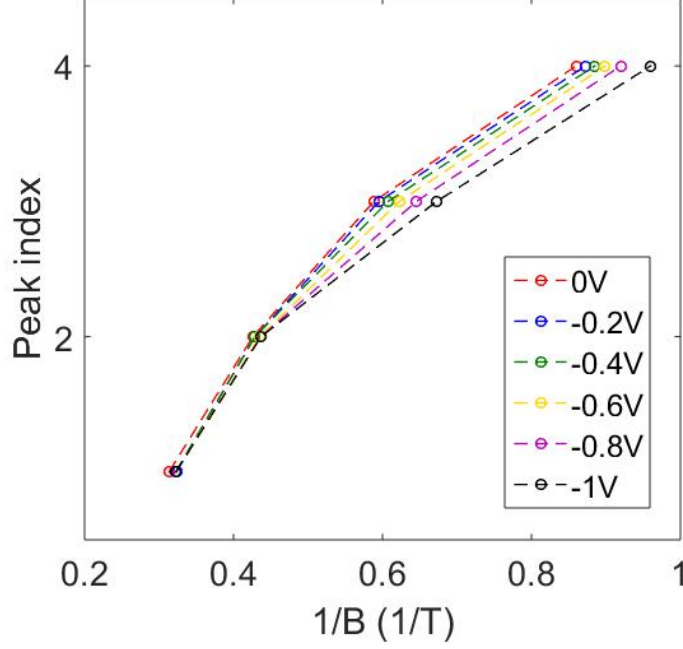


Figure 6.11: Oscillation peak versus  $1/B$  at different split-gate voltages. The y-axis which represents the peak index start from the  $4T$  to lower field. Only 4 sets of data which corresponds to different peaks are analysed, this is because they are the only 4 peaks are visible in SdH.

age increases, the plots deviate from linearity, indicating broadening of the Landau levels and also decrease of the carrier concentration.

The carrier concentration and mobility were calculated as  $1.91 \pm 0.1 \times 10^{-11} \text{cm}^2$  and  $4 \pm 0.2 \times 10^5 \text{cm}^2 / (\text{V} \cdot \text{s})$ , respectively. We also attempted a digamma function fitting (see Figure 6.12). Note that the 2D digamma function with the spin-coherence term (Eq. 2.36) is not applicable here for two reasons. First, the WAL feature is not visible; second, Eq. 2.36 yielded a worse fitting result than to the original digamma function. From the fitting, the phase coherence length was determined as  $590 \pm 10 \text{nm}$ .

We also measured this device at higher temperatures, but the data con-

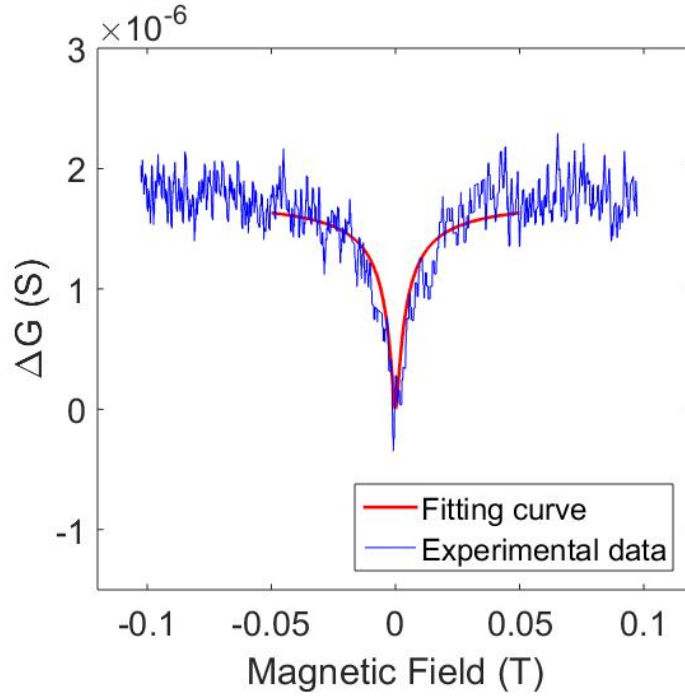


Figure 6.12: Fitting result of zero split-gate voltage at the base temperature (35mK).

tinued to exhibit no WAL, and their quality was not improved. Because of the poor data quality, no further WAL experiments were performed on the current device. The *InGaAs* devices are useful for investigating spin-orbit interactions, but there are no obvious WAL features to explore. There may have two reasons of that: 1.the low value phase coherence length, that indicating huge amount of scattering time inside the systems; 2.the structure inversion asymmetry does not form well.

# Chapter 7

## Conclusions and suggestions

The work fully investigated quantum interference and dimensionality transitions in disordered group III-V systems. The magnitude and dimensionality of the quantum interference correction is governed by the phase coherence length  $L_\phi$ . The transport will be taken into 1D from 2D if  $L_\phi > W$ , where  $W$  is width of the conducting channel. The disordered system can be divided into three regimes: quasi-metallic, metal-to-insulator transition (MIT) and insulating. The present study focused on the quasi-metallic regime. Through measuring the magnetoresistance behaviour of group III-V heterostructure devices at different split-gate voltage, and fitting the data with the theoretical equations, the phase coherent information of the devices can be extracted. The different temperature dependences of these phase coherent information represented the different dimensional regimes of the electron transport. At low temperatures, the electron-electron scattering dominated, and the Nyquist process is expected which predict the dimensionality transition happens from  $L_\phi \sim T^{-1/2}$  dependence transform to  $L_\phi \sim T^{-1/3}$ .

The background information was introduced in chapter 1, which gave a

brief understanding of transport theory in low dimensional system at low temperatures. Some reviews of electronic transport in disordered systems was given in chapter 2. This emphasised the dimensionality dependences of the different corrections, including the various criteria determining the effective dimensionality in each case. Chapter 3 described the techniques and procedures of sample fabrication, as well as a brief introduction of the experimental instruments and set-ups.

In Chapter 4, the phase coherence information was extracted by investigating the weak localisation effect(Negative magnetoresistance) at various temperature, the different temperature dependence regime of  $L_\phi$  reflected the dimensionality transition of transport. With the help of split-gate(QPC), it was easy to achieve dimensionality transition in a 2DEG. Since a magnetic field destroyed the electronic phase coherence required for quantum interference, the magnitude of  $L_\phi$  could be extracted from the measured low field magnetoresistance in a dilution system. The  $L_\phi$  was extracted by fitting the 2D equation, and fitted with  $T^{-1/2}$  at temperature range  $T > 650mK$ . As the split-gate voltage increased to  $-0.18V$ , the  $L_\phi > W$ , and the data fitted well with 1D equation, but the temperature dependence of  $L_\phi$  was still  $T^{-1/2}$ . This was because at the temperature range  $T > 650mK$ , the thermal dephasing length was still shorter than  $W$  at this split-gate voltage, the 2D temperature dependence still governed. As the  $W$  became longer than the thermal dephasing length, the 1D dependence showed up. The 1D dependence of  $L_\phi \sim T^{-1/3}$  happened at the split-gate voltage equalled to  $-1.1V$ . These were all consistent with theoretical prediction. However, a saturation of this dependence was found at temperature  $T < 650mK$ .

This unexpected saturation was suggested that manifesting from spin-flip scattering by magnetic impurities. Furthermore, an abnormal shoulder behaviour of magnetoresistance was observed as the split-gate squeezing. The origin of this behaviour could be the interactions between smooth disorder or macroscopic defects in the material. The contribution to the phase destruction from the Landau-Baber process was also investigated. A same prefactor of the Landau-Baber term in both 2D and 1D was found, which was expected because the dimensionality of this term was not set by thermal dephasing length, but by the density of states. The anti-localisation effect was observed in 1D regime at  $2K$ . A good fitting with theoretical equation was attempted. Since there might exist the spin-flip scattering inside the system, it was not possible to distinguish the spin-orbit interaction from spin-flip scattering term. The electron-electron interaction correction in both 2D and 1D were measured, and found the  $\sim \ln(T)$  and  $\sim T^{-1/2}$  dependence, respectively. The screened Coulomb potentials  $F$  were determined as 1.24 in 2D and 5.88 in 1D. Both of them were significantly large than the maximum theoretical value 1, but many other authors had suggested that the value of  $F$  could become very large as  $k_F l$  drops.

The behaviour of the universal conductance fluctuations as a function of temperature were also found and discussed in chapter 5. Using theories which characterised the fluctuations in terms of  $L_\phi$  and  $L_T$ , the data was analysed to determine the dominant phase breaking mechanism. The Nyquist result was found in both 2D and 1D, giving an important confirmation of the earlier conclusions, though the magnitude of the correction was different to theoretically expected. The saturation of both dependences at lower temperature

part was also observed.

The *InGaAs/InAlAs* interpreted the low-temperature transport phenomena with spin-orbit interaction was experimentally investigated in Chapter 6. The analysis of SdH and QHE were attempted in  $^3\text{He}$  system. The positive magnetoresistance was observed and investigated in a top-gate device, and a spin-scattering time of  $4 \pm 0.1 \times 10^{-12} \text{s}$  was determined. This value was much smaller than  $17 \text{ps}$  which determined from *GaAs/AlGaAs* system previously, indicating a stronger spin-orbit interaction happened. The interaction effect was also investigated, and a screened Coulomb potential of 0.362 was extracted from the data. The magneto depopulation in a split-gate *InGaAs/InAlAs* device was also investigated in this chapter.

However, several problems remain. In Chapter 4, the temperature dependence of the phase coherence length deviated at lower temperatures ( $T < 650 \text{mK}$ ), possibly because of spin-flip scattering by magnetic impurities in the fabricated device. Second, when the spin parameter participates in the fitting process, it affects the estimated phase coherence length. Third, we could not distinguish the WAL induced by spin-flip scattering from that of spin-orbit interactions. Fourth, we should also study devices with lengths shorter than the phase coherence length. Fifth, the origin of shoulder behaviour in magnetoresistance investigating still need to be found. Finally, in Chapter 6, we could not observe the WAL in 1D transport in the split-gate *InGaAs* heterostructure. These problem will be prioritised in future experiments.

To comprehensively understand the quantum transport and electron behaviour at low temperatures, we should also investigate the MIT and insu-

lating regimes.

# References

- [1] Xi-De Xie and Dong Lu. Energy band theory of solids, 1998.
- [2] K-F Berggren and Michael Pepper. Electrons in one dimension. *Philosophical Transactions of the Royal Society of London A: Mathematical, Physical and Engineering Sciences*, 368(1914):1141–1162, 2010.
- [3] KJ Thomas, JT Nicholls, NJ Appleyard, MY Simmons, M Pepper, DR Mace, WR Tribe, and DA Ritchie. Interaction effects in a one-dimensional constriction. *Physical Review B*, 58(8):4846, 1998.
- [4] BJ Van Wees, H Van Houten, CWJ Beenakker, J Gr Williamson, LP Kouwenhoven, D Van der Marel, and CT Foxon. Quantized conductance of point contacts in a two-dimensional electron gas. *Physical Review Letters*, 60(9):848, 1988.
- [5] DA Wharam, Trevor John Thornton, R Newbury, M Pepper, H Ahmed, JEF Frost, DG Hasko, DC Peacock, DA Ritchie, and GAC Jones. One-dimensional transport and the quantisation of the ballistic resistance. *Journal of Physics C: solid state physics*, 21(8):L209, 1988.
- [6] CWJ Beenakker and Henk van Houten. Quantum transport in semiconductor nanostructures. *Solid state physics*, 44(1):228, 1991.

- [7] K von Klitzing, Gerhard Dorda, and Michael Pepper. New method for high-accuracy determination of the fine-structure constant based on quantized hall resistance. *Physical Review Letters*, 45(6):494, 1980.
- [8] RB Laughlin. Impurities and edges in the quantum hall effect. *Surface Science*, 113(1):22–26, 1982.
- [9] RE Prange. Quantized hall resistance and the measurement of the fine-structure constant. *Physical Review B*, 23(9):4802, 1981.
- [10] H Aoki and T Ando. Effect of localization on the hall conductivity in the two-dimensional system in strong magnetic fields. *Solid State Communications*, 38(11):1079–1082, 1981.
- [11] JT Chalker. The hall effect in a two-dimensional electron gas. *Journal of Physics C: Solid State Physics*, 16(21):4297, 1983.
- [12] W Brenig. Quantized hall conductance: Effect of random potentials. *Zeitschrift für Physik B Condensed Matter*, 50(4):305–309, 1983.
- [13] T Ando. Electron localization in a two-dimensional system in strong magnetic fields. i. case of short-range scatterers. *Journal of the Physical Society of Japan*, 52(5):1740–1749, 1983.
- [14] A MacKinnon, L Schweitzer, and B Kramer. Magneto-transport in two dimensions: Some numerical results. *Surface Science*, 142(1):189–195, 1984.
- [15] L Schweitzer, B Kramer, and A MacKinnon. Magnetic field and electron states in two-dimensional disordered systems. *Journal of Physics C: Solid State Physics*, 17(23):4111, 1984.

- [16] H Aoki and T Ando. Critical localization in two-dimensional landau quantization. *Physical review letters*, 54(8):831, 1985.
- [17] Srivastava Richa. Investigation on temperature sensing of nanostructured zinc oxide synthesized via oxalate route. *Journal of Sensor Technology*, 2012, 2012.
- [18] T Ando. Theory of quantum transport in a two-dimensional electron system under magnetic fields. iv. oscillatory conductivity. *Journal of the Physical Society of Japan*, 37(5):1233–1237, 1974.
- [19] NF Mott. The basis of the electron theory of metals, with special reference to the transition metals. *Proceedings of the Physical Society. Section A*, 62(7):416, 1949.
- [20] Gabriel Kotliar and Dieter Vollhardt. Strongly correlated materials: Insights from dynamical mean-field theory. *Physics Today*, 57(3):53–60, 2004.
- [21] PW Anderson. Absence of diffusion in certain random lattices. *Physical review*, 109(5):1492, 1958.
- [22] JT Edwards and DJ Thouless. Numerical studies of localization in disordered systems. *Journal of Physics C: Solid State Physics*, 5(8):807, 1972.
- [23] NF Mott. Electrons in disordered structures. *Advances in Physics*, 16(61):49–144, 1967.
- [24] NF Mott. Conduction in amorphous materials. *Electronics & Power*, 19(14):321–324, 1973.

- [25] F Stern. Evidence for a mobility edge in inversion layers. *Physical Review B*, 9(6):2762, 1974.
- [26] M Pepper. A metal-insulator transition in the impurity band of n-type gaas induced by loss of dimension. *Journal of Physics C: Solid State Physics*, 10(8):L173, 1977.
- [27] NF Mott and EA Davis. Dc mattes due either to a mott-or anderson-type transition. see especially. *Phil. Mag*, 17:1269, 1968.
- [28] NF Mott and WD Twose. The theory of impurity conduction. *Advances in Physics*, 10(38):107–163, 1961.
- [29] DJ Thouless. Maximum metallic resistance in thin wires. *Physical Review Letters*, 39(18):1167, 1977.
- [30] E Abrahams, PW Anderson, DC Licciardello, and TV Ramakrishnan. Scaling theory of localization: Absence of quantum diffusion in two dimensions. *Physical Review Letters*, 42(10):673, 1979.
- [31] GJ Dolan and DD Osheroff. Nonmetallic conduction in thin metal films at low temperatures. *Physical Review Letters*, 43(10):721, 1979.
- [32] MJ Uren, RA Davies, and M Pepper. The observation of interaction and localisation effects in a two-dimensional electron gas at low temperatures. *Journal of Physics C: Solid State Physics*, 13(33):L985, 1980.
- [33] G Bergmann. Weak localization in thin films: a time-of-flight experiment with conduction electrons. *Physics Reports*, 107(1):1–58, 1984.

- [34] DJ Newson, CM McFadden, and M Pepper. Quantum corrections and the metal-insulator transition as a function of dimensionality in the gaas impurity band. *Philosophical Magazine B*, 52(3):437–458, 1985.
- [35] T Ando, T Nakanishi, and R Saito. Berry’s phase and absence of back scattering in carbon nanotubes. *Journal of the Physical Society of Japan*, 67(8):2857–2862, 1998.
- [36] BL Altshuler and AG Aronov. Electron density of states and energy relaxation time in magnetic field. *Solid State Communications*, 38(1):11–15, 1981.
- [37] BL Altshuler, AG Aronov, and PA Lee. Interaction effects in disordered fermi systems in two dimensions. *Physical Review Letters*, 44(19):1288, 1980.
- [38] S Hikami, AI Larkin, and Y Nagaoka. Spin-orbit interaction and magnetoresistance in the two dimensional random system. *Progress of Theoretical Physics*, 63(2):707–710, 1980.
- [39] BL Altshuler and AG Aronov. Magnetoresistance of thin films and of wires in a longitudinal magnetic field. *JETP Lett.*, 33(10):499–501, 1981.
- [40] Y Aharonov and D Bohm. Significance of electromagnetic potentials in the quantum theory. *Physical Review*, 115(3):485, 1959.
- [41] BL Altshuier, AG Aronov, and BZ Spivak. The aaronov-bohm effect in disordered conductors. *Jetp Lett*, 33(2), 1981.

- [42] G Bergmann. Physical interpretation of weak localization: A time-of-flight experiment with conduction electrons. *Physical Review B*, 28(6):2914, 1983.
- [43] BL Altshuler and AG Aronov. Zero bias anomaly in tunnel resistance and electron-electron interaction. *Solid State Communications*, 30(3):115–117, 1979.
- [44] BL Altshuler and AG Aronov. Solid state comm. 30, 115 (1979). *JETP*, 50:968, 1979.
- [45] BL Altshuler and AG Aronov. *Electron-electron interaction in disordered conductors*. Elsevier, 1985.
- [46] H Fukuyama. Effects of interactions on non-metallic behaviors in two-dimensional disordered systems. *Journal of the Physical Society of Japan*, 48:2169, 1980.
- [47] PA Lee and TV Ramakrishnan. Disordered electronic systems. *Reviews of Modern Physics*, 57(2):287, 1985.
- [48] BL Altshuler, AG Aronov, AI Larkin, and DE Khmel'nitskii. Zh. é ksp. teor. fiz. 54, 411 1981 sov. phys. *JETP*, 81:788, 1981.
- [49] WG Baber. The contribution to the electrical resistance of metals from collisions between electrons. *Proceedings of the Royal Society of London. Series A, Mathematical and Physical Sciences*, 158(894):383–396, 1937.
- [50] E Abrahams. Electron-electron scattering in alkali metals. *Physical Review*, 95(3):839, 1954.

- [51] A Schmid. On the dynamics of electrons in an impure metal. *Zeitschrift für Physik*, 271(3):251–256, 1974.
- [52] E Abrahams, PW Anderson, PA Lee, and TV Ramakrishnan. Quasi-particle lifetime in disordered two-dimensional metals. *Physical Review B*, 24(12):6783, 1981.
- [53] H Fukuyama and E Abrahams. Inelastic scattering time in two-dimensional disordered metals. *Physical Review B*, 27(10):5976, 1983.
- [54] BL Altshuler, AG Aronov, and DE Khmel'nitsky. Effects of electron-electron collisions with small energy transfers on quantum localisation. *Journal of Physics C: Solid State Physics*, 15(36):7367, 1982.
- [55] H Fukuyama. A note on inelastic scattering time in two-dimensional weakly localized regime. *Journal of the Physical Society of Japan*, 53(10):3299–3302, 1984.
- [56] Y Isawa. Inelastic scattering time in disordered metals. *Journal of the Physical Society of Japan*, 53(9):2865–2867, 1984.
- [57] PJ Price. Polar-optical-mode scattering for an ideal quantum-well heterostructure. *Physical Review B*, 30(4):2234, 1984.
- [58] N Giordano, W Gilson, and DE Prober. Experimental study of anderson localization in thin wires. *Physical Review Letters*, 43(10):725, 1979.
- [59] P Chaudhari and HU Habermeier. Quantum localization in amorphous w-re alloys. *Physical Review Letters*, 44(1):40, 1980.

- [60] AE White, M Tinkham, WJ Skocpol, and DC Flanders. Evidence for interaction effects in the low-temperature resistance rise in ultrathin metallic wires. *Physical Review Letters*, 48(25):1752, 1982.
- [61] P Santhanam, S Wind, and DE Prober. One-dimensional electron localization and superconducting fluctuations in narrow aluminum wires. *Physical review letters*, 53(12):1179, 1984.
- [62] JT Masden and N Giordano. Localization and electron-electron interaction effects in thin pt wires. *Physical Review B*, 31(10):6395, 1985.
- [63] JJ Lin and N Giordano. Observation of the nyquist phase-coherence time in thin au-pd wires. *Physical Review B*, 33(2):1519, 1986.
- [64] JJ Lin and N Giordano. Localization and electron-electron interaction effects in thin au-pd films and wires. *Physical Review B*, 35(2):545, 1987.
- [65] S Wind, MJ Rooks, V Chandrasekhar, and DE Prober. One-dimensional electron-electron scattering with small energy transfers. *Physical review letters*, 57(5):633, 1986.
- [66] AP Heraud, SP Beaumont, CDW Wilkinson, PC Main, JR Owers-Bradley, and L Eaves. Inelastic electron scattering in pseudo-one-dimensional metal wires. *Journal of Physics C: Solid State Physics*, 20(13):L249, 1987.
- [67] P Santhanam, S Wind, and DE Prober. Localization, superconducting fluctuations, and superconductivity in thin films and narrow wires of aluminum. *Physical Review B*, 35(7):3188, 1987.

- [68] JM Gordon. Quantum phase sensitivity to macroscopic boundaries: Al cylinders and wires. *Physical Review B*, 30(11):6770, 1984.
- [69] KK Choi, DC Tsui, and SC Palmateer. Size effects on electron-electron interactions in  $\text{GaAs-Al}_{1-x}\text{Ga}_x$  heterostructures. *Physical Review B*, 32(8) : 5540, 1985.
- [70] KK Choi, DC Tsui, and SC Palmateer. Dimensional cross-over of electron-electron interactions in  $\text{GaAs/Al}_{1-x}\text{Ga}_x$  heterostructures. *Surface Science*, 170(1) : 708 – 712, 1986.
- [71] TJ Thornton, M Pepper, H Ahmed, D Andrews, and GJ Davies. One-dimensional conduction in the 2d electron gas of a  $\text{GaAs-AlGaAs}$  heterojunction. *Physical review letters*, 56(11):1198, 1986.
- [72] KF Berggren, TJ Thornton, DJ Newson, and M Pepper. Magnetic depopulation of 1d subbands in a narrow 2d electron gas in a  $\text{GaAs:AlGaAs}$  heterojunction. *Physical review letters*, 57(14):1769, 1986.
- [73] HZ Zheng, HP Wei, DC Tsui, and G Weimann. Gate-controlled transport in narrow  $\text{GaAs/Al}_x\text{Ga}_{1-x}$  heterostructures. *Physical Review B*, 34(8):5635, 1986.
- [74] CC Dean and M Pepper. One-dimensional electron localisation and conduction of electron-electron scattering in narrow silicon mosfets. *Journal of Physics C: Solid State Physics*, 17(31):5663, 1984.
- [75] DJ Thouless. The effect of inelastic electron scattering on the conductivity of very thin wires. *Solid State Communications*, 34(8):683–685, 1980.

- [76] TJ Thornton, ML Roukes, A Scherer, and BP Van de Gaag. Boundary scattering in quantum wires. *Physical review letters*, 63(19):2128, 1989.
- [77] L Bockhorn, P Barthold, D Schuh, W Wegscheider, and RJ Haug. Magnetoresistance in a high-mobility two-dimensional electron gas. *Physical Review B*, 83(11):113301, 2011.
- [78] L Bockhorn, IV Gornyi, D Schuh, W Wegscheider, and RJ Haug. Interaction-induced huge magnetoresistance in a high mobility two-dimensional electron gas. In *American Institute of Physics Conference Series*, volume 1566, pages 289–290, 2013.
- [79] L Bockhorn, A Hodaei, D Schuh, W Wegscheider, and RJ Haug. Magnetoresistance in a high mobility two-dimensional electron system as a function of sample geometry. In *Journal of Physics: Conference Series*, volume 456, page 012003. IOP Publishing, 2013.
- [80] L Bockhorn, IV Gornyi, D Schuh, C Reichl, Werner Wegscheider, and RJ Haug. Magnetoresistance induced by rare strong scatterers in a high-mobility two-dimensional electron gas. *Physical Review B*, 90(16):165434, 2014.
- [81] L Bockhorn, A Velieva, S Hakim, T Wagner, EP Rugeramigabo, D Schuh, C Reichl, W Wegscheider, and RJ Haug. Influence of oval defects on transport properties in high-mobility two-dimensional electron gases. *Applied Physics Letters*, 108(9):092103, 2016.
- [82] JT Masden and N Giordano. Length-dependent resistance of thin wires. *Physical Review Letters*, 49(11):819, 1982.

- [83] KK Choi, DC Tsui, and SC Palmateer. Electron-electron interactions in  $\text{GaAs-Al}_x\text{Ga}_{1-x}$  heterostructures. *Physical Review B*, 33(12) : 8216, 1986.
- [84] T Hiramoto, K Hirakawa, Y Iye, and T Ikoma. Phase coherence length of electron waves in narrow  $\text{AlGaAs/GaAs}$  quantum wires fabricated by focused ion beam implantation. *Applied physics letters*, 54(21):2103–2105, 1989.
- [85] YK Fukai, S Yamada, and H Nakano. Saturation of phase coherence length in  $\text{GaAs/AlGaAs}$  on-facet quantum wires. *Applied physics letters*, 56(21):2123–2125, 1990.
- [86] P Mohanty, EMQ Jariwala, and RA Webb. Intrinsic decoherence in mesoscopic systems. *Physical Review Letters*, 78(17):3366, 1997.
- [87] P Fournier, J Higgins, H Balci, E Maiser, CJ Lobb, and RL Greene. Anomalous saturation of the phase coherence length in underdoped  $\text{Pr}_{2-x}\text{Ce}_x\text{CuO}_4$  thin films. *Physical Review B*, 62(18):R11993, 2000.
- [88] F Pierre, AB Gougam, A Anthore, H Pothier, D Esteve, and Norman O Birge. Dephasing of electrons in mesoscopic metal wires. *Physical Review B*, 68(8):085413, 2003.
- [89] C Bäuerle, F Mallet, F Schopfer, D Mailly, G Eski, and L Saminadayar. Experimental test of the numerical renormalization-group theory for inelastic scattering from magnetic impurities. *Physical review letters*, 95(26):266805, 2005.
- [90] L Saminadayar, P Mohanty, RA Webb, P Degiovanni, and C Bäuerle. Electron coherence at low temperatures: The role of magnetic impurities. *Physica E: Low-dimensional Systems and Nanostructures*, 40(1):12–24, 2007.

- [91] DM Pooke, N Paquin, M Pepper, and A Gundlach. Electron-electron scattering in narrow si accumulation layers. *Journal of Physics: Condensed Matter*, 1(20):3289, 1989.
- [92] B Beschoten, E Johnston-Halperin, DK Young, M Poggio, JE Grimaldi, S Keller, SP DenBaars, UK Mishra, EL Hu, and DD Awschalom. Spin coherence and dephasing in gan. *Physical Review B*, 63(12):121202, 2001.
- [93] WH Lau, JT Olesberg, and ME Flatté. Electron-spin decoherence in bulk and quantum-well zinc-blende semiconductors. *Physical Review B*, 64(16):161301, 2001.
- [94] AM Tyryshkin, S Tojo, JJJ Morton, H Riemann, NiV Abrosimov, P Becker, HJ Pohl, T Schenkel, MLW Thewalt, KM Itoh, et al. Electron spin coherence exceeding seconds in high-purity silicon. *Nature materials*, 11(2):143–147, 2012.
- [95] BJF Lin, MA Paalanen, AC Gossard, and DC Tsui. Weak localization of two-dimensional electrons in g a a s- al x ga 1- x as heterostructures. *Physical Review B*, 29(2):927, 1984.
- [96] PM Mensz and RG Wheeler. Magnetoconductance due to parallel magnetic fields in silicon inversion layers. *Physical Review B*, 35(6):2844, 1987.
- [97] BL Altshuler. Fluctuations in the extrinsic conductivity of disordered conductors. *JETP lett*, 41(12):648–651, 1985.
- [98] AD Stone. Magnetoresistance fluctuations in mesoscopic wires and rings. *Physical review letters*, 54(25):2692, 1985.

- [99] PA Lee and AD Stone. Universal conductance fluctuations in metals. *Physical review letters*, 55(15):1622, 1985.
- [100] S Feng, PA Lee, and AD Stone. Sensitivity of the conductance of a disordered metal to the motion of a single atom: Implications for 1 f noise. *Physical review letters*, 56(18):1960, 1986.
- [101] SB Kaplan and A Hartstein. Universal conductance fluctuations in narrow si accumulation layers. *Physical review letters*, 56(22):2403, 1986.
- [102] PA Lee, AD Stone, and H Fukuyama. Universal conductance fluctuations in metals: Effects of finite temperature, interactions, and magnetic field. *Physical Review B*, 35(3):1039, 1987.
- [103] M Büttiker. Four-terminal phase-coherent conductance. *Physical review letters*, 57(14):1761, 1986.
- [104] BL Altshuler and DE Khmelnitskii. Fluctuation properties of small conductors. *Jetp Lett*, 42(7):359, 1985.
- [105] GL Chen, J Han, TT Huang, S Datta, and DB Janes. Observation of the interfacial-field-induced weak antilocalization in inas quantum structures. *Physical Review B*, 47(7):4084, 1993.
- [106] W Knap, C Skierbiszewski, A Zduniak, E Litwin-Staszewska, D Bertho, F Kobbi, JL Robert, GE Pikus, FG Pikus, SV Iordanskii, et al. Weak antilocalization and spin precession in quantum wells. *Physical Review B*, 53(7):3912, 1996.
- [107] Takaaki Koga, Junsaku Nitta, Tatsushi Akazaki, and Hideaki Takayanagi. Rashba spin-orbit coupling probed by the weak antilocalization analysis in

inalas/ingaas/inalas quantum wells as a function of quantum well asymmetry.

*Physical review letters*, 89(4):046801, 2002.

[108] AE Hansen, MT Björk, Carina Fasth, Claes Thelander, and Lars Samuelson. Spin relaxation in inas nanowires studied by tunable weak antilocalization.

*Physical Review B*, 71(20):205328, 2005.

[109] KH Gao, G Yu, YM Zhou, WZ Zhou, T Lin, JH Chu, N Dai, DG Austing, Y Gu, and YG Zhang. Experimental study of weak antilocalization effects in a two-dimensional system: Anomalous dephasing rate. *Physical Review B*, 79(8):085310, 2009.

[110] P Roulleau, T Choi, S Riedi, T Heinzl, I Shorubalko, T Ihn, and K Ensslin. Suppression of weak antilocalization in inas nanowires. *Physical Review B*,

81(15):155449, 2010.

# Appendix A

## The growth structure of the experimental wafers

*GaAs/AlGaAs (W923)*

Matrix Layers										
Layer	Material	Time	[nm]	Ratio	Repeat?	Repeat No.	T-SUB	Dopant	Doping	Comments
1	GaAs	00:03:20	50		<input type="checkbox"/>		600			-----
2	AlAs	00:06:40	50		<input type="checkbox"/>		600			Pyro oscillation interface
3	GaAs	00:33:20	500		<input type="checkbox"/>		600			-----
4	AlGaAs	00:00:10	2.5	0.33	<input checked="" type="checkbox"/>	400	600			2um total SLB
5	GaAs	00:00:07	2.5		<input checked="" type="checkbox"/>	400	600			-----
6	GaAs	01:06:40	1000		<input type="checkbox"/>		600			Usual 1um GaAs buffer
7	AlGaAs	00:02:40	60	0.33	<input type="checkbox"/>		600			-----
8	Interrupt	00:05:30			<input type="checkbox"/>		600			Ramp Si cell
9	AlGaAs	00:01:47	40	0.33	<input type="checkbox"/>		600	Si	1.00E+18	Resultant doping level
10	GaAs	00:00:40	10		<input type="checkbox"/>		600			-----
<b>Total</b>		02:00:54	1715		<i>Note that the calculated total values do not include repeat layers</i>					

$In_{0.75}Ga_{0.25}As/In_{0.75}Al_{0.25}As$  (W402):

Matrix Layers											
Layer	Material	Time	[nm]	Ratio	Repeat?	Repeat No.	T-SUB	Dopant	Doping	Comments	
1	GaAs	00:03:00	50		<input type="checkbox"/>		580			In cell down to 0.025um/hr setting, Si cell -> 1E13	
2	AlAs	00:09:00	75		<input type="checkbox"/>		580				
3	GaAs	00:15:00	250		<input type="checkbox"/>		580				
4	Interrupt	00:20:00			<input type="checkbox"/>		405			Find 405 BandIT before starting buffer, Ga cell down, As -> 270	
5	InAlAs	00:11:26	100	0.05	<input type="checkbox"/>		405			In@0.025, Al@0.5	
6	InAlAs	00:10:57	100	0.16	<input type="checkbox"/>		405			In->0.097, Al->0.473	
7	InAlAs	00:10:06	100	0.26	<input type="checkbox"/>		405			In->0.17, Al->0.446	
8	InAlAs	00:09:23	100	0.35	<input type="checkbox"/>		405			In->0.242, Al->0.42	
9	InAlAs	00:08:45	100	0.42	<input type="checkbox"/>		405			In->0.315, Al->0.393	
10	InAlAs	00:08:12	100	0.49	<input type="checkbox"/>		405			In->0.387, Al->0.366	
11	InAlAs	00:07:43	100	0.56	<input type="checkbox"/>		405			In->0.46, Al->0.34	
12	InAlAs	00:07:17	100	0.61	<input type="checkbox"/>		405			In->0.532, Al->0.313	
13	InAlAs	00:06:54	100	0.66	<input type="checkbox"/>		405			In->0.605, Al->0.286	
14	InAlAs	00:06:34	100	0.71	<input type="checkbox"/>		405			In->0.677, Al->0.26	
15	InAlAs	00:06:15	100	0.75	<input type="checkbox"/>		405			In@0.75, Al->0.233	
16	InAlAs	00:06:17	100	0.8	<input type="checkbox"/>		405			In@0.75, Al->0.175	
17	InAlAs	00:06:40	100	0.85	<input type="checkbox"/>		405			In@0.75, Al->0.123	
18	Interrupt	00:05:00			<input type="checkbox"/>		405			In@0.75, Al->0.233, Ga@0.233	
19	InAlAs	00:15:15	250	0.75	<input type="checkbox"/>		405			75% Buffer, Si cell -> 1E15	
20	InGaAs	00:01:50	30	0.75	<input type="checkbox"/>		405			Channel	
21	InAlAs	00:03:40	60	0.75	<input type="checkbox"/>		405			Si cell -> 2.3E17	
22	InAlAs	00:00:55	15	0.75	<input type="checkbox"/>		405	Si	2.30E+17	As per V504	
23	InAlAs	00:02:26	45	0.75	<input type="checkbox"/>		405				
24	InGaAs	00:00:07	2	0.75	<input type="checkbox"/>		405			Thin cap	
<b>Total</b>		03:02:42	2077								Note that the calculated total values do not include repeat layers

$In_{0.75}Ga_{0.25}As/In_{0.75}Al_{0.25}As$  (W436):

Matrix Layers										
Layer	Material	Time	[nm]	Ratio	Repeat?	Repeat No.	T-SUB	Dopant	Doping	Comments
1	GaAs	00:03:00	50		<input type="checkbox"/>		580			In cell down to 0.025um/hr setting, Si cell -> 1E13
2	AlAs	00:09:00	75		<input type="checkbox"/>		580			-----
3	GaAs	00:15:00	250		<input type="checkbox"/>		580			-----
4	Interrupt	00:25:00			<input type="checkbox"/>		360			Aiming colder than last time, Ga cell down, As -> 240
5	InAlAs	00:11:26	100	0.05	<input type="checkbox"/>		360			In@0.025, Al@0.5
6	InAlAs	00:10:57	100	0.16	<input type="checkbox"/>		360			In->0.097, Al->0.473
7	InAlAs	00:10:06	100	0.26	<input type="checkbox"/>		360			In->0.17, Al->0.446
8	InAlAs	00:09:23	100	0.35	<input type="checkbox"/>		360			In->0.242, Al->0.42
9	InAlAs	00:08:45	100	0.42	<input type="checkbox"/>		360			In->0.315, Al->0.393
10	InAlAs	00:08:12	100	0.49	<input type="checkbox"/>		360			In->0.387, Al->0.366
11	InAlAs	00:07:43	100	0.56	<input type="checkbox"/>		360			In->0.46, Al->0.34
12	InAlAs	00:07:17	100	0.61	<input type="checkbox"/>		360			In->0.532, Al->0.313
13	InAlAs	00:06:54	100	0.66	<input type="checkbox"/>		360			In->0.605, Al->0.286
14	InAlAs	00:06:34	100	0.71	<input type="checkbox"/>		360			In->0.677, Al->0.26
15	InAlAs	00:06:15	100	0.75	<input type="checkbox"/>		360			In@0.75, Al->0.233
16	InAlAs	00:06:17	100	0.8	<input type="checkbox"/>		360			In@0.75, Al->0.175
17	InAlAs	00:06:40	100	0.85	<input type="checkbox"/>		360			In@0.75, Al->0.123
18	Interrupt	00:05:00			<input type="checkbox"/>		360			In@0.75, Al->0.233, Ga@0.233
19	InAlAs	00:15:15	250	0.75	<input type="checkbox"/>		360			75% Buffer, Si cell -> 1E15
20	InGaAs	00:01:50	30	0.75	<input type="checkbox"/>		360			Channel
21	InAlAs	00:03:40	60	0.75	<input type="checkbox"/>		360			Si cell -> 1.8E17
22	InAlAs	00:00:55	15	0.75	<input type="checkbox"/>		360	Si	1.80E+17	Reduced cf. W0413
23	InAlAs	00:02:26	45	0.75	<input type="checkbox"/>		360			-----
24	InGaAs	00:00:07	2	0.75	<input type="checkbox"/>		360			Thin cap
<b>Total</b>		03:07:42	2077	<i>Note that the calculated total values do not include repeat layers</i>						

# Appendix B

## List of Notations

$j$	Current density	$W$	Width of 2DEG
$\sigma$	Conductivity	$h$	Planck's constant
$E$	Electric field	$L_\phi$	Phase coherence length
$n_e$	Carrier density	$\rho_{xx}$	Resistivity in transverse direction
$e$	Elementary charge		
$\tau$	Scattering time	$\rho_{xy}$	Resistivity in longitudinal direction
$\mu$	Electron mobility		
$m^*$	Effective mass of electrons	$\omega_c$	Cyclotron angular frequency
$L$	Length of 2DEG	$B$	Magnetic field
$l$	Mean free path	$E_n$	Landau levels
$D$	Diffusion constant	$\hbar$	Reduced Planck's constant
$E_F$	Fermi energy	$g$	Laudé g-factor
$\rho(E)$	Density of states	$\mu_B$	Bohr magnetron
$v_F$	Fermi velocity	$\nu$	Filling factor
$\tau_\phi$	Phase coherence time	$f(E)$	Fermi-dirac distribution
$G$	Conductance	$k_B$	Boltzmann constant

$E_c$	Carrier energy above conduction band	$\tau_{in}$	Inelastic scattering time
$T$	Temperature in Kelvin	$\tau_{ee}$	Electron-electron scattering time
$R$	Resistance	$\tau_{ep}$	Electron-phonon scattering time
$\xi$	localisation length	$\tau_N$	Nyquist rate
$\sigma_B$	Boltzmann conductivity	$L_N$	Phase coherence length in Nyquist mechanism
$k_F$	Fermi wavevector	$L_{\phi'}$	Phase coherence length in phase breaking mechanism
$S$	Area of cross section	$\tau_{\phi'}$	Phase coherence time in phase breaking mechanism
$d$	Dimensionality	$L_T$	Thermal dephasing length
$G(L)$	Conductance of sample in length $L$	$V$	Voltage
$G(B)$	Boltzmann conductance	$I$	Current
$\sigma(L)$	Conductivity of sample in length $L$	$V_{SG}$	Split-gate voltage
$\Delta\phi$	Phase difference between coherent waves	$\lambda_F$	Fermi wavelength
$\Phi(x)$	Digamma function	$rms(G)$	Root mean square of conductance variations
$\tau_B$	Magnetic diffusion time	$L(x)$	Length of sample in transverse direction of 2DEG
$\delta G(B)$	Magnetoconductance	$L(y)$	Length of sample in longitudinal direction of 2DEG
$\Delta G(B)$	Conductance difference at magnetic field $B$	$L(z)$	Length of sample in perpendicular to the 2DEG
$I_{coh}$	Coherent fraction		
$\delta\sigma$	Magnetoconductivity		
$\tau_{SO}$	Spin-orbit scattering time		
$\tau_S$	Spin flipping time		
$F$	Screened Coulomb potential		